Surface Plasmon Induced Enhancement in the Optical and Photocurrent Properties of Metal-Semiconductor Hybrids

Thesis Submitted to AcSIR For the Award of

the Degree of

DOCTOR OF PHILOSOPHY

In Chemical Sciences

August-2016

By

Mr. Sandeep G. Yenchalwar

(Reg. No. 10CC11J26088)

Dr. (Mrs.) Manjusha V. Shelke

Research Guide

Physical & Materials Chemistry Division,

CSIR-National Chemical Laboratory, Pune - 411008

सीएसआयआर-राष्ट्रीय रासायनिक प्रयोगशाला
(वैज्ञानिक तथा औद्योगिक अनुसंधान परिषद)
डॉ. होमी भाभा मार्ग, पुणे - 411 008. भारत
CSIR-NATIONAL CHEMICAL LABORATORY
(Council of Scientific & Industrial Research)
Dr. Homi Bhabha Road, Pune - 411 008. India.

Dr. Manjusha V. Shelke
Scientist,
mv.shelke@ncl.res.in,
Physical and Materials Chemistry Division,
Ph. No. 020 2590 2308

Certificate

This is to certify that the work incorporated in this Ph.D. thesis entitled ***"Surface Plasmon Induced Enhancement in the Optical and Photocurrent Properties of Metal-Semiconductor Hybrids"*** submitted by **Mr. Sandeep Gopal Yenchalwar** to Academy of Scientific and Innovative Research (AcSIR) in fulfilment of the requirements for the award of the Degree of **DOCTOR OF PHILOSOPHY** embodies original research work under my/our supervision/guidance. I/We further certify that this work has not been submitted to any other University or Institution in part or full for the award of any degree or diploma. Research material obtained from other sources has been duly acknowledged in the thesis. Any text, illustration, table etc., used in the thesis from other sources, have been duly cited and acknowledged.

Mr. Sandeep Yenchalwar

(Student)

Dr. Manjusha V. Shelke

(Supervisor)

Declaration

I certify that this thesis is the result of my own work which is the outcome of work done at the ***CSIR-National Chemical Laboratory, Pune, India*** *under the supervision of* ***Dr. (Mrs.) Manjusha V. Shelke.*** *It has not, previously submitted, in part or whole, to any university/ institution for any degree, diploma, or other qualification. It does not contain any material previously published or written by another person except where due reference is made in the text.*

Date: 19/08/2016

Mr. Sandeep G. Yenchalwar

CSIR- National Chemical Laboratory, Pune-411008

Dedicated To

My Parents

Acknowledgements

I would like to express sincere gratitude to my research supervisor Dr. (Mrs.) Manjusha V. Shelke. Her support, encouragement and guidance have benefited me to develop my knowledge, skills in the field of plasmonics and photonics to pursue as a scientific carrier. I truly enjoyed working while following the unprecedented path in the chosen research area under her mentorship. I extend my sincere thanks to the Director of CSIR-NCL Dr. Ashwini Kumar Nangia, Head of Physical and Materials Chemistry Division Dr. P. A. Joy. I sincerely acknowledge my DAC members Dr. Ajit Kumar, Dr. C. V. Avadhani and Dr. Pankaj Poddar for their assessment. I offer my sincere regards to several teachers for their kind help in the characterizations and analysis. I'm thankful to peoples who have inspired me directly or indirectly in the research carrier and my labmates for their kind help during the tenure of this passage. I am grateful to University Grants Commission (UGC), New Delhi, for awarding the research fellowship and CSIR-National Chemical Laboratory to carry out my research works.

My deepest indebtedness and love to my parents. My father, mother, brother Shashikant, his wife Nilam, my sisters Manisha and Vaishali are always their providing constant support and endless love. I would also like to dedicate this thesis to the little family members Yash, Nishi, Shivam and Swara welcome to this amazing world.

- Mr. Sandeep G. Yenchalwar

List of Abbreviations and Acronyms

APTMS	Aminopropyltrimethoxysilane
AFM	Atomic Force Microscope
AuNPs	Gold Nanoparticles
AuNRs	Gold Nanorods
AzPTES	Azidopropyltriethoxysilane
Cabs	Absorption Cross Section
CB	Conduction Band
Cu	Copper
Csca	Scattering Cross Section
CuS	Copper Sulphide
CV	Cyclic Voltametry
D	Detectivity
DRS	Diffuse Reflection Spectroscopy
Ef	Fermi Energy
EM	Electromagnetic Field
Eg	Band Gap Energy
Eocv	Open Circuit Voltage
eV	Electron Volt
FTIR	Fourier Transform Infrared Spectroscopy
FTO	Fluorine Tin Oxide
GO	Graphene Oxide
rGO	Reduced Graphene Oxide
H-SiNWs	Hydrogen Terminated Silicon Nanowires

HRTEM	High Resolution Transmission Electron Microscope
ID	Defect Domain Intensity
IG	Graphitic Domain Intensity
IPCE	Internal Photon Conversion Efficiency
IR	Infrared
J	Current Density
J_D	Dark-current Density
J_{Ph}	Photocurrent Density
LED	Light Emitting Diode
LSPR	Localized Surface Plasmon Resonance
LSV	Linear Sweep Voltametry
LO	Longitudinal Optical
LTO	Longitudinal and Transversal Optical
mA/W	Milliampere per Watt
mbar	Millibar
mW	Mill watt
NP	Nanoparticle
NR	Nanorod
1D	One Dimension
PEC	Photoelectrochemical
PL	Photoluminescence
P_{Opt}	Optical Power
Pt	Platinum
R	Responsivity

Rct	Charge Transfer Resistance
RF	Radio Frequency
SEM	Scanning Electron Microscope
SERS	Surface Enhanced Raman Spectroscopy
SiNWs	Silicon Nanowires
SPP	Surface Plasmon Polariton
SPR	Surface Plasmon Resonance
STE	Self Trapped Electron
TA	Transverse Acoustic
2D	Two Dimension
3D	Three Dimension
TEM	Transmission Electron Microscope
TO	Transverse Optical
UV	Ultraviolet
UV-Vis	Ultraviolet and Visible
VB	Valence Band
χ	Electron Affinity
XPS	X-ray Photoelectron Spectroscopy
XRD	X-ray Diffraction

Contents

Introduction to Surface Plasmon Resonance Basics and Metal-Semiconductor hybrids

The thesis is related to the study of cumulative optical and photocurrent properties of metal-semiconductor hybrids. The noble metal nanoparticles can be exploited in conjunction with the semiconductor materials for numerous applications in the energy devices. The hybrid has been studied for its enhanced optical properties such as absorption, photoluminescence and electronic (photodetection) properties. The chapter covers the introduction of the surface plasmon theory, concepts such as surface plasmon resonance (SPR), surface plasmon polariton (SPP), Localized surface plasmon resonance (LSPR) alongwith surface plasmon resonance enhanced optical properties which modify the physical properties of the other materials and the devices made from them. The foundation of this thesis is build up on the basis of these fundamental concepts.

1.1 Introduction

1.1.1 Surface Plasmon Basic Concepts:

Plasmons are a quantum of electron density oscillation on the metal. These plasmons can be divided on the basis of the material composition and materials dimensions into following,

1) Bulk plasmons: The term is related to the electron density oscillation inside the bulk of the metals. They require very large amount of energy for their excitation such as 10-30 eV. Therefore, these cannot be excited by the photons in the optical frequency however electron beam can excite them.

2) Surface plasmons: These are the quantum of electron density oscillations on the metal surface. They can be excited by a specific frequency of photons incident on the metal-air interface and decay exponentially back into photons. The excitation frequency range lies in the visible part of the solar spectrum.

Surface plasmons further can be differentiated into,

i) Surface plasmon polariton: The electron density excitation on the interface between the dielectric-metal surface and they can propagate along the surface of the metals.

ii) Localized surface plasmon: Metal nanostructures possess localized surface plasmons (LSP) which are collective electron charge oscillations confined to its surface or dimensions. They exhibit enhanced near-field amplitude at the resonance wavelength. This field is highly localized at the surface of the nanostructure and decays rapidly away as shown in **Figure 1.1** from the nanostructure/dielectric interface into the dielectric background, though far-field scattering by the nanostructure.[1-8]

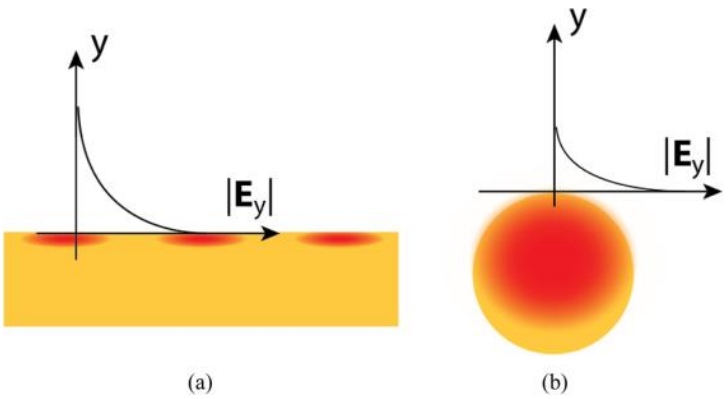

Figure 1.1a) Simple illustrations of Surface Plasmon Polaritons on thin metal films surface. **b)** Localized Surface Plasmon Resonance on the metal nanoparticles surface with its exponential decay as a function of distance.[9]

1.1.2 Surface plasmon on metallic nanostructures (LSPs)

Noble metals gold (Au), silver (Ag) and copper (Cu) are all elements belonging to the 11th group of the periodic table. The electronic configurations of these elements have completely filled d-subshells (respectively 3d, 4d and 5d). Their metallic properties result from the lone valence electron in the half-filled s-subshells (4s, 5s and 6s respectively).

The band structure of gold displays five comparatively flat d-bands, lying 1− 3 eV below the *Fermi energy* (E_f) in which the ten d-electrons are located (**Figure 1.2**). The lone s-electron forms a sp-hybridised band, which is filled up to E_f. Electrons in this band can move quasi-free due to the near parabolic form of the band. This band structure defines the characteristic properties of these metals, such as their thermal and electrical conductivity.

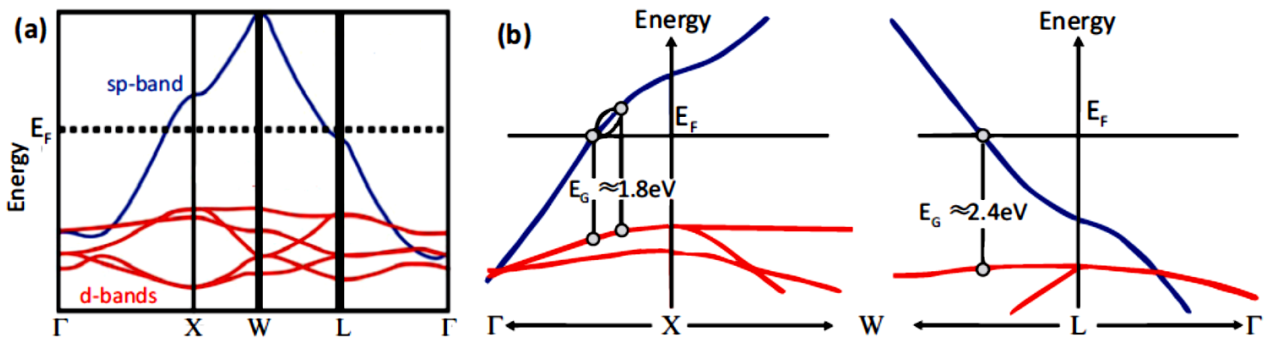

Figure 1.2 The band structure of gold. **a)** The sp-band has a nearly parabolic form leading to quasi-free electrons. **b)** Interband transitions in gold occur near the X-and L- points in the Brilliouin zone.[10, 11]

If an electromagnetic wave impinges on a metallic nanoparticle (whose spatial dimension is assumed to be much smaller than the wavelength of light), the electron gas gets polarized (polarization charges at the surface) and the arising restoring force again forms a plasmonic oscillation. The metallic particle thus acts like an oscillator and the corresponding resonance behaviour determines the optical properties.[10, 11]

a) Dipole Plasmon Resonances:

Irradiation of spherical metal nanostructures by light causes in resonance oscillation of the free electrons with oscillating electric field as represented schematically in the **Figure 1.3**. The displacement of the electron cloud relative to the nuclei induces a restoring force due to coulombic attraction between electrons and nuclei. The term “dipole plasmon resonance” was coined to these collective oscillations of the electrons on the metal nanostructures. The resonance frequency is dependent on various factors such as: the electron density, the effective mass of electron, the shape/size and physical environment around on the metal nanostructures.

The geometry of the metal nanoparticles influences the optical properties which has been an active research field. The main optical features for various spherical, spheroidal, cubic[12-13], and other geometrical shapes, like rods[14-17]and triangular prisms, are identified and extensively studied revealing the dependence on geometry and size.

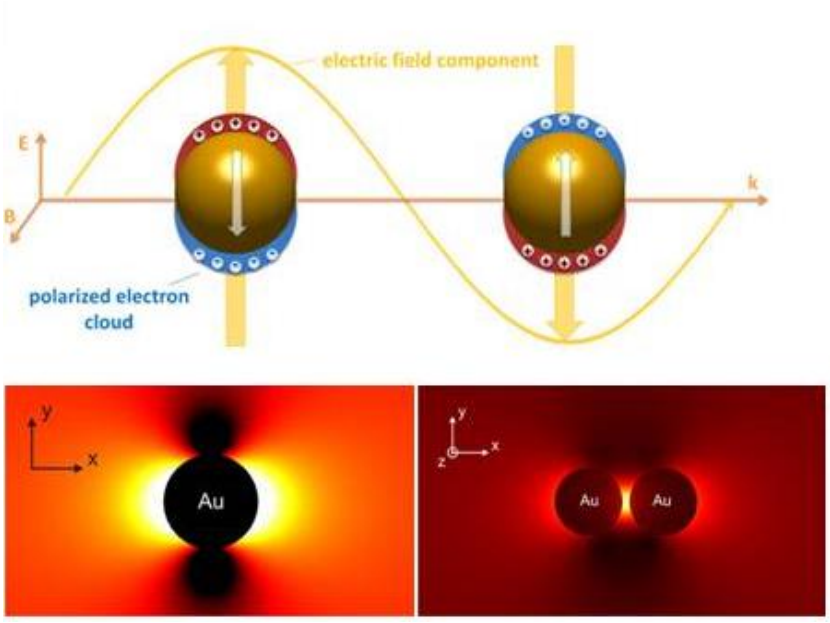

Figure 1.3 a) Surface plasmon schematics **b)** Electric field enhancement on single and coupled metal nanoparticle.[18]

Maxwell theory explains the origin of surface plasmons where free electrons of a metal are treated as an electron plasma (sea of electrons) and electron plasma density fluctuations arising on the surface of a metal are called plasmons, surface plasmons (SP), or surface plasmon polaritons. The surface plasmons can transmit along a metallic surface and have general dispersion relation based on the eigen frequencies (ω) with the wave vector (k) of light described below:

$$k_{SP} = \frac{\omega}{c}\sqrt{\frac{\varepsilon_d \varepsilon_m}{\varepsilon_d + \varepsilon_m}}$$

Where,

$\varepsilon_m = \varepsilon_m' + i\,\varepsilon_m''$=frequency dependent metal dielectric constant,

ε_d =dielectric constant of medium in contact with the metal,

c = speed of light in vaccum,

ω = frequency of light respectively.

The dispersion relation elucidates the conditions necessary to excite the plasmons. When there is no other intervening medium, light passes through air elastically. In other words, the surface plasmon cannot be excited as the dispersion relation does not intersect the dispersion relation (straight line) of light in air by freely propagating beam of light.

$$k_1 = \frac{\omega}{c}\sqrt{\varepsilon_1}$$

$$k_1 = \frac{\omega}{c} \ldots\ldots\ldots\ldots\ldots\ldots (For\ air, \varepsilon_1 = 1)$$

It is possible to excite surface plasmon if any dielectric is present in conjunction with metal satisfying the conditions of momentum conservation at a particular frequency. The light line bending at that specific frequency is the frequency of the surface plasmon resonance.

The interaction between the surface charge density and the electromagnetic fields results in the momentum of the SP being greater than that of a free-space photon of the same frequency. For SP to

be possible, ε_m and ε_d must have opposite signs. This condition is satisfied for metals because ε_m is negative.[1, 19-20]

b) Scattering and Absorption by Metal Nanostructures:

Metal nanoparticles possess high scattering and absorption cross section for light which are useful in various applications. Absorption and scattering cross sections, C_{abs} and C_{sca} are given by the equations that govern the scattering and absorption of light for particles, at $d << \lambda$ limit, can be written as:

$$\sigma_{scat} = \frac{k^4}{6\pi}|\alpha|^2 \ldots\ldots\ldots\ldots\ldots (1)$$

$$\sigma_{abs} = k\, Im\,(\alpha) \ldots\ldots\ldots\ldots\ldots (2)$$

The polarizability α of the particle is given by:

$$\alpha = 4\pi a^3 \frac{\varepsilon - \varepsilon_m}{\varepsilon + 2\varepsilon_m} \ldots\ldots\ldots\ldots (3)$$

Where, ε_m = dielectric function of the metal particle, ε = dielectric function of the embedding medium and a = radius of metal particle.

For spherical particles, when the denominator in the equation 3, i.e. [ε + 2 ε_m] is minimum the polarizability of the particle becomes maximum and resonance occurs which is the case in metals with negative dielectric constant. Different metals have different densities of electrons and reflect specific radiation, depending on the resonance. The plasmon resonant frequency can be modified or shifted depending on the dielectric constant of the host medium. Higher refractive index leads to a higher wavelength shift and broaden the plasmon resonance frequency range. The equations also

show that scattering and absorption of a metal nanoparticle are resonantly enhanced at its plasmon resonance.[2, 3, 19-21]

Plasmonic metal nanostructures are particularly stimulating on account of their wavelength dependent LSPR absorption and scattering. The geometric properties for example size, shape and physical properties such as dielectric constant, refractive index influences the optical properties of the nanostructures. The smaller metal nanoparticles predominantly absorbing in nature which can confine electromagnetic field in the nanoscale dimensions. This concentration of EM field alternatively give rise the highly important near-field enhancement as in surface enhanced Raman spectroscopy (SERS). The larger nanoparticles predominantly behave as a light scatterer in all direction after absorption of resonance frequency. Such peculiar nature of the plasmonic nanostructure is highly appreciated as nano-mirrors in solar cells, photodetectors and photonics. However, these factors not concerted only to the metal nanoparticles. The other 1D, 2D and 3D metal nanostructures are also proving their impact in the said applications. These structure possess higher dimensional plasmon or multimodal plasmons which are useful in the low frequency or in the infrared region.[22-27]

SPRs on metal nanostructures not only altered by small changes in the morphology but also influenced by the modification in the physical environment around the metallic nanostructures. Most important physical property is the dielectric strength and refractive index of the surrounding media which can be shown to shift SPRs. In particular, high value of these factors of a medium shifts SPRs to the longer wavelength of the electromagnetic spectrum by substrate induced multipolar coupling, or local field effects. SP can always absorb light from or emit light into the surrounding medium when the resonant wavelength is matched. Either SPP or LSP extends its energy distribution (a near-field electromagnetic field distribution) in the dielectric or semiconductor material when an SP mode is

generated at the interface between a dielectric (semiconductor) and a metal structure. Such a near-field energy distribution can be absorbed or amplified by the dielectric or semiconductor depending on its excitation condition. In a solar cell, the effective absorption of an SP mode on a metal nanostructure and hence the transfer of SP energy into the solar cell absorbing material create an extra channel for harvesting sunlight photons. The SP interaction in a solar cell is particularly useful in enhancing the absorption efficiency in the spectral range of a low material absorption coefficient.[28-31]

c) Plasmon Decay Pathways:

Metals nanostructures owning high density electronic states and larger scattering, absorbing cross section can be exploited for the energy harvesting and consumption technologies. Plasmonic properties of metal nanostructures enhance light absorption and emission of the other host materials.

The excited plasmons can be utilized through enabling proper decay channels such as,

1) Radiative and 2) Non-radiative represented in the **Figure 1.4**.

The excited surface plasmon can be relaxed by any of the above mentioned ways. In the first case the surface plasmon re-emit the absorbed photons. These photons can then be absorbed by the other semiconducting materials in the vicinity. Thus, minimizes the absorption losses of the semiconductor. While in the second route, the excited surface plasmon get converted into a pool of hot electrons. The presence of the semiconductor nearby the metal nanostructure can be used to extract these electron via Schottky barrier tunnelling. High energy conversion efficiency can be achieved by hot electron transfer in the conduction band (CB) of the semiconductor as a charge carriers.[33-36]

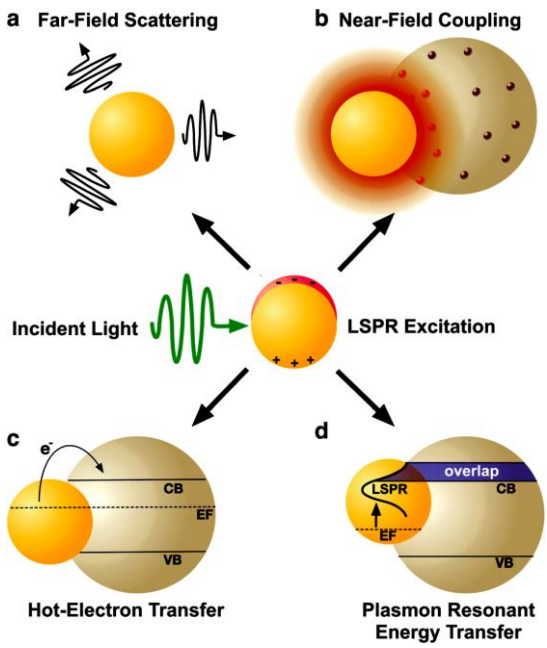

Figure 1.4 Radiative decay modes: **a)** far-field scattering, **b)** near-field coupling. Nonradiative decay modes: **c)** hot-electron transfer, **d)** plasmon resonant energy transfer.[32]

1.1.3 Semiconductors:

Semiconductor and semiconductor nanostructures are extremely important and relatively earliest explored materials. Contemporary electronic devices for example optoelectronic devices, including solar cells, photodetectors, field-effect transistors, light-emitting diodes, integrated circuits are based on various semiconductors. Semiconductors are intermediate materials between the conductor and insulator. They are arbitrarily distinguished on the basis of the magnitude of the energy band gap (*Eg*) between the filled valence band (VB) and the empty conduction band (CB). In semiconductors the energy band gap is typically in the range of 1 - 4 eV. The width of the band gap determines the conductivity as well as optical response of the semiconductor materials.[37-38]

Low dimensional semiconductor nanostructures such as quantum dots, nanosheets, nanoparticles and nanowires exhibit superior properties than their bulk equivalents. They are also advantages regarding high physio-chemical stabilities, unusual optical and electronic properties. Optical as well as electronic properties of the semiconductors can be tuned by controlling the dimensions and chemical compositions. Wide band gap semiconductors are the most commonly used materials such as TiO_2, ZnO etc. These inorganic semiconductor materials have high stability, environmental compatibility and photocatalytic activity. They have been widely popular as photocatalysts for direct conversion of solar energy into fuels. However, the efficiency of semiconductors is limited by their inability to absorb visible light due to high band gap.[39-41]

Graphene shows high room-temperature carrier mobility, tunable bandgap, and high transparency in visible range, and high mechanical strength.[42, 43] These unique properties make them very suitable for transparent electrodes, display devices, ultrafast lasers, optical modulators and solar cell applications.[42-46] Extensive studies have been performed to pursue the application of graphene to electronic devices because of its superior electronic properties. Synthesis of single layer graphene is economically costly requiring high temperature. However, rGO has a high density of states (DOS) away from the Dirac point with a semi-metallic band structure that is similar to that of metal NPs. rGO can be produced from graphene oxide in simple reduction processes alongwith high mass production. Also, we can modulate or alter the properties of the rGO by controlling the reduction process.[45-48]

Silicon is one of the highly significant semiconductor in photovoltaic cells and other optoelectronic devices.[49-52] However, the high refractive index of silicon limits its application due to intrinsic photon loss which is upto 40% occurs due to back reflection from the silicon/air interface.[53] Antireflection

layers with a graded-refractive-index and surface nano texturing have been widely explored in order to suppress the surface reflection over a broad wavelength range. 1D silicon nanowires (SiNWs) have been extensively researched and widely explored for its possible applications in the new generation solar cells, field effect transistors, optical and chemical sensing. The magnitude of the charge transport of the carriers in the SiNWs is lower than that observed in bulk Si due to lateral diffusion. Additionally the optical absorption of the SiNWs is far greater than the bulk Si ranging from visible to near infrared which results in a higher efficiency of the SiNWs based device. Various synthesis methods are available for the synthesis of SiNWs which include highly expensive and complicated process such as plasma etching, reactive ion etching, and laser assisted chemical etching etc. However, metal assisted chemical etching of silicon surface is popularly used for fabrication of SiNWs arrays. This method is very cheap and suitable for high-throughput and inexpensive industrial production.[52-66]

In recent decade, a great deal of research has been carried out to improve the efficiency of photo-catalysts and photovoltaic devices by integration of plasmonic nanoparticles (NPs) with semiconductor materials. The presence of plasmonic NPs leads to increase in the absorption cross-section of semiconductors via strong field enhancement, extension of light absorption to longer wavelengths and enhances electron–hole charge separation in semiconductor medium, thus maximize the efficiency of photocatalytic and photovoltaic devices. However, these semiconductor materials have very weak interaction in the visible light lowering their efficiency due to relatively small optical cross-sections in the visible region. Visible-light response of metal oxide semiconductor can be met by metal or non-metallic elements, controlling the morphology, developing heterostructures, integrating semiconductors with plasmonic metals.

1.1.4 Metal-semiconductor hybrids:

Surface plasmon resonances in metallic nanostructure inherit an intense and enhanced electromagnetic field which typically occurs nearby to the metal surface. It depends on the resonance frequency of the nanoparticle's size, shape, and local dielectric environment. These unique properties of plasmonic materials can be exploited as entirely new approach for energy application in the existing and emerging technologies. Integration of semiconductors with plasmonic metals to form plasmonic metal/semiconductor hybrid nanostructures has recently attracted much attention because of the unique properties of SPR.

Metal-semiconductor hybrid consists of multicomponent heterostructures with the properties different than its original counterparts. They may exhibit not only combined properties of the each components but also, interestingly, enhanced properties which can be tuned by altering the material characteristics. The close interaction of metallic nanostructure with the semiconductor component remarkably alter the hybrid's physical features such as plasmon-exciton coupling, local dielectric environment reform, improved light harvesting due to enhanced absorbance, charge separation relative to the each component. This hybrid effect results in the optical absorption enhancement of metal-semiconductor hybrid. We can selectively implement such desired properties into various applications including photonic, electronic, and optoelectronic. The surface plasmons can conduit the absorbed energy directly to the free electrons, and the generated hot electrons can be utilized in thermoelectric, solar cells and photocatalysis. The advantages of plasmonic metal-semiconductor hybrids over other conventional tools are expected to lead to performance improvements not achievable by other methods are identified.

1.1.5 Approaches and Applications:

The high absorption and scattering coefficient associated with the excitation of SPs opens a wide range of potential applications of metallic NPs in many fields. The possibility to concentrate, amplify and manipulate light at the nanoscale through SPs provides a method to improve optical effects or activate processes in a controlled way. There are hundreds of potential applications of SPs in different fields that have been thoroughly reported in the literature. We will just highlight some of them in order to illustrate capabilities of SPs in four selected fields: energy, environment protection and information technologies.

Plasmonic and surface plasmon enhanced photodetectors are emerging interests. Metallic nanostructures inherently support surface plasmons and when integrated in detectors based on internal photoemission or bandgap emission they enhanced the photodetection sensitivity along with the spectral range of interest. Metal waveguides, metal gratings, on nano-particles, sub-wavelength holes in a metal film are exploited to address the physical problems related to low-noise high-speed detection, single-plasmon detection, near- and mid-infrared imaging, bio-chemical sensing.

1.1.5: I] Optoelectronics Devices:

a) Photovoltaics:

Unlimited amount of solar energy is available as clean energy source to us on the earth and has to be harvested to overcome the growing energy demand. Solar energy is on the top amongst the alternative energy sources related to the ecological, environmentally friendly applications. It also concern with the calamitous environmental pollution arising as a result from burning fossil fuels. Photovoltaic cells

can offer efficient management of such energy by effectively converting sunlight into electrical power.[67-68]

Most of the semiconductor solar cells depend on the band-to-band excitation in the semiconductors, so that their spectral response is dependent on their bandgap. Large scale implementation of conventional photovoltaic technology hinders our ability to produce high efficiency modules. Also, solar cells have their own limitations including poor absorption. The energy conversion efficiencies of such cells are still low due to the large divergence between electronic and optical length scales in these devices; for photon energies close to the bandgap, the absorption depth of light in semiconductors is significantly longer than the electronic (minority carrier or exciton) diffusion length in most deposited thin film materials. In thin film solar cell, the reduced thickness of the silicon layer leads to insufficient sunlight absorption and inevitably the low energy conversion efficiency. Therefore light trapping technology is of paramount importance to increase the performance of thin-film solar cells to make them competitive with crystalline silicon solar cells, which are still dominant in the solar cell market.

Metal nanostructures can be used to tailor the optical and electronic properties of such devices due to plasmonic resonance in the vicinity of a metal-semiconductor junction. Relaxation of plasmons generates hot electrons which has tremendous applications in solar energy harvesting and photodetection. The ability to fabricate hot carrier based devices with tailored spectral response, is exciting for solar energy harvesting, visible or infrared detection.[69-70]

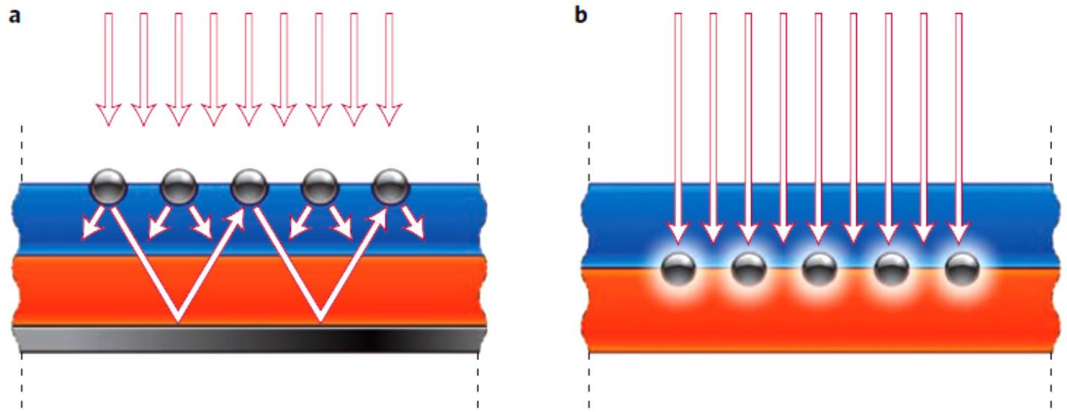

Figure 1.6 Plasmonic light-trapping for thin-film solar cells. **a)** Light scattering when the metal nanoparticles on the top of semiconductor surface. **b)** Absorption enhancement due to near field effect mechanism of LSPRs of metal nanoparticles embedded in the semiconductor.[3]

Plasmonic nanostructures can offer at least three ways of reducing the physical thickness of the photovoltaic absorber layers while keeping their optical thickness constant. The incorporation of metallic NPs in solar cells can increase the efficiency of charge separation by several physical processes. **Figure 1.6** illustrates, by placing metallic NPs at the device surface, upon light illumination, the large scattering cross section associated with SPs can scatter the normal incident light beams. Hence, the effective path across the active absorption layer is increased. Moreover, with a proper architecture, this scattering may be used to promote total reflection inside the layer trapping the photons until they are finally absorbed. The light concentration and local amplification in the vicinity of the NP when SPs are excited increases the absorption efficiency.

Photovoltaic cell efficiency of the order of 10–15% has been achieved by incorporating Au and Ag NPs on the cell surface. The efficiency in this kind of device has a complex dependence on the size of NPs, shape and spatial distribution, since interacting effects play a different role on the light scattering and absorption processes. The impact of both mechanisms in the final improvement is not

easy to disentangle although most recent results point towards the scattering process as the key one. Recently the silver nanoparticle-enabled plasmonic effect has been proposed and demonstrated as a promising approach to achieving light trapping in thin-film solar cells because the relative scattering efficiency of silver nanoparticles is higher than that of other noble metals in the visible range.

The nanoparticles can be used to effectively scatter the incident light into the intrinsic absorbing layer, increasing the optical path length in the thin film solar cells. It can also excite the surface plasmon modes to improve the light absorption within the absorbing layer. However, due to the resonant nature of the plasmonic effect useful absorption enhancements can only be realized at certain resonant scattering wavelengths determined by the nanoparticle size, shape, and their local dielectric environment. Therefore, broadband absorption enhancement is the primary challenge to tackle before the plasmonic solar cells can take off from laboratories. To achieve a broadband absorption enhancement in the silicon layer, the plasmonic nanostructures need to be able to strongly scatter the incident solar light into a large angle range so that light can be best trapped inside the silicon layer while keeping the particle absorption minimum.[71-90]

b) Photodetectors:

The ability of plasmonic structures to manipulate light in the nanoscale dimensions giving rise to potential application optoelectronic devices. The integration of metallic nanostructures with existing electronic and dielectric devices can be realized by an increasing number of nanofabrication techniques, including mature silicon integrated circuit technology. Of the many emerging applications, plasmon enhanced photodetectors are particularly promising.

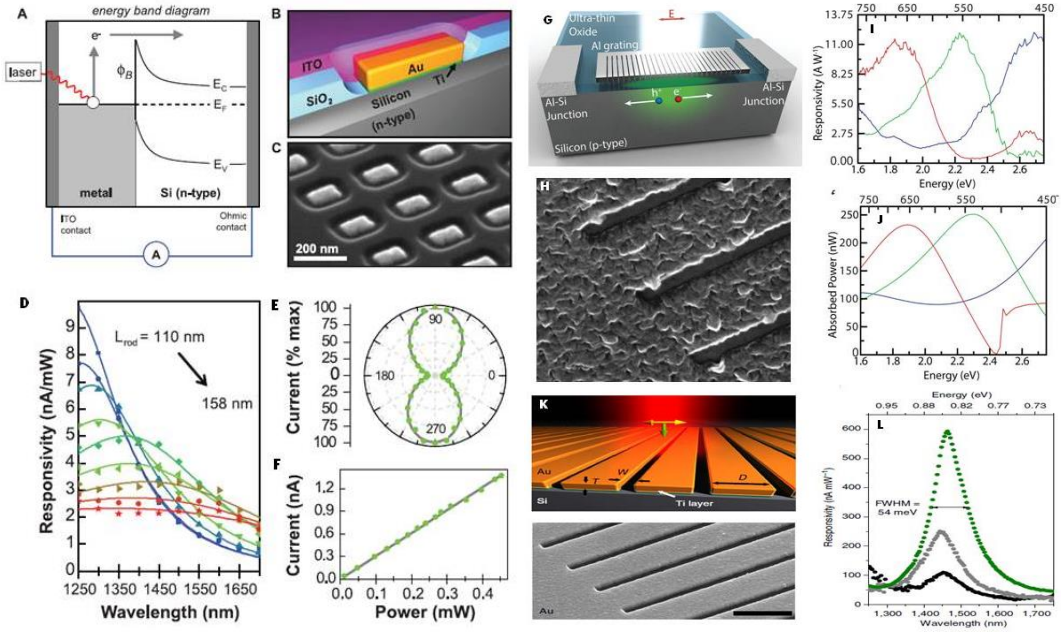

Figure 1.7 An optical antenna-diode for IR photodetection. **A)** Plasmonically driven internal photoemission over a nanoantenna/semiconductor Schottky barrier (Φ_B). **B** and **C)** Represents AuNRs antenna on silicon substrate **D and F)** Responsivity for different AuNRs antenna lengths: From 110-158 nm. **G, H** and **K)** Au nanostripe based Si-Schottky photodetector. **I, J** and **L)** Photocurrent from the respective devices[9, 91, 92]

By using metallic nanostructures as a bridge between dielectric microphotonics and nanoscale electronics, one plays to the strengths of both the metallic nanostructures (concentrating fields and subwavelength guiding) and semiconductor electronic components (high speed and high performance information processing). Plasmonics also offers the possibility of introducing new functionality, including polarization, angle or wavelength selectivity.

Gold nanorods as a light harvesting optical antenna in photodiodes have been demonstrated to enhance the photodetection. Coupling of photons with metallic nanoantenna excite plasmons, latter decaying into hot electrons crosses a potential barrier between the interfaces, results in a photocurrent.

By using gold nanoislands M. Naziradeh et al reported high photoresponsivity (3.5 mA/W) for Silicon based photodetector. Here they have explained that the absorption of sub bandgap electrons via the internal emission is enhanced resulting into high efficiencies. Multicolour graphene photodetector shows 1500% photocurrent and 1.5% external quantum efficiency due to plasmonic enhancement as reported by Y. Liu et al.[93-94]

Metallic- semiconductor-metal (MSM) and metal-insulator-metal (MIM) nano-junction has also been studied in which substantial boost is observed in the photodetection. Overall by harnessing the absorption and decay of surface plasmons (SPs) much higher photon to electron conversion efficiency can be obtained. This takes advantage of the higher absorptivity and spatial localization of SPs relative to linear bulk absorption and could operate across a broad frequency range.

1.1.5: II] Photoelectrochemical Water Splitting:

Photo-assisted hydrogen generation is a new strategy coming forward to sustain the energy crisis. Hydrogen can be stored and used as a fuel by simple water decomposition ($2H_2O \rightarrow 2H_2+O_2$) which is an endothermic decomposition process.[95] Environment friendly and clean solar light can be used to promote water splitting. Wide band gap semiconductors (e.g. TiO_2, ZnO) can be sensitized with metal nanostructures and effectively used to harvest photons over the entire solar spectrum. Such hybrids by using local surface plasmon resonances can be excited in the defined region of the spectrum to carry out hydrogen production.

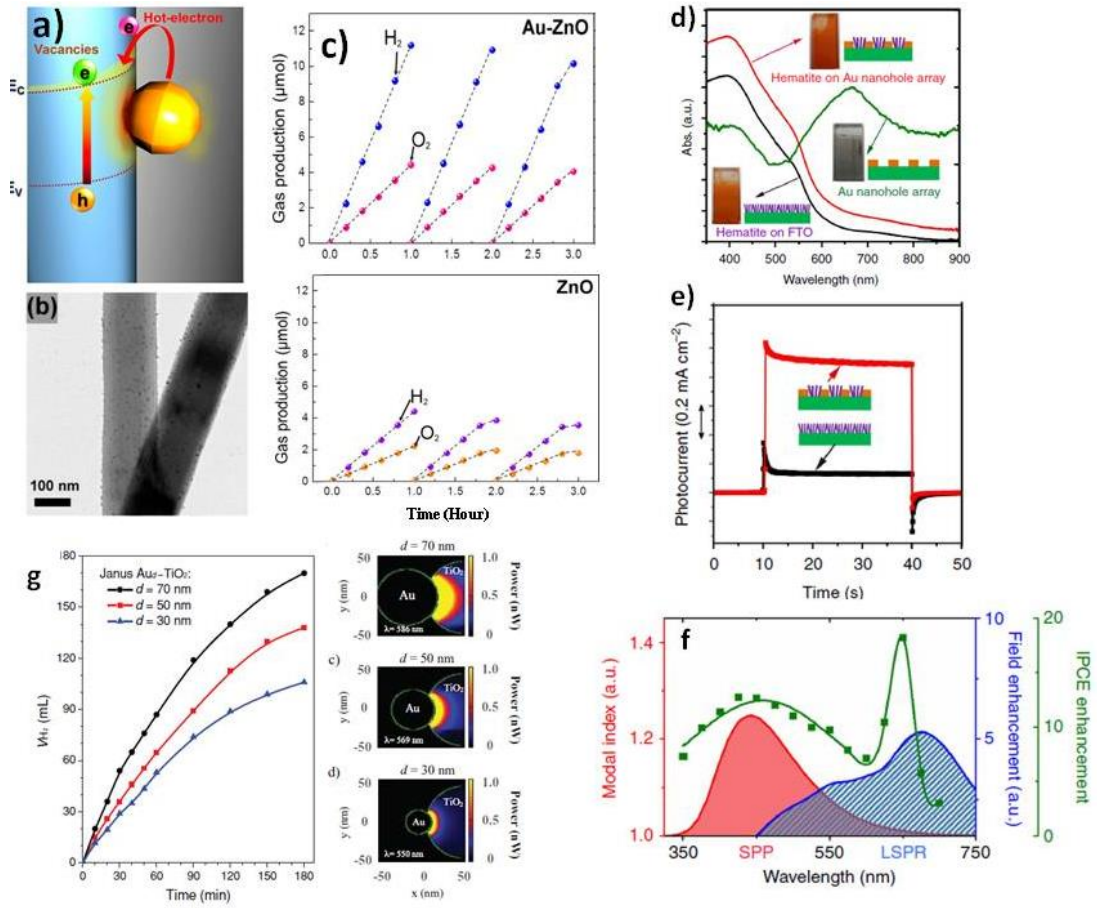

Figure 1.8.a) Schematics of hot electron transfer. **b)** AuNPs on ZnO nanorods. **c)** H_2 and O_2 evolution using Au/ZnO and ZnO photoelectrodes under AM 1.5G solar light. **d)** Absorption spectra for hematite nanorods on FTO and on the Au nanohole array pattern, respectively. **e)** Photocurrent dynamics of photoelectrodes versus Ag/AgCl. **f)** IPCE spectra of the electrodes. **g)** Enhanced electromagnetic field contribution in Janus AuNPs/TiO_2 in the water splitting.[99,100]

As in the above mentioned processes, SPs have demonstrated their capabilities to improve the efficiency of the process. Liu et al recently found an increase of a factor of 66 on the water splitting photocatalysis by TiO_2 when incorporated Au NPs. The local enhancement of the temperature associated with SP excitation may help the catalysis process that should be a photothermal assisted catalysis rather than a real photocatalytic one.[96-98]

The mechanism is based on the direct transfer of the charge carriers from the plasmonic nanostructure to a neighbouring semiconductor or to a semiconductor photocatalyst, or energy transfer in a neighbouring medium, resulting into photoconversion.

Such processes are highly important to accelerate an entire new prototype in garnering photons for real world application. The strong dependence of the wavelength at which the local surface plasmon can be excited on the nanostructure makes it possible, in principle, to design plasmonic devices that can harvest photons over the entire solar spectrum and beyond. For example, platinum nanoparticles on TiO_2 coated gold nanorods has been demonstrated in the hydrogen evolution. Such photocatalyst harness the visible light improving the rate of hydrogen evolution.

1.1.5: III] Plasmon-enhanced photocatalysis:

Many industrial processes result in products or by-products that are hazardous to humans and the environment. Reaction of these products to be transformed into inert ones is mandatory in order to ensure a secure and sustainable development of our society. Catalysis provides a pathway to eliminate these hazardous products quickly, hence reducing their potential danger. Among the different catalytic processes, photocatalysis exhibits particular importance since it is a clean process that can use solar light and mimics other biological processes.

Awazu et al demonstrated the increase in photocatalytic efficiency of a TiO_2 layer by embedding Ag NPs near the surface. Similarly, gold nanoparticles supported on Fe_2O_3 can substantially improve the catalysis of carbon monoxide. AuNPs/ Fe_2O_3 hybrid shows outstanding activity results as the excitation of SPs in AuNPs enhances the photocatalysis of Fe_2O_3. TiO_2 also shows SP enhanced photocatalysis as demonstrated in various reactions such as methanol dehydrogenation, acetic acid

decomposition, propanol oxidation and others. Seh et al demonstrated a photocatalytic process for efficient hydrogen generation using Janus Au-TiO_2 nanostructures due to their strong localization of plasmonic near-fields at the Au-TiO_2 interface.[101-107]

1.1.5: IV] Surface enhanced Raman spectroscopy:

Surface enhanced Raman scattering (SERS) is based on the enhancement of Raman scattering of an analyte molecule near or on a roughened metal substrate surface. Such enhancements were first observed by Van Duyne et al. and Creighton et al for pyridine adsorbed onto an electrochemically roughened silver electrode. Latter Moskovitz and co-workers correctly deduced the origin of the Raman enhancement is largely due to an enhanced EM field at the metal substrate surface due to increased absorption of the incident light.

At present there are two theories explaining the origin of SERS with substantially different mechanisms. The electromagnetic theory is based on the excitation of surface plasmons while chemical theory relies on the charge transfer.

1) EM theory: It is believed that the excited plasmons can amplify the electromagnetic field at the surface of the metal nanoparticle. At resonance wavelength of the surface plasmon, the field enhancement is highest and magnifies the intensity of the incident light. Raman scattering is highest when plasmon oscillations are perpendicular to the surface. Any molecule adsorbed on the nanoparticles surface experiences this field and Raman scattering occurs regardless of the molecule. The Raman signal output for molecules being studied is enhanced by the EM field by the factor of E^4, however it is not same for all frequencies.

2) Chemical Theory: In this theory a charge transfer in involved between the metal and adsorbed molecules. It occurs in conjunction with the electromagnetic enhancement. Chemical enhancement

mechanism in which metal-molecule charge transfer complexes are formed, which improve resonance with the Raman excitation laser. The chemical enhancement is sensitive to the surface properties of the SERS substrate and the nature of the analyte molecules.

The ability to analyse the composition of a mixture on the nanoscale makes the use of SERS substrates beneficial for environmental analysis, pharmaceuticals, material sciences, art and archaeological research, forensic science, drug and explosives detection, food quality analysis, and single algal cell detection. SERS combined with plasmonic sensing can be used for high-sensitivity and quantitative detection of biomolecular interaction.[108-115]

1.1.6 Stimulus behind the Thesis:

Plasmonics is a bourgeoning field in fundamental science and optoelectronics that exploits the unique optical properties of metallic nanostructures to control and manipulate light at nanodimensions. Extraordinary amalgamation of optical and electronic tasks can be achieved in the enormously vast applications through the plasmonics. Intense light localization, plasmonic optical antenna effect, optical resonators and lenses are a few excellent examples. Plasmonic nanoantennas deliver an expedient way to convert optical radiation into intense localized field which enhance a range of linear and nonlinear phenomena.

The metal nanostructures fundamental property i.e. LSPs demonstrates the huge optical absorption and scattering cross sections. The SP resonance depends on the physical parameters such as size, shape and alignment. By controlling these factors, permits us to design of innovative devices that represent a breakthrough with conventional ones. The characteristics of the SPs in the metallic nanostructures permit us to realise regions forbidden by traditional optics. Metallic nanostructures efficiently mediate interactions between radiation and other semiconductor components in the devices. These applications include completely new approaches to problems not yet solved and improvement of well-established optical processes. However, the present-day knowledge is solid enough to develop a vast range of applications, some of them already achieved, others in development and some others yet to be addressed.

The increase in the conversion efficiency and reduced cost are the constant pursuit for the optoelectronic devices such as photodetectors and photovoltaics. Among various approaches to enhance efficiency and reduce cost, plasmonic structures have received much attention in the recent

years. Integrating these metallic nanostructures with the semiconductors, the optical absorption efficiency of the device can be increased which ultimately results into enhanced efficiency with lower cost. Various methods are available to incorporate plasmonically active metal nanostructures such as thermal evaporation and annealing, sputtering, colloidal metal nanoparticles NPs. Each method is associated with its precise control over the spectral position and line width of the plasmon resonance. As the individual components as well as the integration structures differ from one another, each of these works offers important insights on the characteristic influence that plasmons have on the particular devices and implications for future application.

Intense research has been forthcoming to delve the optical properties of a variety of metallic nanostructures for effective control over concentrating light into nanoscale volumes. Plasmonics for extreme light concentration higher efficiency solar cells, and techniques for locally controlling catalytic and thermally stimulated processes. As well as acting as an interface with the nanoscale, plasmonic structures can also change light–matter interactions at a very fundamental level.

1.1.7 Constitution of Thesis:

The present thesis is inspired from several interesting properties own by the metal nanoparticles for example surface plasmon resonance in the solar spectrum, far field and near field effect of the surface plasmons, enhancement in the EM field. Due to above mentioned effects metal nanostructures finds extraordinary applications in both fundamental and applied aspects.

Here we assemble investigations based on metal nanostructures/ semiconductor hybrid materials in the optical absorption enhancement and subsequent application in the photon conversion into electrical current. Chapter **I** expresses the review of some basic of surface plasmon theory of metal

nanostructures and its potential applications are discussed to explain their impact in diverse fields like optoelectronics, photocatalysis, chemical sensing.

Chapter **II** demonstrates the fabrication of functionalized rGO electrodes which were assembled with gold nanoparticles (AuNPs). Graphene with 2 D hexagonal arrangement same as the graphite has been widely explored for practical applications such as transparent electrodes, field effect transistors, photodetectors, chemical sensors and in photocatalysis etc. Its equivalents like graphene oxide (GO) and reduced graphene oxide (rGO) altogether important for the same applications. However, they possess low conductivity as in rGO and almost insulating nature of the GO due oxygen functional groups and defects. These functional groups can be reduced or utilized for their effective application in the intended area.

In our approach we have tried to functionalize these groups with silane and one on which click reaction has been carried out. Citrate capped gold nanoparticles (AuNPs) are then self-assembled electrostatically on the amine terminals. Such functionalized graphene and AuNPs hybrid is studied for their photoelectrochemical properties. The electrochemical cyclic voltammetry and impedance clearly indicates the decreased resistance for click modified than the simple linear chain silane modified graphene surface. The wavelength dependent photocurrent suggests the plasmon effect of gold nanoparticles.

Chapter **III** describes the effect of metal nanoparticles on the semiconductor heterojunction between n-SiNWs and TiO_2. A TiO_2 thin layer was deposited on the surface of the SiNWs by dip coating method followed by thermal heating. For gold nanoparticles sensitization, a simple soaking of

heterojunction in the gold salt solution has been carried out. The materials were characterized for the optical absorption, the photoluminescence as well as the photocurrent enhancement was studied.

The increased photocurrent observed for the heterojunction can be correlated with the enhanced optical properties of the heterojunction. Higher photoluminescence was observed for TiO_2 due to near electric field enhancement by the nanoparticles' LSPRs involvement. The improved photoelectrochemical properties of such heterojunction can be related to generation of higher number of excitons in the TiO_2 and transfer of metal hot electrons into the conduction band of TiO_2.

In the chapter **IV** we have fabricated heterojunction of SiNWs/CuS. Copper sulphide was deposited by radio frequency magnetron sputtering on the H-terminated silicon nanowires. The solid state device have been studied for the photodetection. Later we have dropcasted gold nanorods on the surface of the photodiode and the performance of the device is evaluated.

Finally, chapter **V** includes major conclusions of the present study and future directions for the effective utilization of metal nanoparticles for their potential applications in optoelectronic devices such as solar cells, photodetectors, light emitting diodes etc.

1.1.8 References:

1] R. H. Ritchie, *Phys Rev*, **1957**, 106, 874.

2] J. M. Pitarke, V. M. Silkin, E. V. Chulkov, and P. M. Echenique, *Rep. Prog. Phys.* **2007**, 70, 1.

3] H. Raether, *Surface plasmons: Springer, Berlin*, **1988.**

4] S. V. Boriskina, H. Ghasemi and G. Chen, *Materials Today*, **2013**, 16 (10), 375.

5] M. G. Cottam, *Introduction to surface and superlattice exciations*, Cambridge University Press: New York, **1989.**

6] W. L. Barnes, A. Dereux and T. W. Ebbesen, *Nature*, **2003**, 424, 824.

7] K. A. Willets and R. P. Van Duyne, *Annu Rev Phys Chem*, **2007**, 58, 267.

8] J. A. Schuller et al, *Nature. Mater.* **2010**, 9 (3), 193.

9] M.I. Stockman, *Opt. Express*, **2011**, 19 (22), 22029.

10] M. R. Beversluis, A. Bouhelier and L. Novotny, *Physical Review B*, **2003**, 68 (11).

11] L. Börnstein, *Numerical data and functional relationships in science and technology, group iii: crystal and solid state physics*, John Wiley & Sons **1982**.

12] X. Huang, I. H. El-Sayed, W. Qian and M. A. El-Sayed, *J. Am. Chem. Soc.* **2006**, 128, 2115.

13] K. L. Kelly, E. Coronado, L. L. Zhao and G. C. Schatz, *J. Phys. Chem. B*, **2003**, 107, 668.

14] C. Noguez, *Opt. Mat*. **2005**, 27, 1204.

15] I. O. Sosa, C. Noguez and R. G. Barrera, *J. Phys. Chem. B*, **2003**, 107, 6269.

16] E. K. Payne, K. L. Shuford, S. Park,G. C. Schatz and C. A. Mirkin, *J. Phys. Chem. B*, **2006**, 110, 2150.

17] K. S. Lee and M. A. El-Sayed, *J. Phys. Chem. B*, **2005**, 109, 20331.

18] http://www.silmeco.com/knowledge-base/hot-spots

19] X. Fan, W. Zheng and D. J Singh, *Light: Science & Applications*, **2014**, 3.

20] C. Noguez, *J. Phys. Chem. C*, **2007**, 111 (10).

21] S. A. Maier, *Plasmonics: Fundamentals and applications*, 1st ed. Springer: New York, **2007**.

22] C. F. Bohren, *Absorption and scattering of light by small particles*, 1st ed. John Wiley & Sons: New York, **1983**.

23] J. H. Fendler and E. Hutter, *Adv Mater.* **2004**, *16*, 1685.

24] P. K. Jain, K. S. Lee , I. H. El-Sayed and M. A. El-Sayed , *J. Phys. Chem. B*, **2006**, 110 (14), 7238.

25] S. Kawata (Ed.), *Near-Field Optics and Surface Plasmon Polaritons*, Springer, Berlin, **2001**.

26] W. L. Barnes, A. Dereux and T. W. Ebbesen, *Nature*, **2003**, 424, 824.

27] J. Z. Jhang and C. Noguez, *Plasmonics*, **2008**, 3(4), 127.

28] S. Khatua, W. S. Chang, P. Swanglap, J. Olson and S. Link, *Nano Lett.* **2011**, 11 (9), 3797.

29] A. Tao, P. Sinsermsuksakul and P. D. Yang, *Angew Chem Int Ed*. **2006**, 45, 4597.

30] F. Baletto and R. Ferrando, *Rev Mod Phys*. **2005**, 77, 371.

31] Y. Sun and Y. Xia, *Science*, **2002**, 298, 2176.

32] W. R. Erwin, H. F. Zarick, E. M. Talbert and R. Bardhan, *Energy Environ. Sci*. **2016**, 9, 1577.

33] T. Wijesinghe and M. Premaratne, *Optics Express*, **2012**, 20 (7), 7151.

34] César Clavero, *Nature Photon.* **2014**, 8, 95.

35] M. L. Brongersma, N. J. Halas and P. Nordlander, *Nature Nanotech.* **2015**, 10, 25.

36] R. Sundararaman, P. Narang, Adam S. Jermyn, William A. Goddard III and Harry A. Atwater, *Nature. Comm.* **2014**, 5.

37] C. Kittel, *Introduction to Solid State Physics*, 7th ed. Wiley, **1995.**

38] Y. Peter, *Fundamentals of Semiconductors*, Berlin: Springer-Verlag, **2010.**

39] M. D. Regulacio and M. Y. Han, *Acc Chem Res*. **2016**, 49 (3), 511.

40] A. M. Smith and S. Nie, *Acc Chem Res*. **2010**, 43 (2), 190.

41] G. Cao and C. Brinker, *Annual review of nano research*, Volume 2, World Scientific Pub. Co. **c2008**.

42] A. K. Geim and K. S. Novoselov, *Nature Mater*. **2007**, 6, 183-191.

43] Y. Zhu, S. Murali, W. Cai, L. Xuesong, J. Suk, J. Potts and R. Ruoff, *Adv. Mater.* **2010**, 22, 3906.

44] L. Ju et al, *Nature Nanotechnol*. **2011**, 6, 630.

45] S. Bae et al, *Nature Nanotechnol.* **2010**, 5, 574.

46] T. Mueller, F. Xia and P. Avouris, *Nature Photon.* **2010**, 4, 297.

47] J. Liu, M. Durstockb and L. Dai, *Energy Environ. Sci.* **2014**, 7, 1297.

48] T. Yeh, F. Chan, C. Hsieh, and H. Teng, *J. Phys. Chem. C*, **2011**, 115, 22587.

49]. M. D. Kelzenberg et al and H. A. Atwater, *Nature Mater.* **2010**, 9 (3), 239.

50] K. Q. Peng, X. Wang, X. L. Wu, and S. T. Lee, *Nano Lett.* **2009**, 9 (11), 3704.

51]. C. Lee, S. Y. Bae, S. Mobasser, and H. Manohara, *Nano Lett.* **2005**, 5 (12), 2438.

52] H. Li, R. Jia, C. Chen, Z. Xing, W. Ding, Y. Meng, D. Wu, X. Liu, and T. Ye, *Appl. Phys. Lett.***2011**, 98(15), 151116.

53] E. S. Kolesar, V. M. Bright, and D. M. Sowders, *Thin Solid Films*, **1996**, 290–291, 23–29.

54] J. Q. Xi, M. F. Schubert, J. Kim, E. F. Schubert, M. Chen, S. Y. Lin, W. Liu, and J. A. Smart, *Nature Photonics*, **2007**, 1 (3), 176.

55] S. Chhajed, M. F. Schubert, J. K. Kim, and E. F. Schubert, *Appl. Phys. Lett.* **2008**, 93 (25), 251108.

56] M. L. Kuo, D. J. Poxson, Y. S. Kim, F. W. Mont, J. K. Kim, E. F. Schubert, and S. Y. Lin, *Opt. Lett.* **2008**, 33 (21), 2527.

57] L. Sainiemi, V. Jokinen, A. Shah, M. Shpak, S. Aura, P. Suvanto, and S. Franssila, *Adv. Mater.* **2011**, 23 (1), 122.

58] C. H. Hsu, H. C. Lo, C. F. Chen, C. T. Wu, J. S. Hwang, D. Das, J. Tsai, L. C. Chen, and K. H. Chen, *Nano Lett.* **2004**, 4 (3), 471.

59] Y. F. Huang et al and L. C. Chen, *Nature Nanotechnol.* **2007**, 2 (12), 770.

60] C. Wu, C. H. Crouch, L. Zhao, J. E. Carey, R. Younkin, J. A. Levinson, E. Mazur, R. M. Farrell, P. Gothoskar, and A. Karger, *Appl. Phys. Lett.* **2001**, 78 (13), 1850.

61] Y. Kanamori, M. Sasaki, and K. Hane, *Opt. Lett.* **1999**, 24 (20), 1422.

62] G. Jia, M. Steglich, I. Sill, and F. Falk, *Sol. Energy Mater. Sol. Cells*, **2012**, 96, 226.

63]. J. M. Weisse, C. H. Lee, D. R. Kim, and X. Zheng, *Nano Lett.* **2012**, 12 (6), 3339.

64]. J. Zhu, Z. Yu, G. F. Burkhard, C. M. Hsu, S. T. Connor, Y. Xu, Q. Wang, M. McGehee, S. Fan, and Y. Cui, *Nano Lett.* **2009**, 9 (1), 279.

65]. K. Rasool, M. A. Rafiq, C. B. Li, E. Krali, Z. A. K. Durrani, and M. M. Hasan, *Appl. Phys. Lett.* **2012**, 101 (2), 023114.

66]. J. Y. Jung, Z. Guo, S. W. Jee, H. D. Um, K. T. Park, and J. H. Lee, *Opt. Express*, **2010**, 18, A286.

69] H. A. Atwater and A. Polman, *Nature Mater.* **2010**, 9 (3), 205.

70] K. R. Catchpole and A. Polman, *Opt. Express*, **2008**, 16 (26), 21793.

71] A. Chutinan and S. John, *Phys. Rev. A*, **2008**, 78 (2), 023825.

72] P. Matheu, S. H. Lim, D. Derkacs, C. McPheeters, and E. T. Yu, *Appl. Phys. Lett.* **2008**, 93 (11), 113108.

73] D. M. Schaadt, B. Feng, and E. T. Yu, *Appl. Phys. Lett.* **2005**, 86 (6), 063106.

74] S. Pillai, K. R. Catchpole, T. Trupke, and M. A. Green, *J. Appl. Phys.* **2007**, 101 (9), 093105.

75] K. R. Catchpole and A. Polman, *Appl. Phys. Lett.* **2008**, 93 (19), 191113.

76] D. Derkacs, S. H. Lim, P. Matheu, W. Mar, and E. T. Yu, *Appl. Phys. Lett.* **2006**, 89 (9), 093103.

77] F. J. Haug, T. Söderström, O. Cubero, V. Terrazzoni Daudrix, and C. Ballif, *J. Appl. Phys.* **2008** 104(6), 064509.

78] C. Rockstuhl, S. Fahr, and F. Lederer, *J. Appl. Phys.* **2008**, 104 (12), 123102.

79] C. Hägglund, M. Zäch, G. Petersson and B. Kasemo, *Appl. Phys. Lett.* **2008**, 92 (5), 053110.

80] M. Kirkengen, J. Bergli, and Y. M. Galperin, *J. Appl. Phys.* **2007**, 102 (9), 093713.

81] F. J. Tsai, J. Y. Wang, J. J. Huang, Y. W. Kiang, and C. C. Yang, *Opt. Express*, **2010**, 18, A207.

82] V. E. Ferry, L. A. Sweatlock, D. Pacifici, and H. A. Atwater, *Nano Lett.* **2008**, 8 (12), 4391.

83] T. D. Heidel, J. K. Mapel, M. Singh, K. Celebi and M. A. Baldo, *Appl. Phys. Lett.* **2007**, 91 (9), 093506.

84] S. S. Kim, S. I. Na, J. Jo, D. Y. Kim, and Y. C. Nah, *Appl. Phys. Lett.* **2008,** 93 (7), 073307.

85] C. Hägglund, M. Zäch, and B. Kasemo, *Appl. Phys. Lett.* **2008**, 92 (1), 013113.

86] J. Y. Wang, F. J. Tsai, J. J. Huang, C. Y. Chen, N. Li, Y. W. Kiang, and C. C. Yang, *Opt. Express*, **2010**, 18 (3), 2682.

87] Y. A. Akimov, W. S. Koh and K. Ostrikov, *Opt. Express*, **2009**, 17(12), 10195.

88] P. Reineck et al, *Adv. Mater*. **2012**, 24, 4750.

89] H. R. Stuart and D. G. Hall, *Appl. Phys. Lett.* **1998**, 73, 3815.

90] Y. Liu et al and X. Duan, *Nature Commun.* **2011**, 2, 579.

91] M. W. Knight, H. Sobhani, P. Nordlander and N. J. Halas, *Science*, **2011**, 332, 702.

92] A. Sobhani, M. W. Knight, Y. Wang, B. Zheng, N. S. King, L. V. Brown, Z. Fang, P. Nordlander and N. J. Halas, *Nature Commun*. **2013,** 4, 1643.

93] M. Nazirzadeh, F. Atar, B. Turgut and A. K. Okyay, *Scientific Reports*, **2014**, 4, 7103.

94] Y. Liu, R. Cheng, L. Liao, H. Zhou, J. Bai, G. Liu, L. Liu, Y. Huang and X. Duan, *Nature Commun.* **2011**, 2(579).

95] A. J. Bard and M. A Fox, *Acc. Chem Res.* **1995**, 28, 141.

96] Z. Liu Z, W. Hou, P. Pavaskar, M. Aykol and S. B. Cronin, *Nano Lett.* **2011**, 11, 1111.

97] M. Ni, M. K.H. Leung, D. Y. C. Leung and K. Sumathy, *Renew. Sust. Energy Rev.* **2007**, 11, 401.

98] T. Torimoto , H. Horibe , T. Kameyama , K. Okazaki , S. Ikeda ,M. Matsumura , A. Ishikawa and H. Ishihara , *J. Phys. Chem. Lett.* **2011**, 2, 2057.

99] J. Li, S. K. Cushing, P. Zheng, F. Meng, D. Chu and N. Wu, *Nature Commun.* **2013**, 4.

100] Z. W. Seh, S. Liu, M. Low, S. Y. Zhang, Z. Liu, A. Mlayah and M. YongHan, *Advance Mater.* **2012**, 24 (17), 2310.

101] K. Awazu, M. Fujimaki, C. Rockstuhl, J. Tominaga, H. Murakami, Y. Ohki, N. Yoshida and T. Watanabe, *J. Am. Chem. Soc.* **2008**, 130, 1676.

102] G. K. Larsen, W. Farr, and S. E. Hunyadi Murph, *J. Phys. Chem. C*, **2016**, *120* (28), 15162.

103] X. Yang et al, *J. Am. Chem. Soc*. **2015**, 137, 10104.

104] J.R. Adleman et al, *Nano Lett.* **2009**, 9 (12), 4417.

105] S. Linic, P. Christopher and D.B. Ingram, *Nature Mater.* **2011**, 10 (12), 911.

106] M. Sun and H. Xu, *Small*, **2012**, 8 (18), 2777.

107] P. Christopher, H. Xin, and S. Linic, *Nature Chem.* **2011**, 3 (6), 467.

108] Sebastian Schlücker, *Angew. Chem. Int. Ed.* **2014**, 53 (19), 4756.

109] https://en.wikipedia.org/wiki/Surface enhanced Raman spectroscopy.

110] L. Ru and Etchegoin, *Principles of Surface-Enhanced Raman Spectroscopy*, 1st Edition, Elsevier, **2008**.

111] N. H. Kim, S. J. Lee and M. Moskovits, *Nano Lett.* **2010**, 10, 4181.

112] J. F. Li, *Nature*, **2010**, 464, 392.

113] E. J. Blackie, E. Le Ru and P. G. Etchegoin, *J. Am. Chem. Soc*. **2009**, 131 (40), 14466.

114] A. Campion and P. Kambhampati, *Chemical Society Reviews*, **1998**, 27 (4), 241.

115] J. R. Lombardi, R. L. Birke, T. Lu and J. Xu, *The Journal of Chemical Physics*, **1986**, 84 (8), 4174.

Plasmon Enhanced Photocurrent Generation from Click-Chemically Modified Graphene

Functionalized rGO (reduced graphene oxide) electrodes were prepared, one having linear carbon chain and other with triazole aromatic ring (via cycloaddition reaction). The electrochemical properties of the functionalized rGO have been investigated alongwith visible-light response after covalent linking of gold nanoparticles (AuNPs) on the linkers.

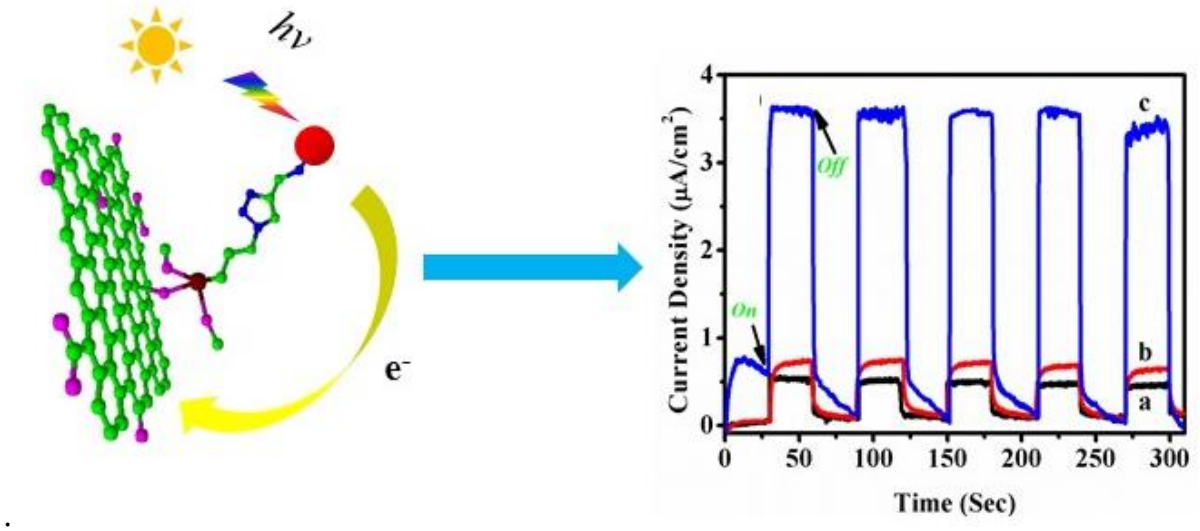

Schematics of the AuNPs functionalize graphene and its photocurrent performance.

Cyclic voltammetry (CV) and impedance measurements suggest fast electron transfer kinetics on account of the low resistance offered by the click-modified rGO surface. The introduction of triazoles offers the efficient bridge for electron transport between the AuNPs and reduced graphene oxide.

2.1 Introduction:

Graphene is one atom thick 2D structure of carbon network. It possess highly impressive properties e.g. electrical conductivity (theoretical ~ 200000 cm^2 V^{-1} s^{-1}), thermal conductivity (5300 W m^{-1} k^{-1}) , mechanical properties and high surface area (2360 cm2).[1-5] It has zero band gap and ballistic electron transport due to linear E-k dispersion relation. Based on these excellent properties it is extensively used in variety of applications ranging from electronics[6,7], energy storage[8,9] and sensing devices.[10-12] However, graphene has many obstacles in the large scale applications e.g. it cannot be synthesized in bulk quantity or not suitable for surface modification due to lack of chemical functionalities. Additionally, the hydrophobic nature and absence of a bandgap limit graphene's utility in water-based applications.[13]Analogues of graphene, Graphene oxide (GO) and partially reduced graphene oxide (rGO) have numerous electroactive sites owing to oxygen functionalities on the basal plane and the edges; they are also called as functionalised graphene.[14] These functionalities allow non-covalent and covalent based chemistry on its surface for practical application of graphene in the devices. Self-assembled monolayers (SAMs), which are ultrathin molecular films, can be used to modify the surface and influence the electronic properties of graphene.[15-18] Covalent bonding facilitates and controls the transport of electrons and thus can effectively charge and discharge electrons onto the Au nanoparticles by means of linker molecules. Such molecular conducting junctions are necessary for controlled, efficient electron transfer and excitation energy transfer between two electrodes in which one acts as a donor and other one act as an acceptor. Conjugated π-systems are of special interest in this respect. As a spacer or bridge, such systems significantly affect the rate of electron transfer, which is dependent on the length and electronic structure of the bridge, the donor–bridge energy gap for injection, the spectral density coupling of molecules and the electrode.[19-21] Aromatic

triazoles have been used as potential connecting bridge to facilitate photoelectron transfer through the involvement of a conjugative p network in intramolecular processes.[22-24] The Cu-catalysed azide–alkyne cycloaddition reaction between terminal alkynes and azides is famously known as "click chemistry" or Huisgen 1,3-dipolar cycloaddition. It has found wide applications in organic chemistry, polymer chemistry, supramolecular chemistry, drug discovery and so on.[25-27] Click chemistry is one of the strategies that can be implemented easily on various surfaces: for example, silicon[28], semiconductor nanoparticles and metal nanoparticles[29], graphene[30], graphene oxide[31] and so forth.

Plasmonic metal nanoparticles like Au and Ag possess higher scattering and absorption cross section and can be utilized in various applications like non-linear optics[32-34], surface-enhanced Raman scattering (SERS)-based sensors[35-37], energy harvesting and photocatalysis.[38-40] Integration of gold nanoparticles with the semiconductor structures have been investigated for their enhanced photoluminescence and photocurrent in hybrids like TiO2/Au[41,42], ZnO/Au[43-45]. Dye-sensitised solar cells (DSSCs), photochromic molecules such as PdPc (palladium phthalocyanine)[46,47] and porphyrins[48]showed increase in the photocurrent[49] due to plasmonic AuNPs. Localised surface plasmons on the AuNPs significantly improve photocurrent signals by intense photon absorption and they induce a large electromagnetic field adjacent to its surface. Covalently immobilised AuNPs on the rGO surface through organic linkers has been suggested as a means of achieving controllable transport in memory devices.[50]

In this chapter, we have fabricated functionalized rGO electrodes by different organic molecules. First, silanization of rGO surface was carried out by simple hydrolysis process with Azidopropyltriethoxysilane (AzPTES) and aminopropyltrimethoxysilane (APTMS). The copper-mediated click chemistry reaction was carried out on AzPTES functionalized rGO surface which

converts azide into an aromatic 1,2,3-triazoles. Finally, aromatic and non-aromatic linkers were attached on the rGO surface having amine group on the terminal end. Citrate capped AuNPs were subsequently self-assembled on the amine terminal end.

The optical and electrochemical properties have been studied to understand the effect of metal nanoparticles. We studied the influence of AuNPs assembled on the rGO surface for plasmon enhanced photocurrent generation. The interfacial properties of the covalently modified rGO are considerably altered by gold nanoparticle immobilisation. The aromatic 1,2,3 triazole acts as a perfectly suited linker between rGO and AuNPs for efficient charge transfer. After photoexcitation of Au nanoparticles, efficient charge separation and electron transfer occurs to the graphene through the molecular linkers. The maximum photocurrent is achieved when a triazole interfaces with the gold nanoparticles, thus indicating the necessity of π- conjugation for the charge transfer.

2.2 Experimental Methods:

2.2.1 Synthesis of GO and rGO

Well known hummers method is used to synthesise Graphene oxide (GO) where natural graphite exfoliation is carried out in the acidic medium. The reduction of graphene oxide was performed by irradiating its aqueous dispersion (50 mg, 1 mg/ml) with UV light source for 6 hrs (3 mW, 250–400 nm).[52] The reduction of GO can be confirmed from the dark brown colouration which starts to settle from its aqueous solution. The samples were collected by centrifugation at 12000 rpm and redispersed in the ethanol and used for further studies.

2.2.2 Spray Deposition and Functionalization of rGO:

Transparent conducting oxides plates, here FTO (resistivity: 15 Ωcm^{-2}, Solaronix, Switzerland) was used as conducting electrode. Small pieces of FTO were cut into pieces of dimensions 1cm x 1 cm. FTO-coated glass plates were pre-cleaned by acetone, isopropyl alcohol and finally with water under ultrasonication and dried in N_2 gas. The dispersion of rGO in ethanol was spray coated with air blowing on the conducting surface of the preheated FTO at 150º C until the desired thickness was achieved. Finally, the rGO layer on the FTO coated glass was heated at 150º C for 2 hrs until complete removal of solvent and to ensure film adhesion and better contact of rGO sheets onto the FTO surface. The FTO/rGO plates were immersed in a solution of APTMS and AzPTES in ethanol for 12 hr for amine and azide functionalization, respectively. After the functionalization of the FTO/rGO plates with amine and azide, the plates were washed with ethanol and water and dried under N_2 gas. The click attachment of propargylamine was performed on the azide-terminated FTO/rGO electrodes. The electrodes were kept in the solution that contained propargylamine (50 ml), copper sulphate pentahydrate ($CuSO_4 \cdot 5H_2O$, 1 mM) and sodium ascorbate (1 mM) in ethanol (10 ml) for 12 hr at room temperature. The electrodes were then washed with ethanol and water several times until the excess amount of physically adsorbed reactants were removed from the substrate and dried under N_2 gas.

2.2.3 Synthesis of Gold Nanoparticles:

Gold nanoparticles were prepared by the citrate reduction method. Briefly, $HAuCl_4$ (20 ml, 1 mM) was heated in a water bath at 120º C for 15 min and citrate solution (20 ml, 1 mM) was added to the $HAuCl_4$ solution at once. The yellow solution of the gold ions gradually turned wine red, thus

indicating the formation of gold nanoparticles. Heating was continued for 15 min and then the mixture was allowed to cool to room temperature. The functionalised FTO/rGO plates were then immersed in the as-synthesised gold nanoparticle solution (10 ml, pH~ 6.4) for 30 min. After that, the plates were washed in a water stream to remove physically adsorbed gold nanoparticles and then dried in N_2 gas.

2.3 Characterization Section:

2.3.1 Morphology:

Vibrational characteristics after covalent functionalization of rGO surface and after attaching gold nanoparticles were studied by ATR-FTIR spectra which were obtained by FTIR Spectrum GX-Perkin Elmer instrument. Atomic force microscopy images were taken in tapping mode with nanoscope-IV multimode scanning probe microscope. Jasco V-570 spectrometer is used for UV–Visible and diffused reflectance spectrum recording. Morphological characterization of the samples was examined by using a Quanta 200 3D, FEI scanning electron microscope (SEM). High resolution transmission electron microscope (HR-TEM) images were taken by using FEI Technai 300 keV. The Raman spectra collected using LabRAM HR800 from JY Horiba, France with laser wavelength of 632.84 nm (He-Ne Laser, 10mW of power) and 2μm spot size. XPS data were acquired fromVG Microtech Multilab ESCA-3000 spectrometer equipped with a non-monochromatic Mg (Kα)-Xray (1253.6 eV) source.

2.3.2 Electrochemical Measurements:

Electrochemical measurements along with photocurrent measurements were performed on Potentiostat (Biologic SP 300) coupled with 300W Xenon lamp (ScienceTech) under AM 1.5 conditions.

Electrochemical characterization is carried out under three-electrode configuration where FTO/rGO and functionalized FTO/rGO were used as working electrode, Ag/AgCl as a reference electrode and counter electrode was Platinum foil. Aqueous KCl (0.1 M) solution was used as electrolyte with 10 mM potassium ferrocyanide which served as a redox couple. Before experiment the solution was deaerated by purging N_2 gas for 1 hr which removes dissolved oxygen from the system. Copper wire is soldered on conducting side of the FTO.

2.3.3 Photoelectrochemical Measurements:

For photocurrent measurement 1 M Na_2SO_4 aqueous solution was used as electrolyte and an electron donor. Fixed area of 5 mm X 5 mm of the working electrode was exposed to the light. A Xenon lamp in the solar simulator was the white light source having intensity of 100 mW/cm^2. Light emitting diodes purchased from Luxeon star, Canada were used for the wavelength dependent photocurrent measurements.

2.4 Results and Discussion:

Graphene oxide was first synthesised by Hummers method with acid-mediated oxidation and exfoliation of graphite powder.[51]In this work photoinduced conversion of GO to rGO is carried out using ultraviolet irradiation. Reduction of aqueous dispersion of GO was done by exposing the solution under UV light (3 mW) for six hours. GO significantly absorbs UV radiation and generate photoexcited electrons; relaxation of these electrons causes phonon vibration in the graphene lattice through thermal energy transfer. This creates localised heating and simultaneous removal of oxygen functionalities from the surface. In such process hydrated or solvated electrons can trigger the reduction of the graphene oxide.[51,52]

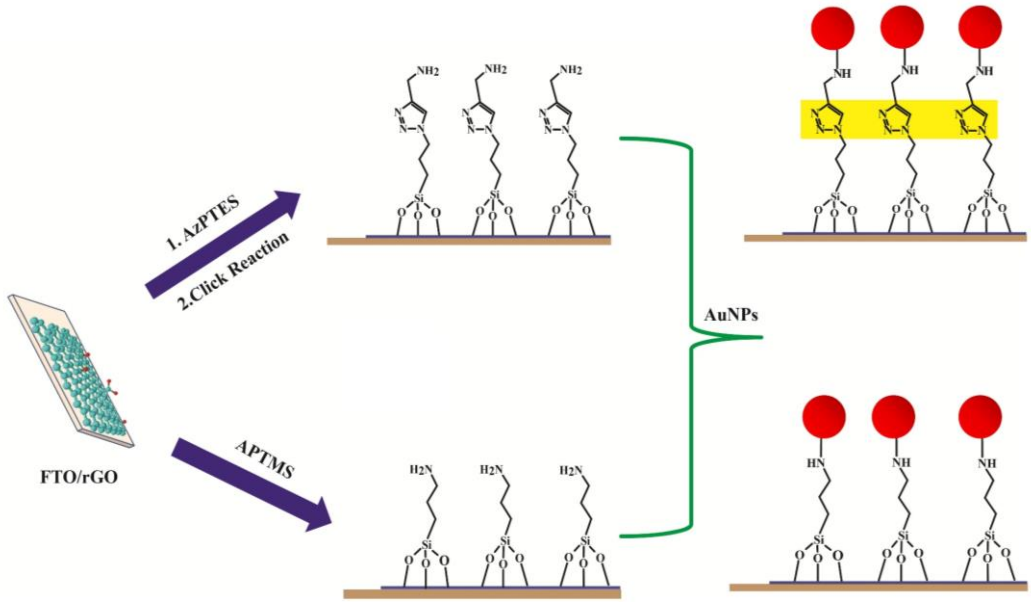

Scheme 2.1. Schematic of the GO surface functionalisation and immobilisation of AuNPs.

Conducting side of the cleaned fluorine-doped tin oxide (FTO) substrate was spray coated with reduced graphene oxide. The surface of rGO deposited on FTO was then modified chemically by covalent reactions. The above **scheme 2.1** represents the process of the self -assembled monolayers

formation on the rGO. Two types of organic linkers were attached onto the rGO surface by hydrosilylation. In first approach we used aminopropyltrimethoxysilane (APTMS) which is linear chain molecule and in the second azidopropyltriethoxysilane (AzPTES) followed by click reaction. After click functionalization with propargylamine, a triazole is formed which is an aromatic moiety. Both the reaction at the end will generate amine groups which can be subsequently used for the AuNPs attachment onto the functionalized rGO/FTO substrates.

2.4.1 Optical, AFM and SEM Analysis:

Morphological surface characteristics of spray deposited rGO on FTO are studied by optical, AFM images. Optical images reveal the brownish coloured thin film of the rGO on the FTO surface. AFM shows highly rough surface of FTO which indicates granules of FTO which can be formed after sputter coating of FTO on the glass.

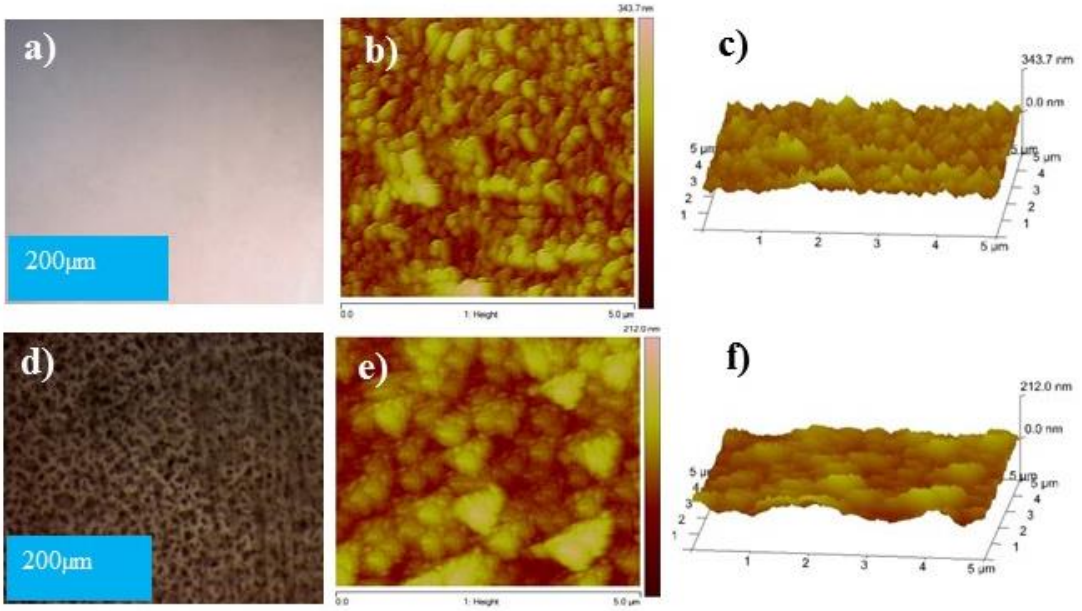

Figure 2.1. Optical microscopic images **a)** bare FTO, **d)** Spray coated rGO on FTO. Surface roughness analysis by AFM **b)** FTO top view and **c)** 3D plot. **e)** AFM top view and **f)** 3D plot after spray coating of rGO on FTO.

FTO roughness decreases after of spraying of rGO solution indicating the deposition of active layer of rGO as can be seen in the **Figure 2.1c** and **d**. The roughness of bare FTO was 36.7 nm which is reduced to 25.4 nm after rGO deposition as calculated from the AFM images (**Fig 2.1e** & **f)**. Scanning electron microscopic images reveal the rough nature of the bare FTO surface and after spray depositing rGO sheets on the FTO surface. We can clearly see the flat rGO sheets on the FTO with edges partly protruding out of the surface shows the effectiveness of the spray deposition as in the **Figure 2.2A and B**.

2.4.2 Fourier Transform Infrared spectroscopy and Raman measurement:

The graphene oxide, reduced graphene oxide, chemically modified rGO substrates along with gold nanoparticles assembled rGO were characterised by FTIR (**Figure 3a**). The oxygen functionalities present on the GO surface includes alcoholic, carbonyl, C=C and epoxy groups abundantly which was confirmed from the various IR vibrational modes at 3363, 1732, 1630 and 1059 cm^{-1}.

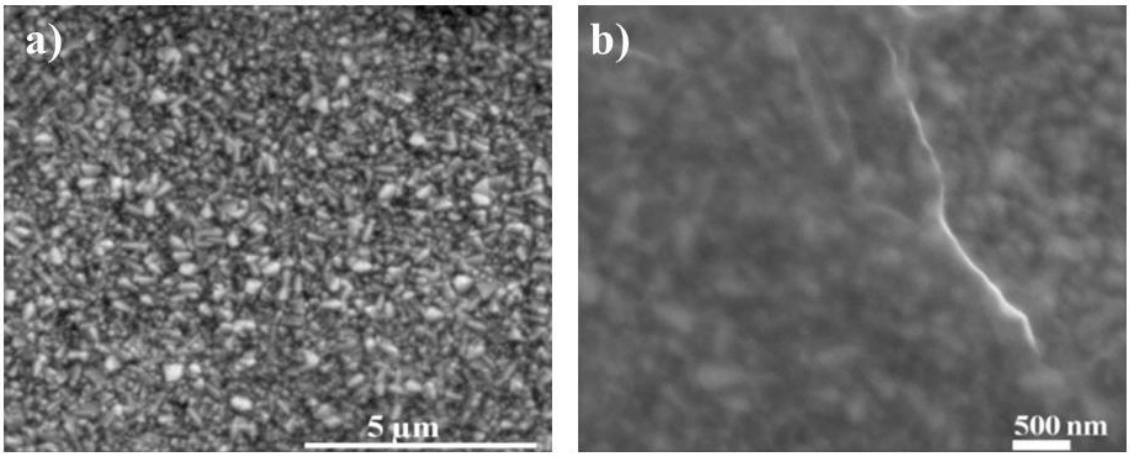

Figure 2.2. Scanning electron microscope images **a)** bare FTO, **b)** Spray coated rGO on FTO.

The reduction of GO sheets can be observed as the IR intensity of OH and C=O group on the GO is decreased upon irradiation with UV light. However it also indicates that presence of sufficient functionalities are available over their surface for further chemical modification (**Figure 2.3A – a, b**).

The silanization of rGO is based on silane chemistry in which -OH or -COOH groups are necessary for covalent attachment onto the surface. Briefly, the silane reacts with the above-mentioned functional groups by hydroxylation. Such SAMs have excellent stability under ambient atmosphere, which simultaneously passivates the electronic defects on the graphene edges and surface.[7] The FTIR spectra of APTMS and AzPTES-modified rGO show a characteristic Si-O-C peak at 1100 cm^{-1} alongwith additional peaks at 740 and 890 cm^{-1} could be assigned to Si-O-Si and Si-O-C symmetric stretching modes. The peak at 2090 cm^{-1} correspond to azide vibrational mode as in **Figure 2.3A (c)**.

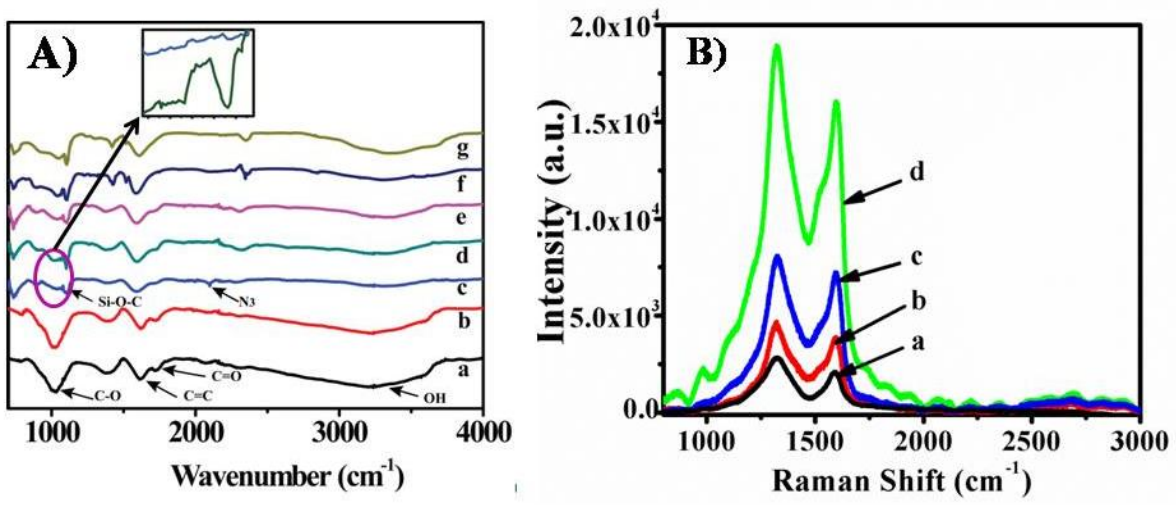

Figure 2.3. A) ATR/FTIR spectra of **a)** GO, **b)** rGO, **c)** N_3/rGO, **d)** click/rGO, **e)** APTMS/rGO, **f)** AuNPs(click)/rGO and **g)** AuNPs(APTMS)/rGO. **B)** Raman spectra of a) GO, b) rGO, **c)** AuNPs(APTMS)/rGO and **d)** AuNPs(click)/rGO.

In the click reaction 1,3-dipolar addition of propargylamine was carried out in the presence of Copper as catalyst and sodium ascorbate as a reducing agent. Cu (I) generated after the reduction formed a complex with propargylamine by reacting with a terminal alkyne, which then selectively added to azide to form 1,2,3-triazole. After click reaction the azide peak (2090 cm^{-1}) completely disappeared as can be seen in the IR spectra (**Figure 2.3A (d)**), thus indicating successful click attachment of the propargylamine on the azide-terminated GO surface, whereas the triazole ring peak appears at 1066 cm^{-1} after the click reaction. The click reaction on the N_3-rGO ultimately terminates the rGO surface with the amine end, which electrostatically immobilises citrate-capped AuNPs. The appearance of peaks at 1460 and 1574 cm^{-1} represent C-N stretching and N-H bending modes of amide groups, which further confirms the covalent attachment of AuNPs onto the functionalised rGO surface.[54]

Raman spectroscopy (633 nm excitation wavelength) was used to investigate the structural changes and interaction effects of gold nanoparticles with the graphene surface. Graphene oxide displays two distinctive peaks: the G band for the graphitic mode that arises from the first-order scattering of the E_{2g} phonon (~ 1320 cm^{-1}) at the Brilliouin zone centre and the in-plane breathing modes (1590 cm^{-1}) of the six atom ring (A_{1g} phonon) respectively in the Raman spectrum (**Figure 2.3B**) . The graphitic nature of the GO can be measured from the ID/IG ratio. The ratio for the GO and rGO was found to be 1.83 and 1.63. The ID/IG ratio indicates the average size of sp^2 domains in the graphene. In our case the decrease in the ratio is attributed to desorption of the oxygen functionalities, that is, the removal of defects with the introduction of sp^2 domains at different levels and subsequent reduction of the GO surface.[27] The ratio for APTMS and the click-modified rGO surface was found to be 1.56 and 1.49, respectively. AuNPs deposited on the APTMS and click-functionalized rGO surface shows enhanced Raman signals of the rGO bands. The gold nanoparticles interfaced with APTMS showed

a 97% enhancement in the D band, whereas a 426% enhancement was observed for the click-modified surface. The enhancement could be attributed to electromagnetic (excitation of LSPs) or chemical mechanisms (charge-transfer mechanism).[28] The enhanced Raman intensity of the D and G bands in the Raman spectra of the AuNPs on the click-modified rGO surface can be attributed to the involvement of the resonating SPs on the surface of the Au nanoparticles, which would induce concentrated electromagnetic fields around the nanoparticle as well as charge transfer because of the linkers used for the covalent assembly of AuNPs.

2.4.3 Transmission Electron Microscopy and X-Ray Diffraction:

Transmission electron microscopy was carried out to investigate the morphology and adsorption of AuNPs on the click-modified GO surface.

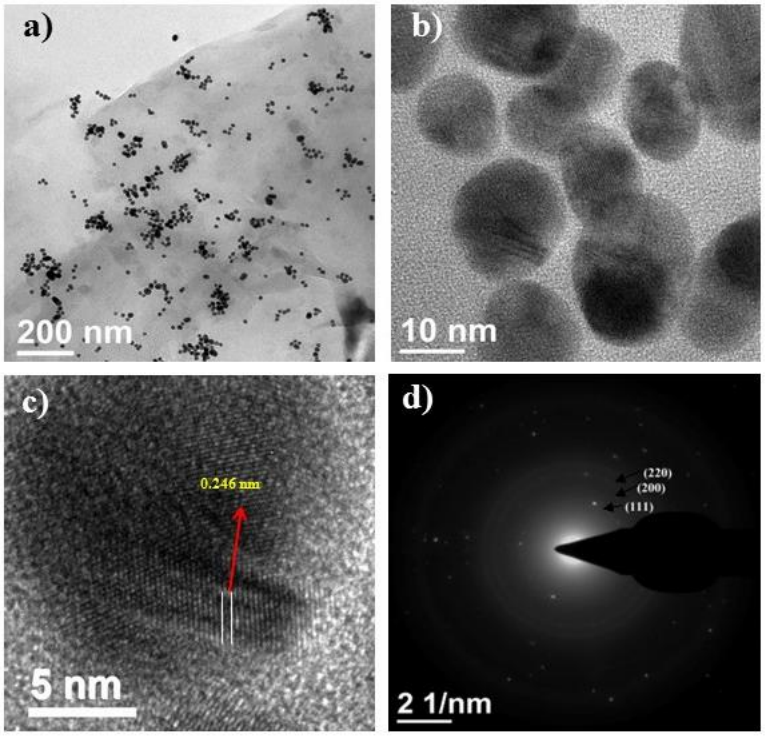

Figure 2.4. (a-c) HRTEM images of rGO(click)/AuNPs. **(d)** Selective area electron diffraction pattern.

Figure 2.4a–d shows the HRTEM images of the as-prepared rGO/Au. AuNPs with an average diameter of 12 nm were observed on the surface of the rGO, which was confirmed from the particle-size distribution calculated from **Figure 2.5a**. A lattice spacing of 0.246 nm was measured, which corresponds to (111) and other planes for face-centred cubic (fcc) Au nanocrystals.

The X-ray diffraction (XRD) is the most widely used technique for structural characterization. The XRD pattern for the GO, rGO and rGO with AuNPs is shown in **Figure 2.5b**. The peaks at 9.98 (001) and 24.5 (002) are the characteristic of GO and rGO, respectively. The diffraction peak at 2θ ~10 is mainly due to the oxidative exfoliation of graphite. While reduced graphene oxide diffraction peak at 2θ ~ 25 corresponding to the highly organized layer structure with decreased interlayer distance along the (002) orientation. The other peaks such as 38 (111), 44.3 (200) and 64.4 (220) in the XRD and selected-area electron diffraction (SAED) patterns also reveal the face centred cubic (JCPDS no. 04-0784) structure of the AuNPs.

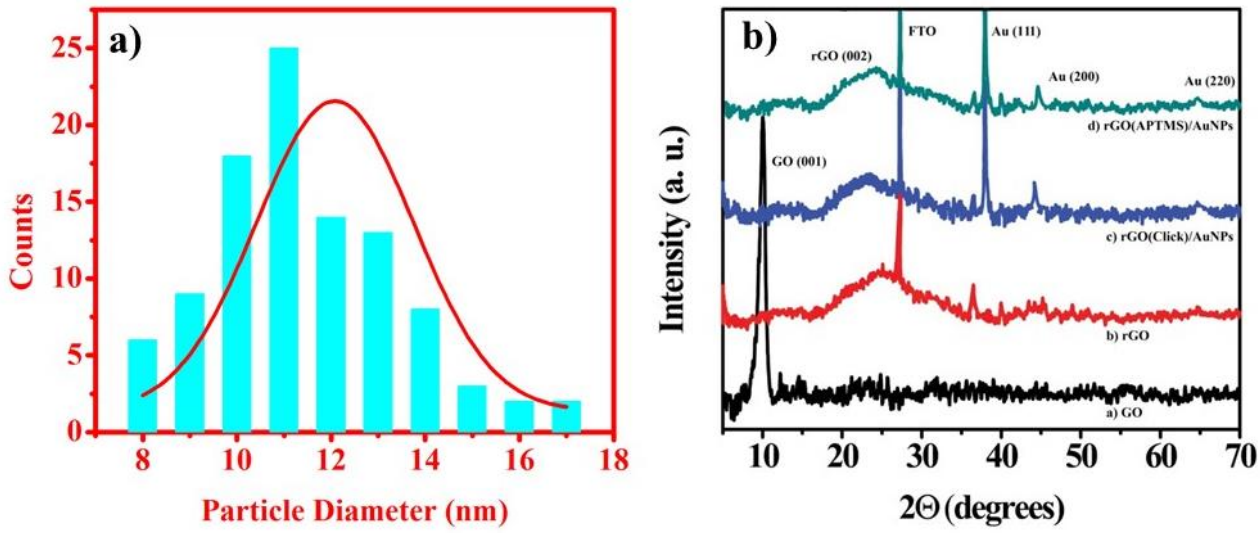

Figure 2.5. (a) Gold nanoparticles size distribution **(b)** XRD pattern for the as synthesized GO, rGO and functionalized rGO with gold nanoparticles.

2.4.4 X-ray Photoelectron Spectroscopy:

In XPS survey, GO samples showed that considerable oxygen moieties are present in the carbon backbone of the GO as in **Figure 2.6a**. The carbon 1s shows four peaks at 284.5, 286.4, 287.5 and 288.5 eV that correspond to C=C, C-O, C=O, and O=C-O, respectively.[24] **Figure 2.6b** indicates lowering in the oxygenated carbon intensity of the GO surface confirming the reduction of GO into rGO. Also, the carbon peak shows considerable increase in the intensity of the C=C bond, which suggests the restoration of the hexagonal network of graphene owing to the reduction of GO to rGO.

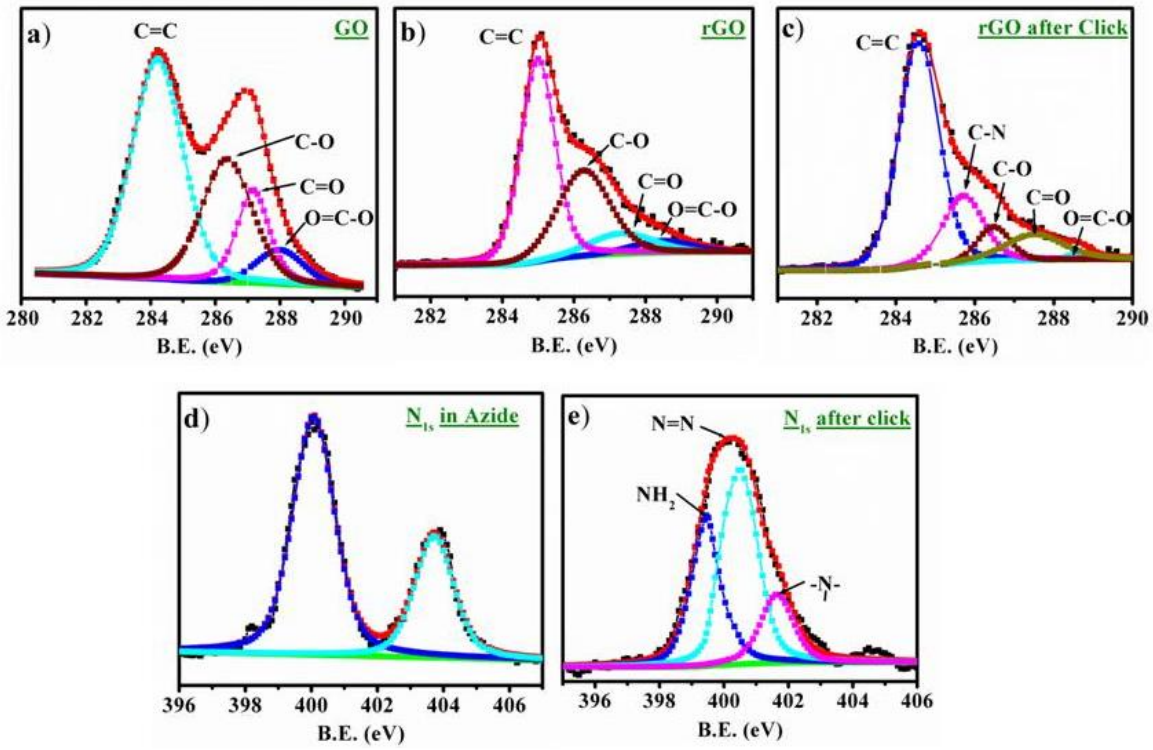

Figure 2.6. XPS spectra of C and N before and after click functionalization of rGO: C1s peak in **(a)** GO, **(b)** rGO, **(c)** azide-modified rGO, and N1s peak in **(d)** azide and **e)** after click reaction.

After click modification we can see the peak at 285.7 eV representing the C-N bond **(Figure 2.6c)** from the successful integration of amine moieties on the rGO surface. **Figure 2.6d** reveals the

presence of a nitrogen peak in the form of azide, which can be deconvoluted into two nitrogen (ratio of 2:1) peaks at 400 and 403.7 eV, thereby confirming the successful azide functionalization of the rGO surface. However, Figure 6e represents the XPS data obtained for the same surface after the click reaction whereby the absence of an azide peak at 403 eV along with the broadening of the N peak at 399.5 eV in the XPS spectra confirms the formation of triazoles. The high-resolution scan of this broad peak shows the presence of three N atoms in different environments, namely, NH_2 at 399.5 eV, N=N of the triazoles at 400.5 eV and NH_4^+ at 401.7 eV. [29]

2.4.5 Electrochemical Experiments:

2.4.5 (a) Cyclic Voltammetry:

Electrochemical measurements were carried out to comprehend the electrochemical reaction occurring on the different electrode interfaces.

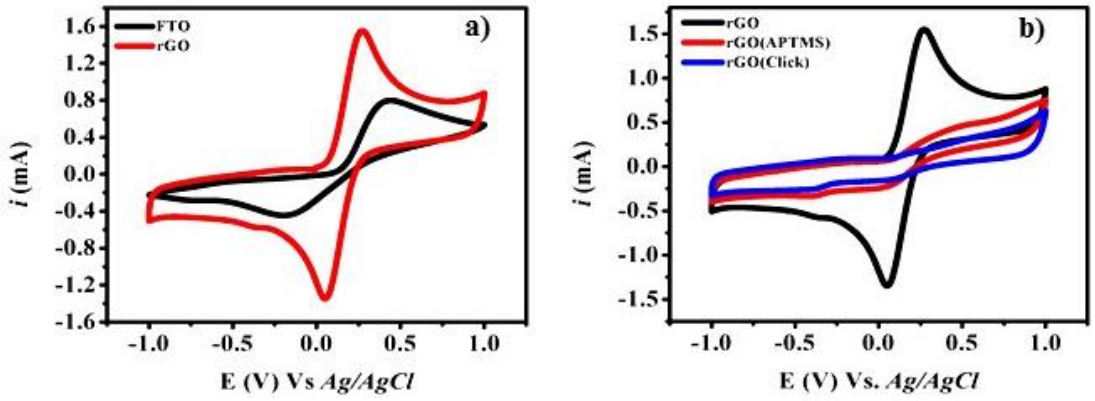

Figure 2.7. (a) Cyclic voltammograms of rGO and **(b)** functionalized rGO in 10 mM of potassium ferrocyanide and 0.1 M KCl versus Ag/AgCl.

The cyclic voltammograms of various electrodes are studied by using 10 mM potassium ferrocyanide (as a fast electron-transfer probe) in 0.1 M KCl as a supporting electrolyte at a scan rate of 100 mV/s.

Figure 2.7a represents the very well behaved cathodic (i_{pc}) and anodic (i_{pa}) characteristic peaks for the [Fe $(CN)_6^{3-/4-}$] redox system on the bare FTO and FTO/rGO electrode which are well defined and sharp. The shift in the peak values suggests that the reaction kinetics on the different electrodes are different. For rGO the peak potential shift is 0.214 V suggesting that the rGO is a highly conducting layer owing to high-quality sp^2 network and high surface area. The redox peaks on rGO are due to the defects related to some oxygen functionalities and defects still present on its edges and surface which can act as a redox centre. However, after functionalization the redox couple's peaks disappear indicating electron blocking behaviour self-assembled monolayers as in **Figure 2.7B**.

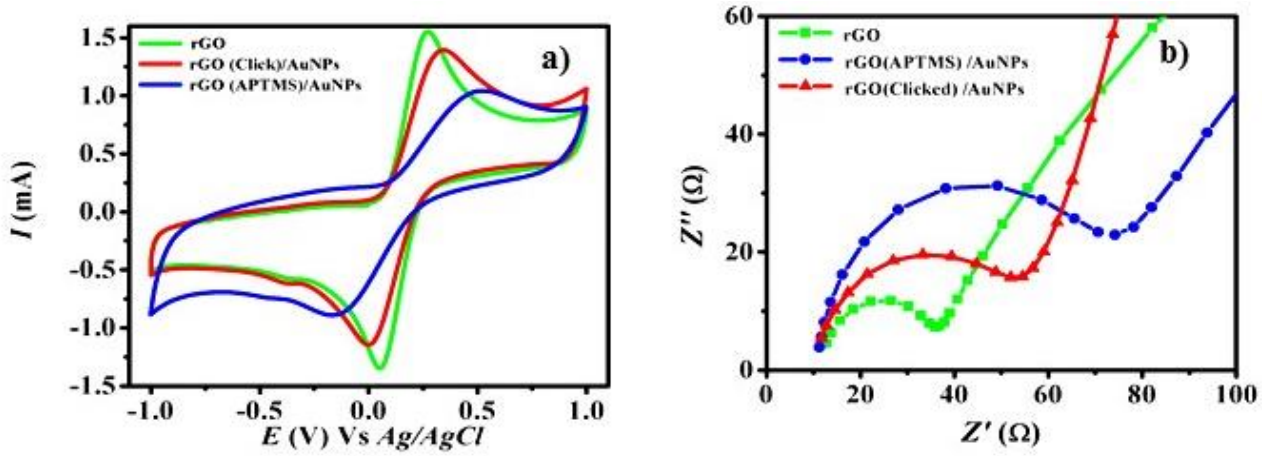

Figure 2.8. (a) CV and **(b)** EIS measurements of rGO and functionalised rGO after AuNPs attachment in 10 mm of potassium ferrocyanide and 0.1 M KCl versus Ag/AgCl (EIS frequency range: 10 kHz–0.1 Hz).

After gold nanoparticles assembly the redox peaks again appear suggesting that the AuNPs are serving as redox centre. In figure 8a for the rGO(APTMS)/AuNPs electrode, the cathodic and anodic peaks are found at 0.494 and at -0.138 V, whereas for the rGO-(click)/AuNPs electrode, they are at 0.320 and 0.003 V, respectively. The peak potential separations (Δ Ep) for [Fe $(CN)_6^{3-/4-}$] are found to be 0.632 and 0.323 V, corresponding to rGO(APTMS)/AuNPs and rGO(click)/AuNPs. This indicates facile heterogeneous electron-transfer kinetics of the redox couple at rGO and AuNPs

deposited on the rGO surface. It becomes sluggish for the rGO(APTMS)/AuNPs electrode relative to rGO- (Click)/AuNPs. The nature of the linkers between the AuNPs and rGO affects the interfacial electronic structure and charge-transfer rate. The lower Δ Ep value for clicked rGO might be attributed to the low barrier offered by the triazole ring conjugated with rGO, whereas aminosilane offers greater resistance to the electron transfer, which hinders the electron transport.

2.4.5 (b) Impedance:

Figure 2.8b shows the electrochemical impedance characteristics of AuNPs attached on functionalized rGO. It illustrates the resistance offered by the interface of different electrodes. The impedance generally has two processes: 1) charge-transfer resistance-limiting process also called as faradic reaction where small semicircle at higher frequencies appears and 2) the diffusion process corresponding to ion transfer at the electrodes represented by a straight line at lower frequencies. The plot shows simultaneous appearance of these processes for the electrodes. The FTO/rGO electrode has a low charge-transfer resistance value (≈ 27 Ω) because of the direct interaction of redox species with the rGO conducting surface. However, functionalised rGO electrodes shows slight increase in the Rct values after gold nanoparticles were assembled on it. The AuNPs on click-modified surface offer less resistance to the charge transfer (R_{ct} ≈ 52 Ω) than the APTMS-modified surface (Rct ≈ 76 Ω), which can be attributed to the aromatic triazole ring assisting or providing the necessary conducting link for the electron transfer onto the electrode surface.

2.4.6 Photoelectrochemical Experiments:

The gold nanoparticles immobilized on the chemically modified rGO surface were studied for photocurrent generation. **Figure 2.9a**, represents the linear sweep voltammograms for rGO (a),

AuNPs on APTMS (b) and click functionalized rGO (c) respectively in the presence of white light. It indicates higher photocurrent generation for AuNPs attached on click modified rGO electrode.

The transient photocurrent versus time was recorded at 0 V against the open circuit potential (E_{ocp}) in which Ag/AgCl and Platinum foil served as a reference electrode and as a counter electrode, respectively. The photocurrent responses were measured for rGO, rGO(APTMS)/AuNPs and rGO(click)/AuNPs electrodes irradiated with white light in the visible range (λ >400 nm,100 mW/cm^2) are plotted in **Figure 2.9b**. On/off cycle photocurrent was prompt and became stable in the time interval of the pulse illumination.

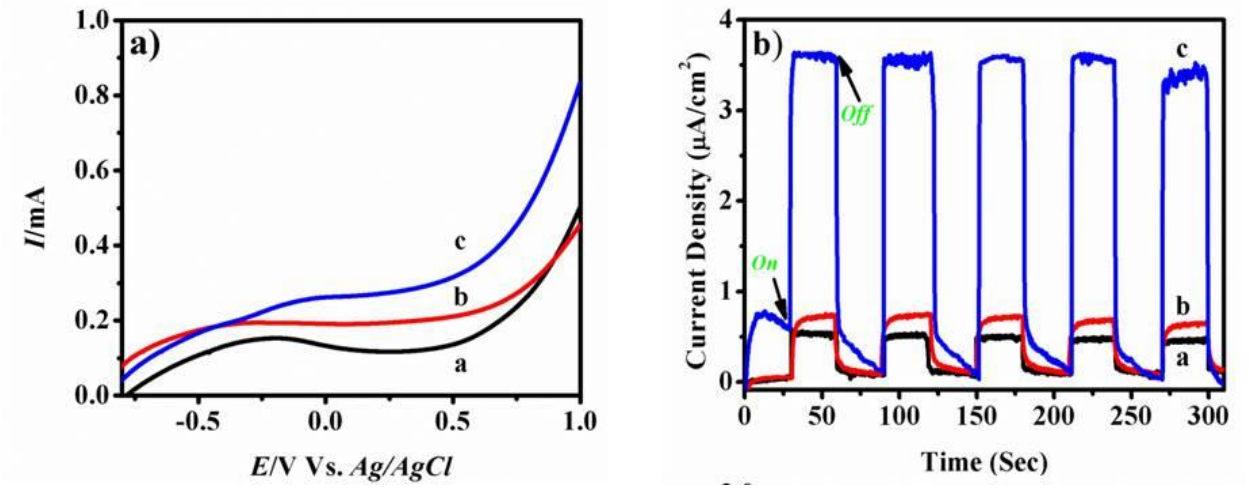

Figure 2.9. (a) Linear sweep voltammograms. **(b)** Transient photocurrent responses of a) FTO/rGO, b) FTO/rGO(APTMS)/AuNPs and**(c)** FTO/rGO(click)/ AuNPs electrodes using 1 M Na_2SO_4 as an electrolyte (at 0 V bias versus Eocv) under white light irradiation.

When irradiated with white light, a cathodic photoresponse was shown by rGO electrodes with photocurrent ~ 0.54 μA/cm^2. The click-modified rGO exhibited a cathodic photocurrent of five orders of magnitude higher (3.62 μA/cm^2) than APTMS/rGO (0.70 μA/cm^2).

To ascertain the plasmonic effect in photocurrent generation, the click-modified samples were irradiated with light of specific wavelengths. **Figure 2.10** reveals the wavelength dependent photocurrent measurements for the AuNPs on click functionalized rGO electrodes. On light irradiation with 530 nm, it showed the highest photocurrent (2.36 μA/cm^2) relative to the other wavelengths. The wavelength of incident light is close to the surface plasmon band of the gold nanoparticles i.e. λ ~ 543 nm; indicating the photocurrent from the AuNPs. This can be attributed to the SPs generated on the AuNPs by light irradiation; which induces a dipole that enhances the electric field, thus leading to separation and generation of hot electrons.

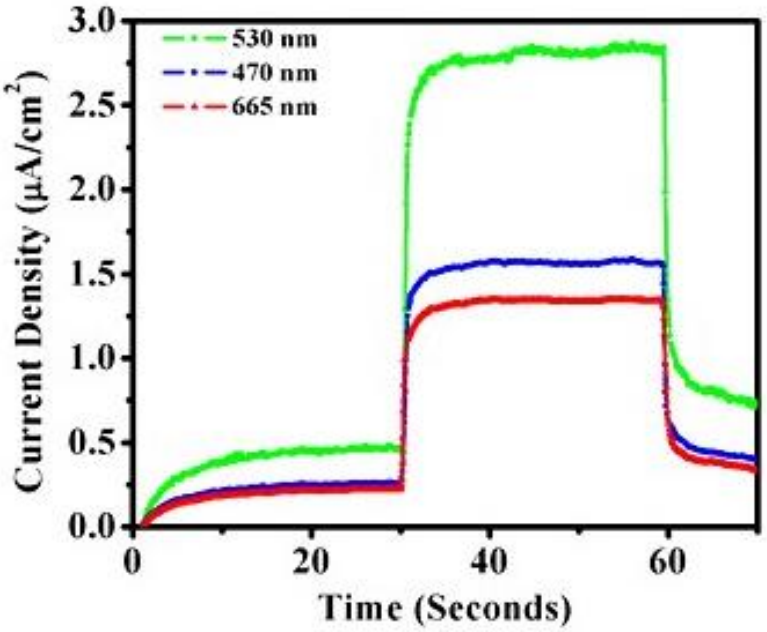

Figure 2.10. Wavelength dependent photocurrent responses of FTO/rGO(click)/AuNPs electrodes in 1 M Na_2SO_4 as an electrolyte and applying 0 V bias.

These hot electrons then effectively transferred to the graphene electrode with the help of triazole ring enabling higher photocurrent. It shows that the conjugated triazole moiety can serve as a better linker than the unconjugated one, thereby facilitating charge transfer from AuNPs to graphene. It also

reveals the better electronic conductivity of rGO for inter- facial shuttling of electrons from the AuNPs to the rGO surface through the aromatic triazole linker. It is worth mentioning that the presence of bifunctional linkers between semiconductor and AuNPs could affect the electronic structure at the interface as well as the electron-transfer rate.[55-57] In such a system, the photoexcited electron can relax by any one of the two mechanisms, namely, tunnelling or resonant charge-transfer mechanisms. We believe that resonant charge transfer is probably the more suitable mechanism in our case. The result shows that the selective π-conjugated covalent attachments on the rGO remarkably enhance the photoelectrical transport properties of the rGO.

2.5 Conclusion:

Enhanced photocurrent generation was observed from the functionalized rGO electrodes when assembled with AuNPs on different linker molecules due to plasmonic assistance. The AuNPs on click-functionalized rGO shows enhanced photocurrent whereby AuNPs act as a plasmonic antenna and triazoles act as an effective electron-transferring linker. The structure of self-assembled monolayers influences the electron-transport properties in the hybrid. The aromatic triazoles show the faster electron transfer than linear one. Cyclic voltammetry and electron impedance spectroscopy (EIS) measurement of the electrode interface also suggest that the π-conjugated triazole ring to be an excellent bridge for the fast charge transport from the AuNPs to the graphene surface. The inclusion of π- conjugation near metal nanoparticles allows electron delocalization over the aromatic ring. This increases the scattering cross section due to intense electromagnetic field resulting into Raman intensity enhancement in the rGO bands. It also acts as an efficient pathway for the relaxation of hot electrons, thereby ensuring a large photocurrent from the hybrid.

2.6 References:

1] A. H. Castro Neto, F. Guinea, N. M. R. Peres, K. S. Novoselov and A. K. Geim, *Rev. Mod. Phys*. **2009**, 81, 109.

2] A. K. Geim and K. S. Novoselov, *Nat. Mater*. **2007**, 6, 183.

3] K. S. Novoselov, A. K. Geim, S. V. Morozov, D. Jiang, Y. Zhang, S. V. Dubonos, I. V. Grigorieva and A. A. Firsov, *Science*, **2004**, 306, 666.

4] S. M. Paek, E. J. Yoo and I. Honma, *Nano Lett*. **2009**, 9, 72.

5] L. Ji, M. Rao, H. Zheng, L. Zhang, Y. C. Li, W. H. Duan, J. H. Guo, E. J. Cairns and Y. G. Zhang, *J. Am. Chem. Soc*. **2011**, 133, 18522.

6] X. L. Li, G. Y. Zhang, X. D. Bai, X. M. Sun, X. R. Wang, E. G. Wang and H. J. Dai, *Nat. Nanotechnol*. **2008**, 3, 538.

7] J. Chen, M. Ishigami, C. Jang, D. R. Hines, M. S. Fuhrer and E. D. Williams, *Adv. Mater*. **2007**, 19, 3623.

8] D. H. Wang, R. Kou, D. W. Choi, Z. G. Yang, Z. M. Nie, J. Li, L. V. Saraf, J. G. Zhang, G. L. Graff, J. Liu, M. A. Pope and I. A. Aksay, *ACS Nano*, **2010**, 4, 1587.

9] D. H. Wang, D. W. Choi, J. Li, Z. G. Yang, Z. M. Nie, R. Kou, D. H. Hu, C. M. Wang, L. V. Saraf, J. G. Zhang, I. A. Aksay and J. Liu, *ACS Nano*, **2009**, 3, 907.

10] F. Schedin, A. K. Geim, S. V. Morozov, E. W. Hill, P. Blake, M. I. Katsnelson and K. S. Novoselov, *Nat. Mater*. **2007**, 6, 652.

11] X. Li, X. Wang, L. Zhang, S. Lee and H. Dai, *Science* **2008**, 319, 1229.

12] Y. Wang, Z. Li, D. Hu, C. Lin, J. Li and Y. Lin, *J. Am. Chem. Soc.* **2010**, 132, 9274.

13] D. Dreyer, S. Park, W. Bielawski and S. Ruoff,*Chem. Soc. Rev.* **2010**, 39, 228.

14] X. Zhou, X. Huang, X. Qi, S. Wu, C. Xue, F. Boey, Q. Yan, P. Chen and H. Zhang, *J. Phys. Chem. C*, **2009**, 113, 10842.

15] B. Lee, Y. Chen, F. Duerr, D. Mastrogiovanni, E. Garfunkel, E. Andrei and V. Podzorov, *Nano Lett.* **2010**, 10, 2427.

16] B. Li, A. Klekachev, M. Cantoro, C. Huyghebaert, A. Stesmans, I. Asselberghs, S. De Gendt and S. Feyter, *Nanoscale*, **2013**, 5, 9640.

17] J. Lee, S. Kang, J. Jaworski, K. Kwon, M. Seo, J. Lee and J. Jung, *Chem. Eur. J.* **2012**, 18, 765.

18] Y. Xu, Z. Liu, X. Zhang, Y. Wang, J. Tian, Y. Huang, Y. Ma, X. Zhang and Y. Chen, *Adv. Mater.* **2009**, 21, 275.

19] R. Cohen, K. Stokbro, J. Martin and M. Ratner, *J. Phys. Chem. C*, **2007**, 111, 14893.

20] B. Albinsson, M. Eng, K. Pettersson and M. Winters, *Phys. Chem. Chem. Phys*. **2007**, 9, 5847.

21] A. Nitzan and M. A. Ratner, *Science*, **2003**, 300, 1384.

22] G. de Miguel, M. Wielopolski, D. Schuster, M. Fazio, O. Lee, C. Haley, A. Ortiz, L. Echegoyen, T. Clark and D. Guldi, *J. Am. Chem. Soc*. **2011**, 133, 13036.

23] A. Baron, C. Herrero, A. Quaranta, M. Charlot, W. Leibl, B. Vauzeilles and A. Aukauloo, *Chem. Commun*. **2011**, 47, 11011.

24] P. Zoon, I. Van Stokkum, M. Parent, O. Mongin, M. Blanchard Desce and A. Brouwer, *Phys. Chem. Chem. Phys*. **2010**, 12, 2706.

25] H. Kolb, M. Finn and K. Sharpless,*Angew. Chem. Int. Ed.* **2001**, 40, 2004.

26] C. BarnerKowollik, F. Du Prez, P. Espeel, C. Hawker, T. Junkers, H. Schlaad and W. Van Camp, *Angew. Chem. Int. Ed*. **2011**, 50, 60.

27] J. Lutz, *Angew. Chem. Int. Ed*. **2007**, 46, 1018.

28] X. Liu, H. Zheng, Y. Maa, Q. Yan and S. Xiao, *J. Colloid Interface Sci.* **2011**, 358, 116.

29] N. Lia and W. Binder, *J. Mater. Chem*. **2011**, 21, 16717.

30] A. Devadoss and C. Chidsey, *J. Am. Chem. Soc*. **2001**, 129, 5370.

31] I. Kaminska, M. Das, Y. Coffinier, J. NiedziolkaJonsson, J. Sobczak, P. Woisel, J. Lyskawa, M. Opallo, R. Boukherroub and S. Szunerits, *ACS Appl. Mater. Interfaces,* **2012**, 4, 1016.

32] M. Kauranen and A. Zayats, *Nat. Photonics*, **2012**, 6, 737.

33] D. Gramotnev and S. Bozhevolnyi, *Nat. Photonics*, **2010**, 4, 83.

34] J. Zhang and C. Noguez, *Plasmonics,* **2008**, 3, 127.

35] J. Anker, W. Hall, O. Lyandres, N.Shah, J. Zhao and R. Duyne, *Nat. Mater*. **2008**, 7, 442.

36] A. Brolo, *Nat. Photonics,* **2012**, 6, 709.

37] A. McFarland, R. Van Duyne, *Nano Lett*. **2003**, 3, 1057.

38] S. Linic, P. Christopher and D. Ingram, *Nat. Mater*. **2011**, 10, 911.

39] I. Thomann, B. Pinaud, Z. Chen, B. Clemens, T. Jaramillo and M. Brongersma, *Nano Lett*. **2011**, 11, 3440.

40] W. Hou and S. B. Cronin, *Adv. Funct. Mater*. **2013**, 23, 1612.

41] M. Son, J. Im, K. Wang, S. Oh, Y. Kim and K. Yoo, *Appl. Phys. Lett*. **2010**, 96, 023115.

42] Y. Tian and T. Tatsuma, *J. Am. Chem. Soc*. **2005**, 127, 7632.

43] K. Saravanan, B. Panigrahi, R. Krishnan and K. Nair, *J. Appl. Phys*. **2013**, 113, 033512.

44] B. Lawrie, Jr. R. Haglund and R. Mu, *Opt. Express,* **2009**, 17, 2565.

45] H. Chen, C. Chen, M. Tseng, P. Wu, C. Chang, L. Cheng, H. Huang, T. Chan, D. Huang, R. Liu and D. Tsai, *Small* **2013**, 9, 1.

46] S. Standridge, G. Schatz and J. Hupp, *J. Am. Chem. Soc*. **2009**, 131, 8407.

47] S. Lin, K. Lee, J. Wu and J. Wu, *Appl. Phys. Lett*. **2011**, 99, 043306.

48] K. Sugawa, T. Akiyama, H. Kawazumi and S. Yamada, *Langmuir*, **2009**, 25, 3887.

49] K. Sugawa, S. Hirono, T. Akiyama and S. Yamada, *Photochem. Photobiol. Sci.* **2012**, 11, 318.

50] P. Cui, S. Seo, J. Lee, L. Wang, E. Lee, M. Min and H. Lee, *ACS Nano*, **2011**, 5, 6826.

51] D. Marcano, D. Kosynkin, J. Berlin, A. Sinitskii, Z. Sun, A. Slesarev, L. Alemany, W. Lu and J. Tour, *ACS Nano*, **2010**, 4, 4806.

52] L. Guardia, S. Rodil, J. Paredes, R. Rozada, A. Alonso, J. Tascó, *Carbon*, **2012**, 50 (3), 1014.

52] R. Gengler, D. Badali1, D. Zhang1, K. Dimos, K. Spyrou, D. Gournis and R. Dwayne Miller, *Nat. Comm.* **2013**, 4, 1-5.

53] Y. Cao, J. Feng and P. Wu, *J. Mater. Chem*. **2012**, 22, 14997.

54] a) S. Some, Y. Kim, Y. Yoon, H. J. Yoo, S. Lee, Y. Park and H. Lee, *Sci. Rep*. **2013**, 3, 1; b) M. Cheng, R. Yang, L. Zhang, Z. Shi, W. Yang, D. Wang, G. Xie, D. Shi and G. Zhang, *Carbon* **2012**, 50, 2581.

55] W. Park and Z. Kim, *Nano Lett*. **2010**, 10, 4040.

56] C. Zhang, R. Hao, H. Liao and Y. Hou, *Nano Energy*, **2013**, 2, 88.

57] a) T. Z. Markus, M. Wu, L. Wang, D. H. Waldeck, D. Oron and R. Naaman, *J. Phys. Chem. C*, **2009**, 113, 14200; b) C. Ratanatawanate, Y. Tao, J. Kenneth and J. Balkus, *J. Phys. Chem. C*, **2009**, 113, 10755; c) M. Miljevic, B. Geiseler, T. Bergfeldt, P. Bockstaller and L. Fruk, *Adv. Funct. Mater*. **2014**, 24, 90.

Enhanced Photoluminescence and Photoactivity of Plasmon Sensitized nSiNWs/TiO_2 Heterostructures

A radial heterojunction between TiO_2 deposited on nSiNWs surface were fabricated by dip coating and thermal annealing of the samples. Sensitization by gold nanoparticles on the heterojunction was achieved by soaking and subsequent heating. The AuNPs thus formed influence the optical and photocurrent properties of the heterojunction considerably. Improvement in the band gap emission of TiO_2 has been found at the expense of defect radiation. Excitation of AuNPs deposited on nSiNWs/TiO_2 by light irradiation shows a wavelength-dependent photocurrent due to the increased photoactivity of the heterojunction.

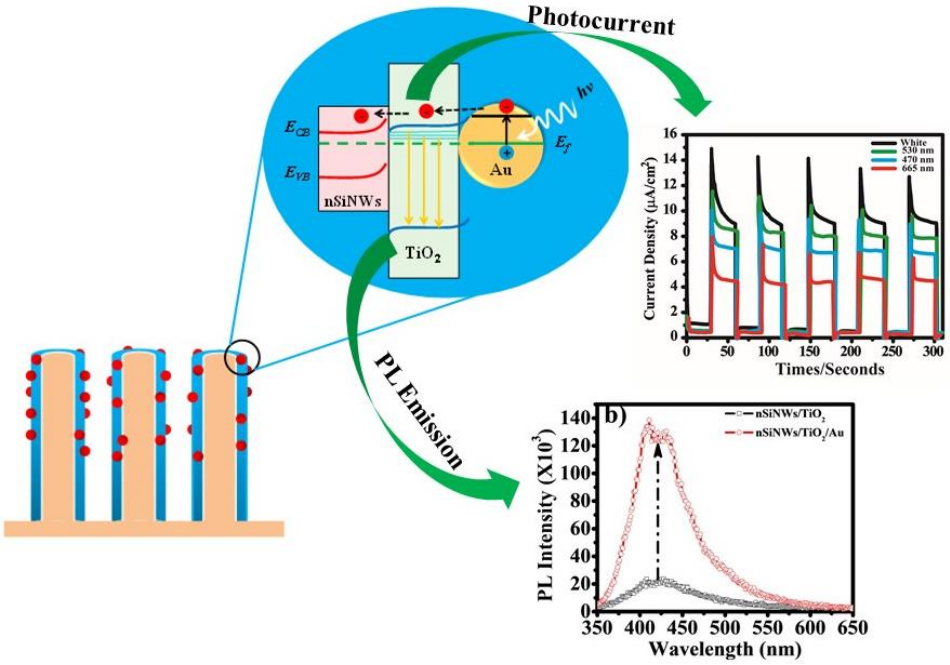

Schematic illustrations of the heterojunction optical properties and photocurrent results.

3.1 Introduction:

Metal nanoparticles exhibit localized surface plasmon resonance (LSPR) by the interaction of visible-light photons with the valence electrons on the metal surface. At a resonance frequency of metal nanoparticles the strongest optical interaction occurs being a function of the size, shape, type of metals as well as the local dielectric environment.[1,2] The large resonant scattering cross sections of metal nanostructures offer the potential to scatter light strongly, while LSPs can guide and confine light flux in nanoscale dimensions.[3] The LSPs decay radiatively by scattering or non-radiatively resulting in energy absorption.[4] These tunable properties of metal nanoparticles can be used in a variety of applications from non-linear optics and photovoltaics to sensing.[5,7] Light detection and photocurrent generation from the excitation of surface plasmon on the surface of metal nanoparticles is a recent concept. There has been a profound surge of interest in exploiting the collective oscillations of the conduction electrons of a metal as a powerful method for use in nanoscience and nanotechnology.

One-dimensional SiNWs arrays offer increased surface area, enhanced light absorption and reduced charge recombination. Due to their versatile properties and easy, controllable synthesis, silicon nanowires (SiNWs) are important candidates for optoelectronic devices and solar cells.[8,9] Large-scale silicon nanowire (SiNWs) arrays fabricated by metal assisted chemical etching have been used as the antireflection layer for photovoltaic cells and for other optoelectronic devices [10-14]. This method is very cheap and simple, suitable for high-throughput and inexpensive industrial production. Oxides with wide band gaps and high dielectric constants, commonly known as k-oxides, are of great interest in the electronic industry. TiO_2 is a remarkable semiconductor material

with a large band gap (3.0–3.2 eV), is chemically inert, has a high photo-conversion efficiency and good photo-stability.[15,16] Although Si is more efficient, it corrodes in water, and the large band gap of TiO_2 restricts its applications in certain requirements, e.g. water splitting in the visible part of the spectrum. Semiconductor heterojunctions are being studied to overcome these shortcomings. The performance of functional devices in water splitting applications is based on the heterojunctions formed between TiO_2 and silicon. Such heterojunctions allow effective separation and utilization of charge carriers (e^-/h^+) by increased absorption of light. Band bending near the junction of nSiNWs/TiO_2 for photo-oxidative properties of the hybrid in photoelectrochemical cells has been studied, where it has been observed that the photocurrent increases due to enhanced charge separation and minimum recombination.[17] Photocatalytic degradation of phenol on an electrode with n–n and p–n heterojunctions has been observed between SiNWs and TiO_2.[18] Semiconductor–metal composites are highly valued for their visible light sensitivity because of the plasmonic antenna effect of metal nanoparticles extending the absorption range of wide band gap semiconductors. Such hybrid nanomaterials show enhanced physical properties such as low reflection, high absorption, dielectric strength etc.

In this chapter, we demonstrate the effect of the surface plasmon of gold nanoparticles on SiNWs/TiO_2 heterojunctions. These hybrids show enhanced optical absorption, emission and photocurrent generation. Plasmonic sensitization enhances self-trapped exciton emission and oxygen vacancy radiative recombination emission properties of TiO_2. Light-emitting diodes (LEDs) are used as the source of light for photocurrent measurements. Enhanced photocurrent is achieved by decorating AuNPs on the surface of nSiNWs/TiO_2 heterojunctions due to plasmonic charge carrier generation.

3.2 Experimental Methods:

3.2.1 Synthesis of TiO_2 sol.:

Titanium isopropoxide (TTIP) is used as a precursor for the synthesis of the titanium sol. In the preparation, 0.5 ml of TTIP was added into 5 ml of ethanol with simultaneous addition of 0.2 ml of acetic acid. Double distilled water (0.5 ml) is added dropwise in the above solution alongwith sonication for the hydrolysis of titanium isopropoxide. A white turbidity appears indicating the formation of TiO_2 which was dissolved by adding some amount of dilute HNO_3. The clear solution thus formed is the sol of titanium. As prepared titanium sol is stable for many days, subsequently used for the TiO_2 coating on n-SiNWs.

3.2.2 Synthesis of n-SiNWs/TiO_2:

Electroless metal deposition method is used to synthesize SiNWs. The Silicon wafers cut into small pieces and clean with acetone, isopropyl alcohol finally with DI-water by sonication. The cleaned wafers were blow dried under N_2 gas. The wafers then treated with piranha solution for 30 minutes (H_2SO_4:H_2O_2, 3:1) to oxidize any organic contaminants and simultaneously creating hydroxylated surface on the Silicon. The etching of silicon is carried out using 0.04 M $AgNO_3$ and 5% HF (1:1) for 5 minutes at 55°C. After etching, SiNWs were kept in 5 M HNO_3 to remove deposited silver. For TiO_2 thin film coating, native oxide layer was removed from the surface of the SiNWs by keeping it in 5% HF solution for 5 min. H-terminated SiNWs array was deep coated for 10 times in TiO_2 sol to form TiO_2 coating on SiNWs. After, complete drying the substrate was annealed at 500°C for 1 hr. under ambient oxygen to form TiO_2 covered n-SiNWs.

3.2.3 Gold deposition on n-SiNWs/TiO_2:

For gold deposition the TiO_2 coated samples were soaked in gold salt solution (1mM $HAuCl_4$) for 30 minutes and dried under IR lamp. These samples were then annealed at 400°C (10 minutes) for the gold nanoparticle formation.

3.3 Characterization:

3.3.1 Morphology:

Morphological characteristics of the as synthesized materials was examined by using Quanta 200 3D, FEI scanning electron microscope (SEM). High resolution transmission electron microscope (HR-TEM) images were taken by using FEI Technai 300 keV. X-Ray diffraction studies were carried out on a Phillips PW 1830 instrument operating at 40 kV and a current of 30 mA with Cu Kα radiation. UV–Visible diffused reflectance spectra were recorded using a Jasco V-570 spectrophotometer. The Raman spectra were collected using LabRAM HR800 (Jobin Yvon Horiba, France) with laser wavelength of 632.84 nm (He-Ne Laser, 20 mW of power) and 2 μm spot size. PL data were recorded on Fluorolog Horiba Jobin Yvon fluorescence spectrophotometer using a xenon lamp with an excitation wavelength of 340 nm. Electrochemical measurements along with photocurrent measurements were performed on Potentiostat (Biologic SP 300, Netherlands).

3.3.2 Photo-Electrochemical (PEC) Measurements:

PEC study was carried out in neutral 1 M Na_2SO_4 using three electrode system where Ag/AgCl and Pt foil served as reference and counter electrodes. All samples were covered with Teflon tape exposing the front side (0.5 cm x 0.5 cm) of the electrode. Contacts were made using Ga-In

conducting liquid. Visible light measurements were carried out by irradiating the exposed part of the samples with white and monochromatic LED sources (Luxeon Star, Canada). The photocurrents for each sample were then normalized with respect to per unit area and plotted.

3.4 Result and Discussion:

3.4.1 SEM and TEM:

The heterojunction materials fabricated by the above process were characterized by scanning electron microscopy.

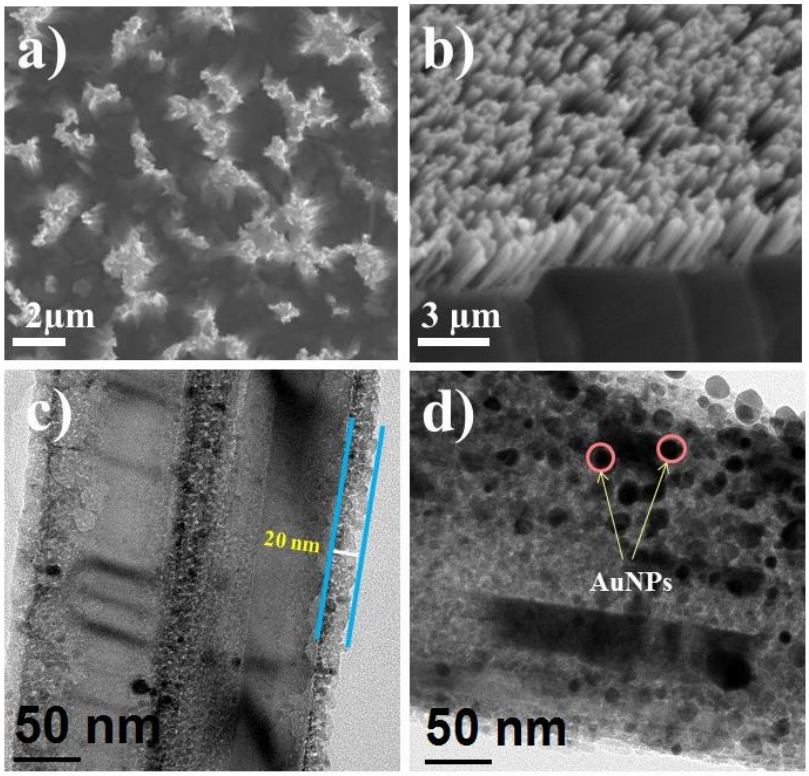

Figure 3.1. a) Top view and **b)** cross section (tilt at 45°) SEM views of the as-prepared nSiNWs/TiO_2 heterojunction. **c, d)** HRTEM images of the TiO_2-coated nSiNWs before and after gold nanoparticle deposition, respectively.

Vertical SiNWs of approximately 3 μm in length and 100 nm in diameter was observed on the silicon surface which are shown in **Figure 3.1a and b**. Individual Si nanowires are uniformly covered by the TiO_2 layer as can be seen in **Figure 3.1b**.

High resolution TEM of the SiNWs/TiO_2 sample, shown in the **Figure 3.1c,** reveals the thickness of the TiO_2 layer of approximately 20 nm. These samples were soaked in a gold salt solution where Au (III) ions physically adsorbed on the TiO_2 surface. After thermal annealing the nanoparticles are found to be partially embedded in the TiO_2 matrix. The **Figure 3.1d** shows ~9 nm sized gold nanoparticles on TiO_2 surface, suggesting the effectiveness of the process utilized herein for the synthesis of the hybrids. The relative size distribution of gold nanoparticles was calculated after measuring several particles from the **Figure 3.2**.

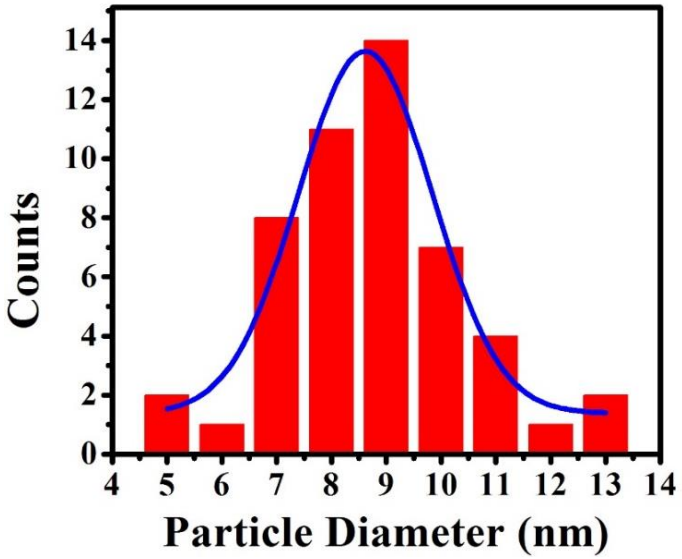

Figure 3.2. Particle size distribution of gold nanoparticles on the heterojunction.

3.4.2 XRD and Diffuse Reflectance spectroscopy:

XRD patterns of the samples were plotted in the **Figure 3.3a** shows the peaks at 2θ = 32.2 (100) and 69.3 (400) correspond to the highly crystalline nature of SiNWs. The peaks appearing at 25.4 (101), and 75.3 (215) belong to the crystalline anatase phase of the TiO_2 [JCPDS No. 841285]. After gold nanoparticles deposition new peaks appears at 38.2 and 44.4 representing (100) and (200) planes of face-centred cubic symmetry of the gold nanoparticles [JCPDS No. 040784].

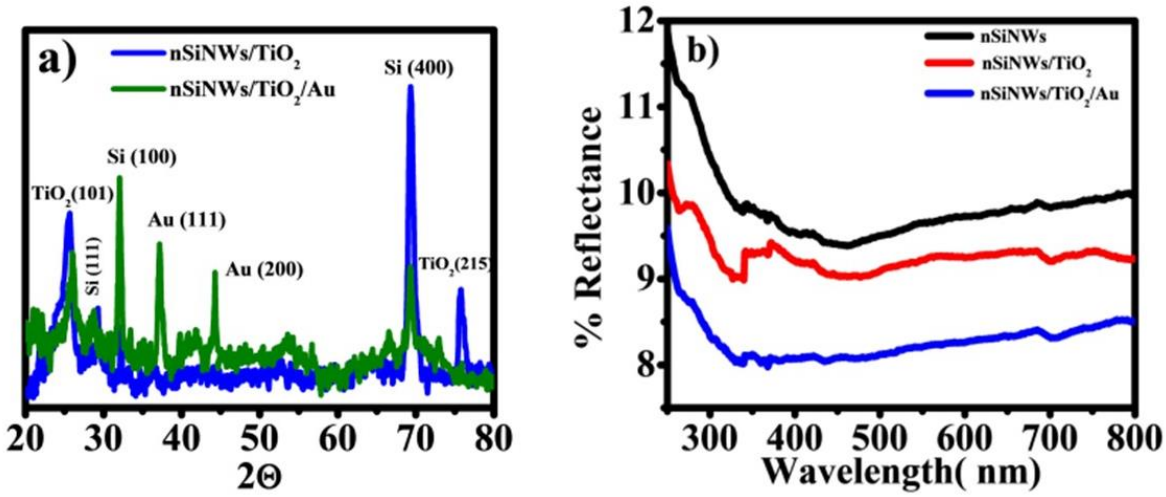

Figure 3.3. a) X-Ray diffraction pattern showing the anatase form of the thin TiO_2 overlayer along with typical gold lattice planes. **b)** Comparative diffuse reflectance spectra of the as-prepared samples.

Diffuse reflectance spectra (**Figure 3.3b**) were recorded for the SiNWs, TiO_2-coated SiNWs and Au nanoparticle decorated SiNWs/TiO_2 samples. All samples show lower reflectance over the spectral range of 300–800 nm than the silicon. SiNWs have inherent lower reflectance due to internal reflection of light. The thin TiO_2 layer on the SiNWs acts as a surface passivating layer as well as an anti-reflection coating, thereby, improving the absorbance by multiple internal reflections. This reveals the increased light harvesting capability of heterojunctions compared to

pristine SiNWs. The heterojunction can utilize light from both the visible and UV regions of the electromagnetic spectrum, which can be utilized in various potential applications. The TiO_2-coated SiNWs samples show ~8% reflectance over the entire visible range after the embedding of gold nanoparticles in the TiO_2 matrix.

Gold nanoparticles have absorption in the range of 450–550 nm due to the surface plasmon. Deposition of AuNPs on the TiO_2 overlayer further enhances light absorption of the heterojunction. The possible reason may be an interaction of LSPRs with the light. This results into higher scattering cross section on gold nanoparticles which increases the scattering of light leading to more photon absorption.[19] Mechanisms such as (i) a change in the refractive index of the metal oxide (here TiO_2) due to the embedded gold nanoparticles or (ii) a change in the effective electron density of the AuNPs could be responsible for the broad nature of the peak.

3.4.3 Raman Spectroscopy and Photoluminescence:

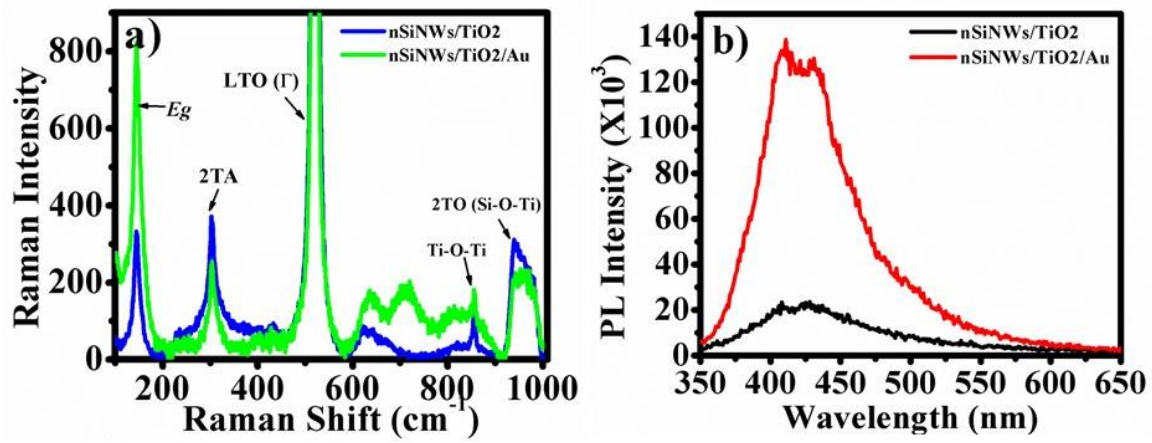

Figure 3.4. a) Micro-Raman spectra before and after deposition of AuNPs on the nSiNWs/TiO_2 heterojunction, indicating the typical anatase peak of TiO_2 and first and second order silicon peaks. **b)** Room temperature photoluminescence spectra of the heterojunctions.

Raman scattering is a sensitive technique to probe crystallinity of the lattice microstructures. **Figure 3.4a** display the Raman spectra of the samples where we can see the typical peaks for the Silicon and TiO_2. The characteristic silicon peak appears at 520.13 cm^{-1}, corresponding to the first order longitudinal and transversal optical phonon (LTO) in the diamond structures of SiNWs. The peak at 303.86 cm^{-1} is the second order transverse acoustic phonon (2TA) contribution, which appears to be significant in the spectra.[21,22] Sharp peaks at 145.60 cm^{-1} and 636.96 cm^{-1} belong to the optical vibration Eg modes in anatase TiO_2.[20]

The broad band centred at 960.1 cm^{-1} is related to second order transversal optical phonons (2TO) in silicon, and also suggests a strong interaction between the TiO_2 thin film and the silicon surface. The peak at 855.8 cm^{-1} could be ascribed to a Ti–O–Ti stretch, indicating 2D connectivity.[23]

Room temperature solid state photoluminescence (PL) spectroscopy was used to understand the presence of defects and the recombination ability of charge carriers. Room temperature photoluminescence spectra have been plotted in **Figure 3.4b**. The as-prepared samples were excited at the band edge absorption of the TiO_2, i.e. 340 nm. Both samples show multi-emission peaks which have been de-convoluted using Gaussian fitting in order to understand their peak positions and nature. For semiconductors such as TiO_2 and ZnO on excitation by photon energy equal to or higher than their band gap, electrons can be transferred from the valence band to the conduction band, generating excitons which after recombining emit radiation approximately equal in energy to the band gap. However, this is not always true, since the presence of defects such as oxygen deficiencies, impurities or metal doping creates sub-energy levels that can capture the electrons, resulting in emission of photons lower in energy than the band gap. The oxygen-related defects in

TiO_2 are intrinsic and particularly important as they give rise to intermediate energy levels within the band gap. As a consequence, many recombination centres are introduced for electron–hole pairs. In the absence of gold nanoparticles, TiO_2 shows PL peaks at 415 nm, 451 nm and 503 nm (**Figure 3.5a**), which belong to self-trapped excitons (STEs), oxygen vacancies with two electrons (F-center or $V_O^{\bullet\bullet}$) and oxygen vacancies with one electron ($V_O^{\bullet}$), respectively. After gold nanoparticle deposition (**Figure 3.5b**), new peaks appeared at 403 nm, 433 nm and 458 nm. All these peaks confirm the anatase-type TiO_2 thin layer formed on the SiNWs.

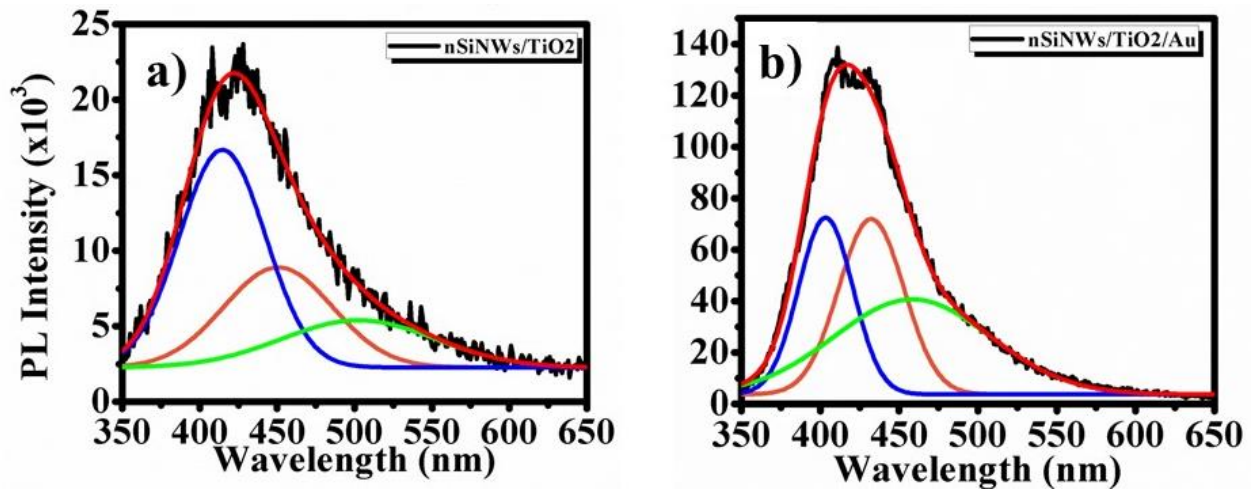

Figure 3.5. a) Gaussian fitted PL peaks of the as-prepared samples before and **b)** after AuNPs deposition respectively.

The PL of anatase TiO_2 has three different physical origins, namely radiative recombination of self-trapped excitons, oxygen vacancies (OVs), and surface states[24] in the defect states within the band gap. It has been reported that oxygen vacancies in metal oxides behave as deep trap states which enhance the recombination of charge carriers, and shallow trap states promote diffusion of carriers to the surface.[25, 26]

The mechanism for the PL in TiO2 can be described by the following processes.[19]

$$TiO_2 \xrightarrow{h\nu} TiO_2(e^- + h^+) \rightarrow e^-_{CB} + h^+_{VB}$$

$$V^{\bullet}_O + e^-_{CB} \rightarrow V_O \text{ (shallow state trapped electrons)}$$

$$V_O + h^+_{VB} \rightarrow V^{\bullet}_O + h\nu \text{ (radiative recombination)}$$

where, V is a Kroger notation for the ionized oxygen vacancy level.

The conduction and valence band edges for titanium oxide lie at ~ 4.26 eV and ~ 7.46 eV with respect to the vacuum, considering the anatase TiO_2 band gap of 3.2 eV.[27] The shallow traps belonging to oxygen vacancies were established to be 0.51 eV[19] and 0.8 eV[28] below the conduction band. The peaks at 451 nm and 503 nm in Fig. 3c are nearly coincident with these OV levels. The electrons excited from the valence band (VB) of the TiO_2 cannot reach the conduction band (CB) of TiO_2; instead they are captured by the oxygen vacancies via a non-radiative process and then recombine with the holes in the VB, accompanying radiative emission in the visible region corresponding to the peak at 415 nm. A blue shift of 12 nm in the band edge luminescence is observed for the gold-deposited samples, suggesting trapping of electrons in the energy level just below the CB of TiO_2. It also emphasizes the strong interfacial interaction between TiO_2 and gold nanoparticles. The emission at 432 nm corresponds to self-trapped excitons, which have been suggested to occur due to oxygen vacancies created by metal doping (here by Au metal).[29,30] The considerably increased intensity of shallow trap states after the deposition of gold nanoparticles infers increased radiative recombination at this level. The photoluminescence of the heterojunction on gold deposition shows a 5-fold enhancement after integrating the emission signals of TiO_2. This

suggests that the rate of semiconductor emission in a gold nanoparticle-decorated heterojunction system, which is a function of the concentration of electron–hole pairs in the semiconductor, is larger than that in the isolated heterojunction system. This can be explained only by the involvement of SPR of AuNPs, which increases the rate of electron–hole pair formation in the semiconductor due to a near-field effect. The photoexcited plasmonic AuNPs efficiently scatter resonant photons, increasing the average photon path length in the TiO_2 layer and ultimately resulting in an enhanced rate of exciton formation. More precisely, the defect emission energy (503 nm) is close to the SPR of gold nanoparticles as per the DRS spectra. This energy is absorbed by the gold nanoparticles, generating energetic electrons (hot electrons) in the high energy state within the Fermi level, which could be transferred from the gold nanoparticles into the conduction band of the TiO_2. After this, by combining with the holes in the VB of the TiO_2, relaxation occurs by emission of energetic photons, which results in an increase in the intensity of the other emission band of TiO_2.[31,32]

3.4.4 Photoelectrochemical Measurements:

The higher optical absorption can be useful for the photoconversion into electrical current generation. As the samples prepared show increased absorption and PL enhancement we carried out photocurrent experiments. The Silicon nanowires with TiO_2 and after gold nanoparticles deposition are used as active electrodes. Aqueous solution of 1M Na_2SO_4 acts as an electron donor. The photoelectrochemical measurements of the samples were studied in a solution under LED light illumination. **Figure. 3.6** shows the linear sweep voltammograms before and after gold nanoparticle deposition on the heterojunction. These voltammograms are recorded in the potential range between

-1 to +2 V, with Ag/AgCl as a reference electrode, under dark and white light illumination and with a scan rate of 100mV/s. Increase in the photocurrent is observed for gold nanoparticle-decorated samples over the dark current than the standard sample as evident in the **Figure 3.6A**. Spectrally resolved analysis plotted in the **Figure 3.6B** suggests substantially higher photocurrent at wavelength of 530 nm.

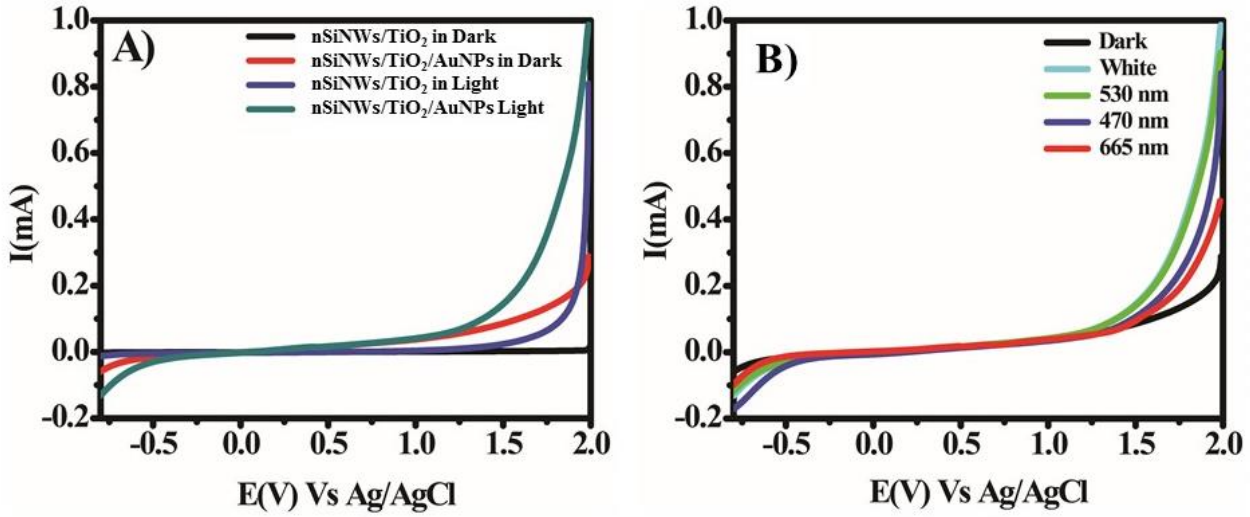

Figure 3.6. A) Linear sweep voltammograms (LSVs) of the nSiNWs/TiO_2 and nSiNWs/TiO_2/Au samples under dark and white light. **B)** LSVs under various wavelength irradiations.

The dynamic photocurrent i.e. at the time of on-off illumination is carried out and represented in **Figure 3.7**. At applied potential of 0.5 V versus Ag/AgCl as reference electrode, the SiNWs/TiO_2 heterojunction shows a maximum photocurrent of 0.33 µA/cm^2 under white light irradiation **(Figure 3.7A)**. The favourable band alignment for the possible photoexcited electron transfer and absorption of the visible light by the heterojunction are responsible for the current generation. AuNPs deposited heterojunction electrodes showed 25-fold enhancement in the photocurrent (~ 8.4 µA/cm^2). This increase in the current can be attributed to the possible role of the localized surface

plasmon on the gold nanoparticles revealing the usefulness of the higher optical absorption of the heterojunction as discussed above. A wavelength-dependent study was carried out and the results are presented in **Figure 3.7B**. When irradiated by a green LED light with central wavelength at 530 nm and with an incident power of 11.2 mW on the prescribed area of the electrode, i.e. 0.5 cm X 0.5 cm, the highest current is obtained as compared to the other wavelengths.

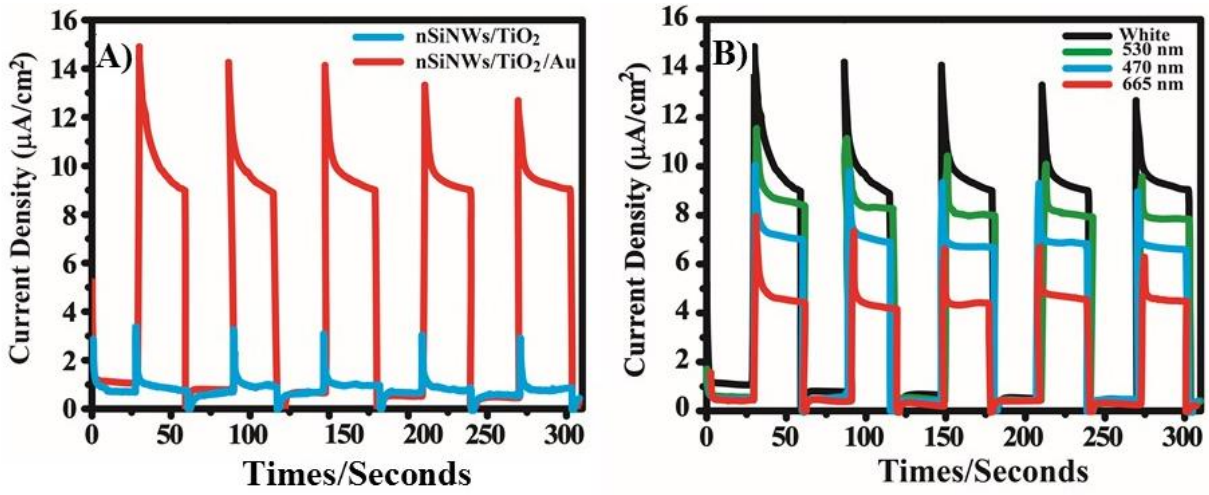

Figure 3.7. A) Photoresponse of heterojunction under white light irradiation. **B)** Wavelength dependent photoresponse of the nSiNWs/TiO_2/Au at bias of 0.5 V Vs Ag/AgCl in 1 M Na_2SO_4 as an electrolyte.

The gold deposited on the heterojunction has a maximum absorbance in the region of 400–550 nm, which is due to the combined effect of SPR and the dielectric strength of the TiO_2. Therefore, it is reasonable that the photocurrent response at 470 nm (~ 6.43 μA/cm^2) and 530 nm (~ 7.8 μA/cm^2) is because of the spectral overlap of the energy levels of the SPR of the gold nanoparticles and TiO_2. The photon energy (530 nm) is selectively absorbed by the gold nanoparticles over the highly energetic photons (470 nm) and hence the maximum photocurrent is observed under green light irradiation. The absorbance of the gold-decorated samples extends over the entire visible region, hence it should be able to convert incident photons of 665 nm wavelength as well, resulting in the

higher photocurrent (~ 4.14 µA/cm^2) at this wavelength. To produce photocurrent from the gold nanoparticle decorated nSiNWs/TiO_2, the electrons and holes must have to be transferred across the heterojunction (**Scheme 3.1**).

A barrier of 1.1 eV exists between the AuNPs–TiO_2 interface because of the difference in the work function of gold (~ 5 eV) and the electron affinity of TiO_2 (~ 3.9 eV)[33], which has to be overcome by the electrons so as to contribute to the current.

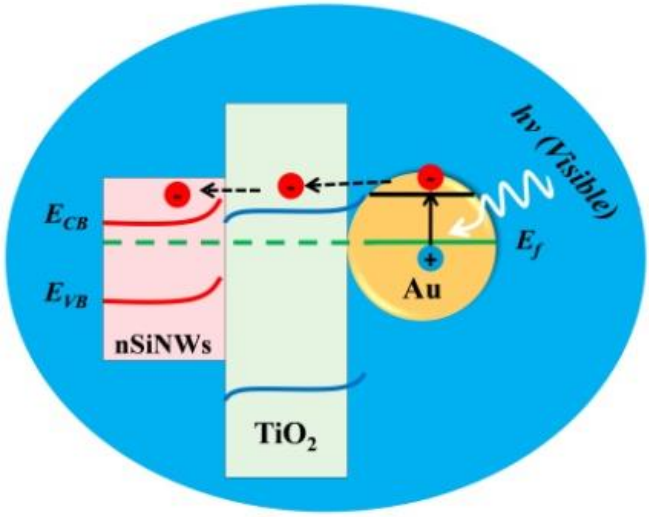

Scheme 3.1. Simplified illustration for the band energies and possible charge transfer from gold nanoparticle SPR level into the conduction band of TiO_2 under visible light illumination.

As the present study suggests, the increase in the photocurrent on visible light irradiation indicates that these electrons have enough energy to cross the Schottky barrier. Also, SPRs on gold can be stimulated by the defect emission (~ 2.5 eV) energy transfer. The excited SPRs might be responsible for the electron tunnelling from gold to the TiO_2 conduction band. As a result, electron density increases in the conduction band of TiO_2, leading to a higher recombination rate of

electron–hole pairs, which enhances the PL properties of TiO_2. All of this suggests a synergistic effect between TiO_2 emission and gold SPR involvement in the enhanced photoactivity of the heterojunction.

3.5 Conclusions:

A simple method has been presented for the synthesis of heterojunctions, along with improved and new properties of such heterojunctions resulting from deposition of gold nanoparticles. The influence of the SPR of gold nanoparticles on the optical and photocurrent properties of the nSiNWs/TiO_2 heterojunction has been investigated. Such gold plasmon-sensitized SiNWs/TiO_2 exhibits broadband visible light absorbance and photoresponse at matching wavelengths between the SPR and interband transitions. The enhanced absorption, enhanced rate of electron–hole pair formation, electric field amplification and simultaneous plasmonic energy transfer to the semiconductor is attributed to the increased response towards the multiwavelength photoconductivity of the heterojunction. The deposition of noble metal nanoparticles on semiconductors or semiconductor heterojunctions can be effectively used in the preparation of highly efficient optoelectronic devices.

3.6 References:

1] K. L. Kelly, E. Coronado, L. L. Zhao and G. C. Schatz, *J. Phys. Chem. B*, **2003**, 107, 668.

2] L. Gunnarsson, *J. Phys. Chem. B*, **2005**, 109, 1079.

3] J. A. Schuller, E. S. Barnard, W. Cai, Y. C. Jun, J. S. White and M. L. Brongersma, *Nature Mater*. **2010**, 9, 193.

4] M. Kauranen and A. V. Zayats, *Nature. Photon.* **2012**, 6, 737.

5] H. A. Atwater and A. Polman, *Nature Mater*. **2010**, 9, 205.

6] S. Nie and S. R. Emory, *Science*, **1997**, 275, 1102.

7] S. Kuhn, U. Hakanson, L. Rogobete and V. Sandoghdar, *Phys. Rev. Lett*. **2006**, 97, 017402.

8] B. Tian, X. Zheng, T. J. Kempa, Y. Fang, N. Yu, G. Yu, J. Huang and C. M. Lieber, *Nature Mater*. **2007**, 449, 885.

9] I. Hochbaum, R. Chen, R. D. Delgado, W. Liang, E. C. Garnett, M. Najarian, A. Majumdar and P. Yang, *Nature Mater*. **2008**, 451, 163.

10) J. Oh, H. C. Yuan, and H. M. Branz, *Nature Nanotechnol*. **2012**, 7 (11), 743.

11) G. Jia, M. Steglich, I. Sill, and F. Falk, *Energy Mater. Sol. Cells*, **2012**, 96, 226.

12) E. C. Garnett and P. Yang, *J. Am. Chem. Soc*. **2008,** 130 (29), 9224.

13) J. M. Weisse, C. H. Lee, D. R. Kim, and X. Zheng, *Nano Lett.* **2012**, 12 (6), 3339.

14) K. Rasool, M. A. Rafiq, C. B. Li, E. Krali, Z. A. K. Durrani, and M. M. Hasan, *Appl. Phys. Lett.* **2012**, 101 (2), 023114.

15] X. Chen and S. S. Mao, *Chem. Rev*. **2007**, 107, 2891.

16] R. Asahi, T. Morikawa, T. Ohwaki, K. Aoki and Y. Taga, *Science*, **2001**, 293, 269.

17] Y. J. Hwang, A. Boukai and P. Yang, *Nano Lett*. **2009**, 9, 410.

18] H. Yu, X. Li, X. Quan, S. Chen and Y. Zhang, *Environ. Sci. Technol*. **2009**, 43, 7849.

19] K. R. Catchpole and A. Polman, *Opt. Express*, **2008**, 16, 21793.

20] D. Bersani, P. P. Lottici and X. Z. Ding, *Appl. Phys. Lett*. **1998**, 72, 73.

21] R. Wang, G. Zhou, Y. Liu, S. Pan, H. Zhang, D. Yu and Z. Zhang, *Phys. Rev. B: Condens. Matter Mater. Phys*. **2000**, 61, 16827.

22] B. Li, D. Yu and S. L. Zhang, *Phys. Rev. B: Condens. Matter Mater. Phys*. **1999**, 59, 1645.

23] M. Fernandez Garcıa, X. Wang, C. Belver, J. C. Hanson and J. A. Rodriguez, *J. Phys. Chem. C*, **2007**, 111, 674.

24] N. Serpone, D. Lawless and R. Khairutdinovt, *J. Phys. Chem*. **1995**, 99, 16646.

25] Y. Lei, L. D. Zhang, G. W. Meng, G. H. Li and X. Y. Zhang, *Appl. Phys. Lett*. **2001**, 78, 1125.

26] G. Mattioli, F. Filippone, P. Alippi and A. M. Bonapasta, *Phys. Rev. B: Condens. Matter Mater. Phys.* **2008**, 78, 241201.

27] I. Chung, B. Lee, J. He, R. P. H. Chang and M. G. Kanatzidis, *Nature*, **2012**, 485, 486.

28] L. V. Saraf, S. I. Patil, S. B. Ogale, S. R. Sainkar and S. T. Kshirsager, *Int. J. Mod. Phys. B*, **1998**, 12, 2635.

29] K. Iijima, M. Goto, S. Enomoto, H. Kunugita, K. Ema, M. Tsukamoto, N. Ichikawa and H. Sakama, *J. Lumin.* **2008**, 128, 911.

30] B. Choudhury, M. Dey and A. Choudhury, *Appl. Nanosci*. **2013**, 4, 499.

31] C. W. Cheng, E. J. Sie, B. Liu, C. H. A. Huan, T. C. Sum, H. D. Sun and H. J. Fan, *Appl. Phys. Lett.* **2010**, 96, 071107.

32] H. Y. Lin, C. L. Cheng, Y. Y. Chou, L. L. Huang and Y. F. Chen, *Opt. Express*, **2006**, 14, 2372.

33] G. Rothenberger, D. Fitzmaurice and M. Gratzel, *J. Phys. Chem*. **1992**, 96, 5983.

Optical Antenna Effect on SiNWs/CuS photodiode

This chapter is based on the photodetection investigation of the SiNWs/CuS heterojunction by sensitization with gold nanorods (AuNRs). CuS was deposited on silicon nanowires by Radio Magnetron Sputtering and analyzed for the solid-state photodetector application. AuNRs serving as light trapping antenna enhances the photocurrent from the photodiode by simply dropcasting AuNRs on the surface of the devices.

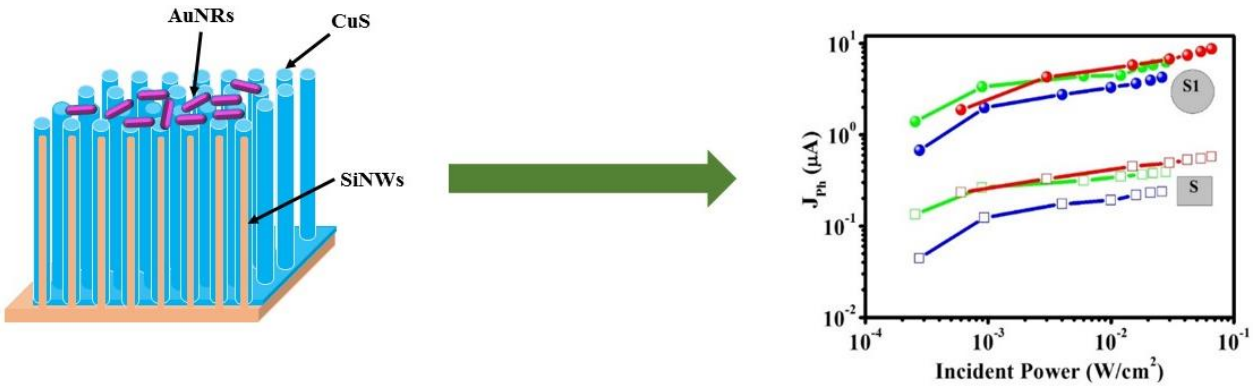

Schematics of the fabricated device and experimental results

A maximum photo responsivity of 0.36 mA/W was achieved under 665 nm excitation wavelength on independent of bias which is ~ 13 times higher than heterojunction. Such plasmonic sensitization can be useful for enhanced sensitivity of visible as well as IR light photodetectors.

4.1 Introduction:

Plasmonic nanostructures nowadays are studied extensively for efficient light trapping properties based on their high scattering efficiency in solar spectrum.[1,2] Not only they enhance total absorbance by subwavelength localization of electromagnetic radiation but also boost photodetection performance of the device. By introducing such optical antennas in conjunction with other materials, the enhancement in the efficiency and performance of the solar cells and other optoelectronic devices have been demonstrated.[3-5] The optical scattering by metal nanoparticles indirectly improves sensitivity of the photodetectors by the semiconductor band gap absorption.[6-9]Photoelectron emission by non-radiative plasmon decay itself contributes in the optical response as in terahertz photodetectors.[10-12]

One dimensional SiNWs and its heterojunctions are being important in many optoelectronic device applications. Such junction offers radial direction separation and swift collection of charges in regard of carrier diffusion length.[13-15] CuS as a direct bandgap material with absorption in visible region, exhibits p-type behaviour. It has been an interesting candidate for various optoelectronic devices of a wide range such as photodiodes and photovoltaics.[16, 17]

Optical response of photodiode is measured in the visible spectrum. The heterojunction performs rapid on-off response with respect to the light dynamics independent of bias potential. Gold nanorods were then dropcasted on the device top surface which enhances the photoresponse indicating the light trapping in the heterojunction.

4.2 Experimental Methods:

4.2.1 SiNWs Fabrication:

We have fabricated a radial photodiode between SiNWs and CuS. Electroless chemical deposition method used to grow vertically aligned SiNWs on the Silicon surface. Precleaned n-Si wafers (100, Res. 0.01-0.02 Ω) and N_2 blow dried wafers directly placed in etchant or silver plating solution (0.001 M $AgNO_3$ + 5% HF) for 30 seconds. After removing from the silver plating solution the wafer washed with DI water and immersed in 4.8 M HF and 0.30 M H_2O_2 to etch the silicon surface for 1 hr at room temperature. Etched wafers rinsed several times with DI water. The Ag deposited on the wafer was removed by using 5M HNO_3. The wafers were dried under N_2 gas and used for the further process.

4.2.2 RF Magnetron Sputtering of CuS:

The CuS was deposited on SiNWs by Radio Frequency Magnetron Sputtering method. Briefly, the H terminated SiNWs arrays placed in the deposition chamber. The distance between sputtering target CuS (99.99% purity) and substrate was about 60 mm and the substrate holder rotated at a frequency of 10 rev/ min. Argon gas was solely introduced as both reactive and working gas during the sputter deposition with a flow of 30 sccm and the sputtering pressure was controlled to $6x10^{-3}$ mbar. During deposition RF power was 100 watt and growth time was 60 min. CuS thin films were produced in a RF sputtering system mainly with a planar magnetron sputter gun and automatic tuning network.

4.2.3 Gold Nanorods synthesis:

AuNRs are synthesized by well knows protocol as described below in brief.[18] In 5 ml of gold salt aqueous solution (0.5 mM $HAuCl_4$) 5 ml of CTAB solution (200 mM) was added with stirring. Ice cold $NaBH_4$ (0.6 ml, 10 mM) was added to the above solution forming a brownish yellow solution. The seed solution kept at 25 °C after continuous stirring for 2 minutes. Growth solution was prepared by mixing 5 ml of CTAB solution (200 mM) with 0.15 ml of $AgNO_3$ (4 mM) followed by 5 ml $HAuCl_4$ (1 mM). The solution was mixed gently and 75 µl of L-Ascorbic acid (78.8 mM) was added to reduce Au (III) to Au (I). 12 ml of seed solution was added to the colourless growth solution and allowed to stand for 2 hr without stirring. The temperature of the growth medium was kept constant at 27-30 °C in all the experiments.

4.3 Result and Discussion:

4.3.1 SEM and TEM:

Figure 4.1 represents morphology of the SiNWs and the heterojunction observed by scanning electron microscopy. Etching of the silicon surface by electroless metal deposition process produces a high density 1D SiNWs which grows perpendicular or in the z-direction onto the Silicon substrate. The average length and the diameter of the SiNWs measured are ~ 5 µm and in between ~ 70-150 nm respectively. **Figure 4.1B** and **C** show CuS deposited on the SiNWs covering the individual nanowires as well as the spaces in between them. We can also see the gold nanorods (AuNRs) on the surface of the heterojunction as in the **Figure 4.1D**. The inset represents transmission electron microscopic images of AuNRs synthesized in this study. The diameter and length of the AuNRs were measured to be ~13 nm and ~ 40 nm respectively.

.

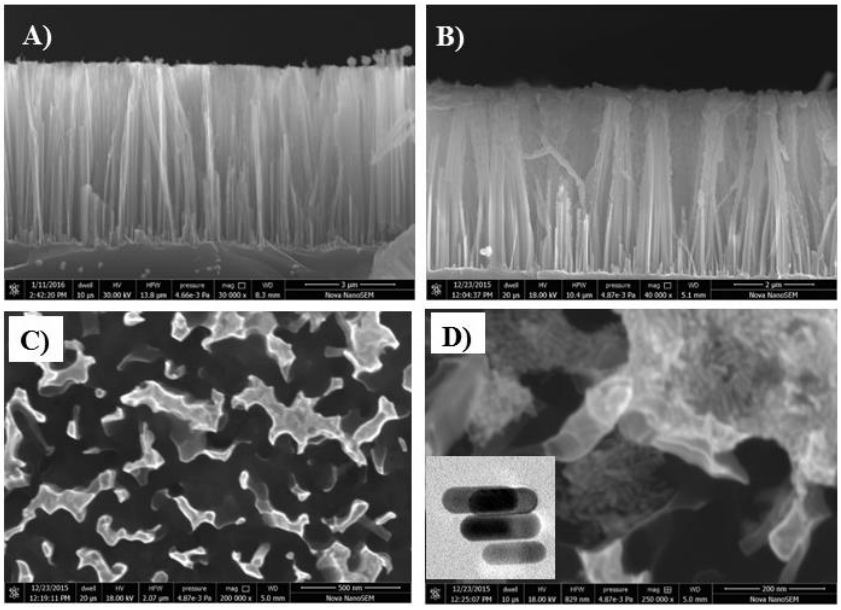

Figure 4.1. (A) FE-SEM cross section view of silicon wafer with vertically aligned Silicon Nanowires. **(B)** Transverse view. **(C)** Top view for RF magnetron sputtered CuS on the SiNWs surface. **(D)** Heterojunction with AuNRs. Inset- TEM image of AuNRs.

4.3.2 X-ray Diffraction and Raman Spectroscopy:

X- ray diffraction and Raman spectroscopy measurements were carried out to understand the phase and crystallinity of the as deposited CuS film. The dominant covellite phase structure was indicated by the XRD peaks in the **Figure 4.2A**, corresponding to (102), (006), (110), and (116) CuS crystallographic planes (JCPDS 00-006-0464) with space group P63/mmc.[19]

The covellite structure of the CuS film has been further confirmed from the Raman analysis (633 nm laser, 5 mW) as represented in the **Figure 4.2B**. Two Raman peaks for CuS appears in the spectrum, strong one a transverse optical (TO) phonons mode at 474 cm^{-1} for stretching mode in S-S and a weak peak belongs to longitudinal optical (LO) phonon mode at 265 cm^{-1} for the Cu-S vibration.[20] The other peaks 300 cm^{-1} and 520 cm^{-1} are characteristics of the various silicon vibrational modes such as TA and 2TO respectively.

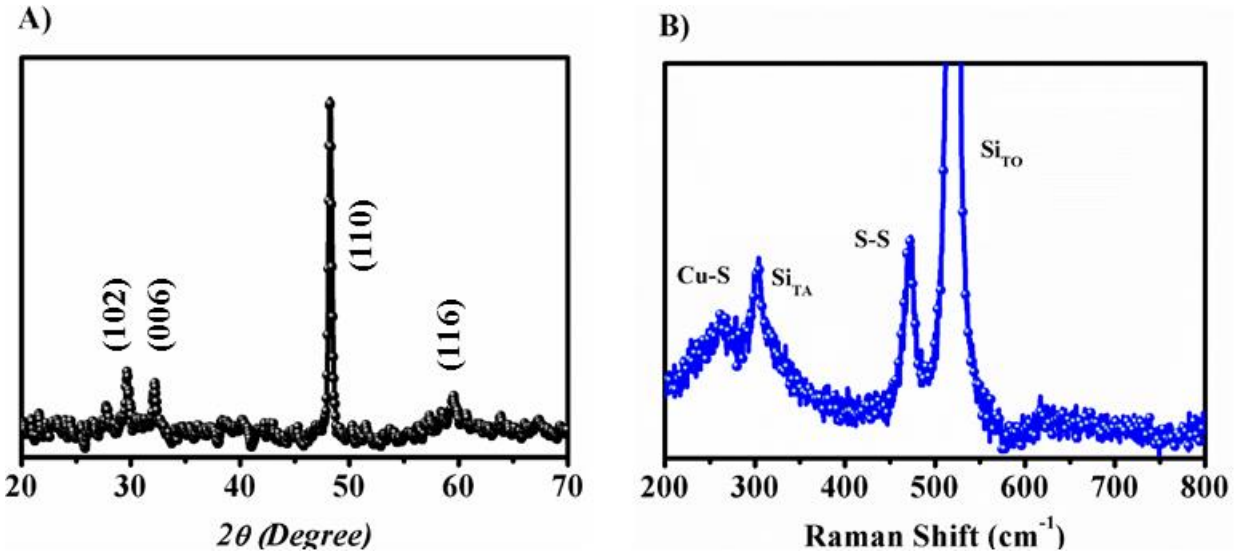

Figure 4.2. (A) X-Ray diffraction pattern of CuS prepared by RF magnetron sputtering. **(B)** Raman spectra of SiNWs/CuS heterojunction.

4.3.3 UV-Vis absorbance and Diffuse Reflectance Spectra:

As synthesized Gold nanorods are analysed by UV-Vis absorbance spectra. Two plasmon resonances can be observed as the characteristics for the AuNRs as seen in the **Figure 4.3A**. The transverse plasmon appears at 516 nm while longitudinal plasmon at 764 nm.

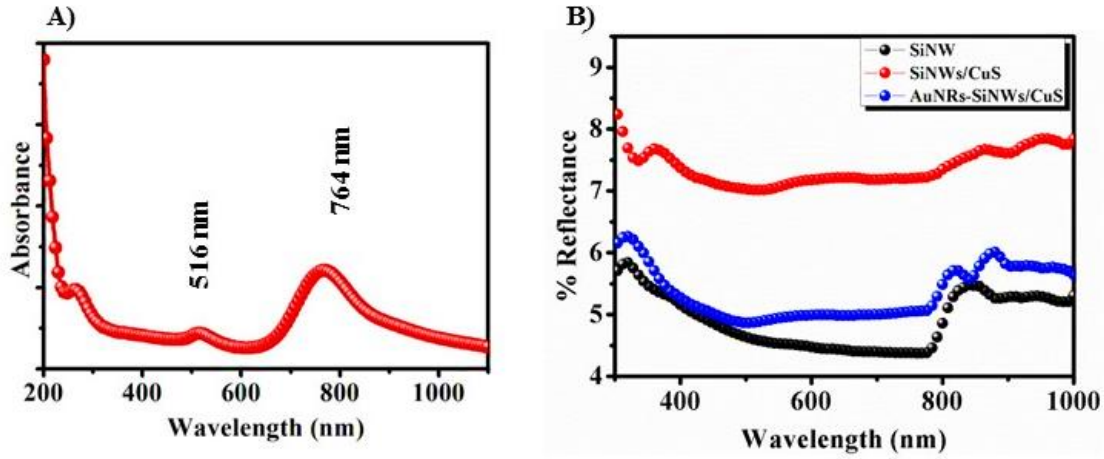

Figure 4.3. (A) Absorbance spectrum of aqueous AuNRs solution. **(B)** Diffuse Reflectance spectra of SiNWs, CuS deposited SiNWs and after AuNRs deposition film.

The CuS not only covers the SiNWs but also the space between the nanowires so that the internal reflection is reduced and consequently results into the low absorption than the SiNWs. However, the same device displays lower reflectance (~ 5%) after dropcasting the AuNRs on its surface. The band gap of the CuS film is measured to be 1.80 eV using the Kubelka-Munk function plot.[21]

In the visible region the device absorbance slightly broadens from 600-800 nm probably due to the coupling of CuS exciton and surface plasmons. It is well known fact that the metallic nanoparticles act as light trapping system and thereby enhances the absorption properties of the device.

4.3.4 Electrical Measurements:

The current density (J) *vs* bias potential (V) analysis was performed with semiconductor parameter analyser (Keithley-4200 SCS) and represented in the **Figure 4.4**.

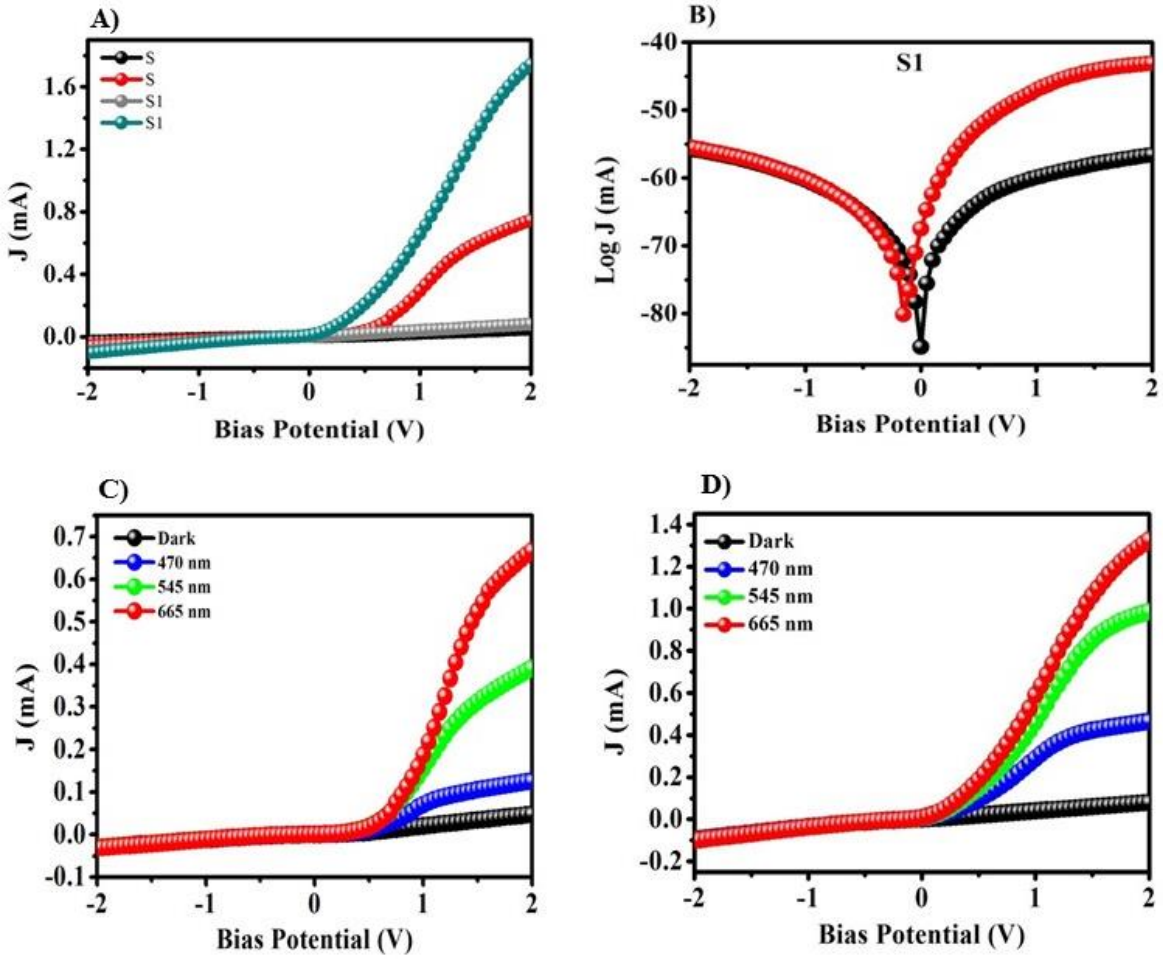

Figure 4.4. (A, B) Current density Vs bias potential curves of the device without (S) and with AuNRs (S1) in Dark (black and blue color line) and on 665 nm excitation wavelength (red and magenta color line). **(C)** Bias dependent J_{Ph}/J_D ratio. **(D)** Optical responsivity of the same devices.

The SiNWs/CuS photodiode with control device (S) and AuNRs deposited device (S1) shows well behaved J-V curves in the dark and light illumination ($\lambda \sim 665$ nm, ~18 mW/cm^2).

The J-V curves of the diodes show the ohmic behaviour in the dark which indicates the formation of a junction between the CuS film and n-Si. The rectifying nature of the heterojunction can be observed on the excitation wavelength 665 nm at forward bias for both devices. However, the AuNRs modified device appears to have stronger photoresponse as in **Figure 4.4A**.

The dark current of the diodes S and S1 are approximately 1.94 x10^{-5} A and 3.63 x 10^{-5} A, while the photocurrents increased to 1.9 x 10^{-4} A and 5.3 x 10^{-4}A at 1 V bias respectively. **Figure 4.4B** represents the log I vs V characteristics where the heterojunction with AuNRs generates - 0.15 V of open circuit voltage on the irradiation. The device S exhibits higher photoresponse for the wavelength 665 nm than other i.e. 530 nm and 470 nm as seen in the **Figure 4.4C**. AuNRs further enhance the photocurrent generation from the sample S as represented in the **Figure 4.4D**.

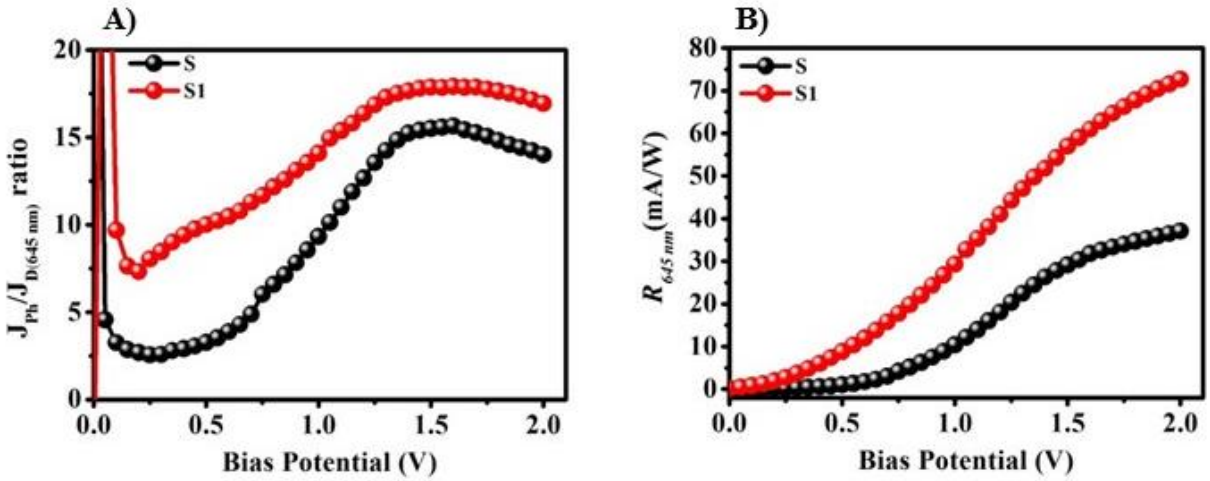

Figure 4.5. Bias dependent **(A)** Photocurrent ratio. **(B)** Responsivity for both the samples S and S1 on excitation wavelength of 665 nm.

The J_{Ph}/J_D ratio Vs Bias Potential (Photoconductive gain, $\eta = J_{Ph}/J_D$) indicates the higher photosensitivity of the device with AuNRs in **Figure 4.5A**. Both devices show maximum response in the range of 1 to 1.6 V corresponding to the 665 nm excitation wavelength. After AuNRs deposition on the device the J_{Ph}/J_D ratio or the photoconductive gain increases. The same is true for the responsivity plotted in the **Figure 4.5B**.

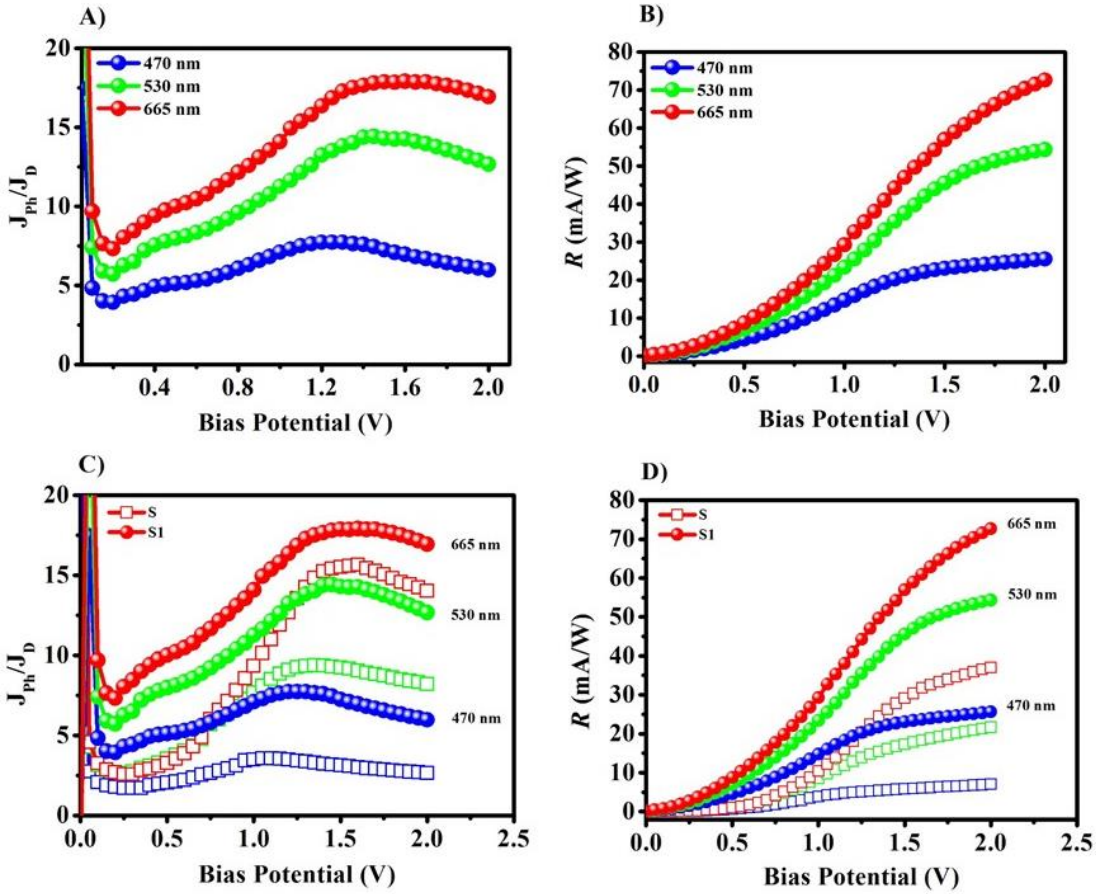

Figure 4.6. (A, B) Bias dependent J_{Ph}/J_D ratio and responsivity of the device S1 on various wavelength excitation. **(C, D)** Comparative J_{Ph}/J_D and responsivity as a function of applied bias for the device S and S1.

A comparative data of bias dependent photoconductive gain and responsivity is plotted for the sample S1 (**Figure 4.6B**) after excitation by various wavelengths. Both photoconductive gain and responsivity is higher at wavelength 665 nm for the device S1 i.e. with AuNRs suggesting the higher absorption of the near infrared wavelength by the device. Altogether both characteristics are represented in the **Figure 4.6A** and **B** indicating higher response due to AuNRs deposition on the heterojunction device.

One can clearly see that the maximum J_{Ph}/J_D ratio has different potential values at various wavelengths and is also different for the two devices. It is obvious that at higher potential more photocurrent generation results into higher responsivity. It is to be noted that the AuNRs modified photodiode shows higher photocurrent ratio and responsivity due to the higher absorption by optical antenna effect. **Table 1** represents the J_{Ph}/J_D ratio measured at their maximum alongwith responsivities measured at 1V bias potential at various wavelengths. The responsivity ($R_{665\ nm}$) measured for photodiode S is 10.4 mA/W which reaches to 29.3 mA/W for photodiode S1 at 1 V bias potential. This specifies ~ 2.8 times enhancement in the responsivity of the photodiode S1 due to higher absorption. The device indicates the significance of optical trapping owing to presence of AuNRs.

Table 1: Summarized J_{Ph}/J_D ratio, Responsivity for the devices S an S1.

	J_{Ph}/J_D ratio at the maximum		**Responsivity (mA/W) at 1V**	
λ (nm)	**S**	**S2**	**S**	**S2**
665 nm	15.76	17.94	10.4	29.3
530 nm	9.44	14.41	8.55	23.3
470 nm	3.54	7.81	3.87	14.75

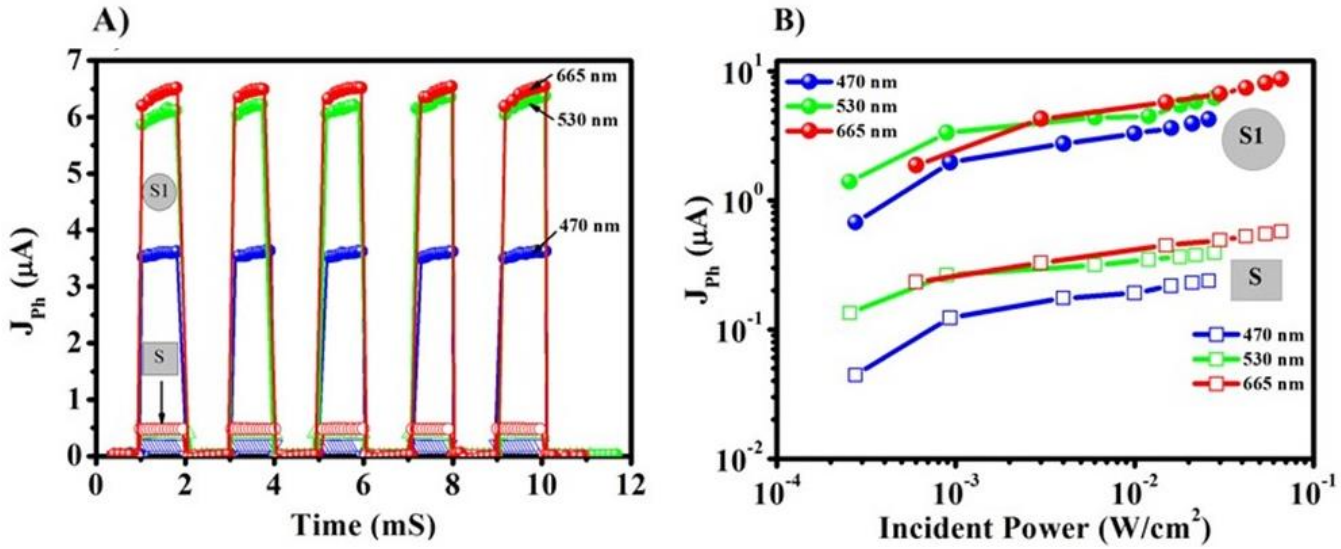

Figure 4.7. (A) Dynamic photoresponse. **(B)** Photocurrent vs incident power for the device S and S1 on different excitation wavelength.

The comparative photoresponse plot of both the devices on irradiation by various wavelengths is plotted in the **Figure 4.7A**. Both the devices show a quick and strong response. It is evident that the heterojunction efficiently generates and sweeps out charged carriers. The photoresponse for the device S1 is considerably enhanced than the device S. Gold nanorods in the device S1 effectively scatters incoming radiation in the heterojunction which increases the photogenerated carriers and subsequently increases the photocurrent.

Figure 4.7B shows the photocurrent density as a function of the intensity of the excitation wavelength. On increasing the energy, more electron-hole pairs generated resulting into high photocurrent. The AuNRs as an optical antenna increase the absorption of the device producing

higher amount of e-/h+ pairs than the standard device. It also confirms the sublinear power law behaviour of the device.

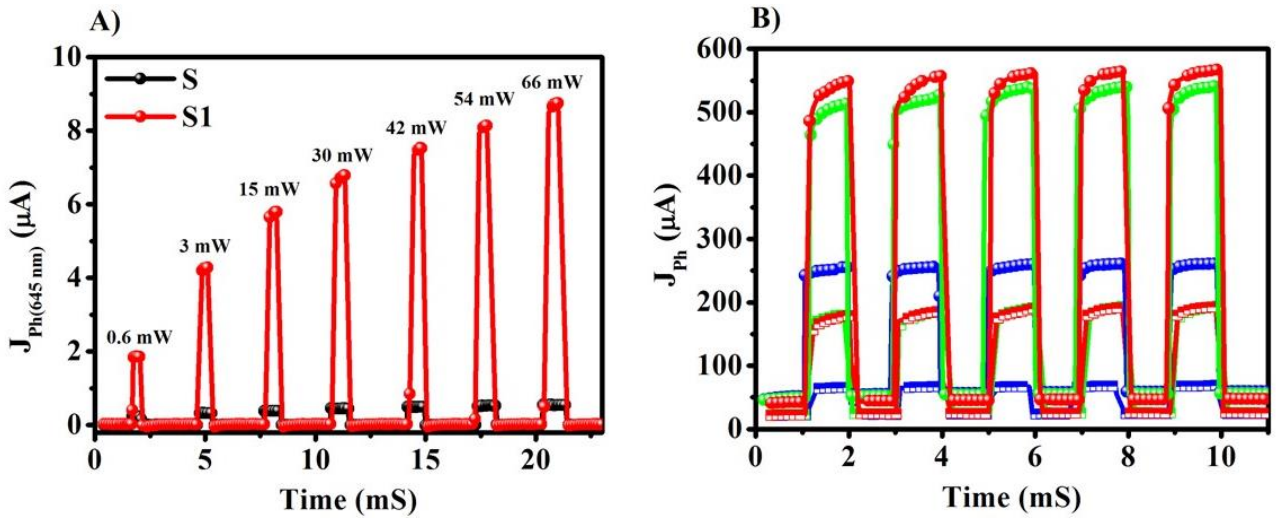

Figure 4.8. (A) Photocurrent as a function of light intensity (λ ~ 665 nm). **(B)** Wavelength dependent transient photocurrent at 1V for device S and S1.

Figure 4.8A represents the dynamic photocurrent vs incident power of 665 nm wavelength on the devices at zero bias which is used for the calculation of photocurrent density with respect to the incident power. There is substantial increase in the dynamic photocurrent at potential set to 1V as shown in the **Figure 4.8B**.

The photodetector figures of merit such as responsivity (R) and detectivity (D) are measured and plotted in the **Figure 4.9 (A, D)** alongwith photocurrent (J_{Ph}) as a function of incident power (λ_{exe}= 665 nm). R and D values for both the devices, calculated using following standard equations,

$$D = \frac{J_{Ph}\sqrt{A}}{P_{Opt}\sqrt{2qJ_D}} \quad \ldots\ldots\ldots\ldots 1)$$

$$R = \frac{J_{Ph}}{P_{Opt}} \quad \ldots\ldots\ldots\ldots 2)$$

where,

D = Specific detectivity (Shot noise i.e. when dark current equals to noise current)

R= Responsivity

$J_{Ph} = \text{Photocurrent}$

$J_D = \text{Dark Current}$

$P_{Opt} = \text{Incident optical power}$

q = Electron charge

A = Effective area of the device

On excitation at λ~ 665 nm, both photocurrent and responsivity of the device S1 reaches to 1.87 μA/cm^2 and 3.12 mA/W at incident power of 0.6 mW/cm^2 respectively which is ~7 times higher the sample S.

The detectivity value for the sample S1 was found to be 3.19 X 10^{10} Jones ~ 3 times higher than the standard sample under same wavelength and power. The measurement clearly shows that the increased photoresponse of the SiNWs/CuS heterojunction due to AuNRs deposition on the surface. The optical scattering of the AuNPs enhances the absorption of the heterojunction in the visible region which results into improved detection capabilities of the samples. The device shows a high R and D values under low excitation power at 0 V suggesting that the built-in potential can efficiently separate photoelectrons on incident photon energy resulting into a large electrical signal.

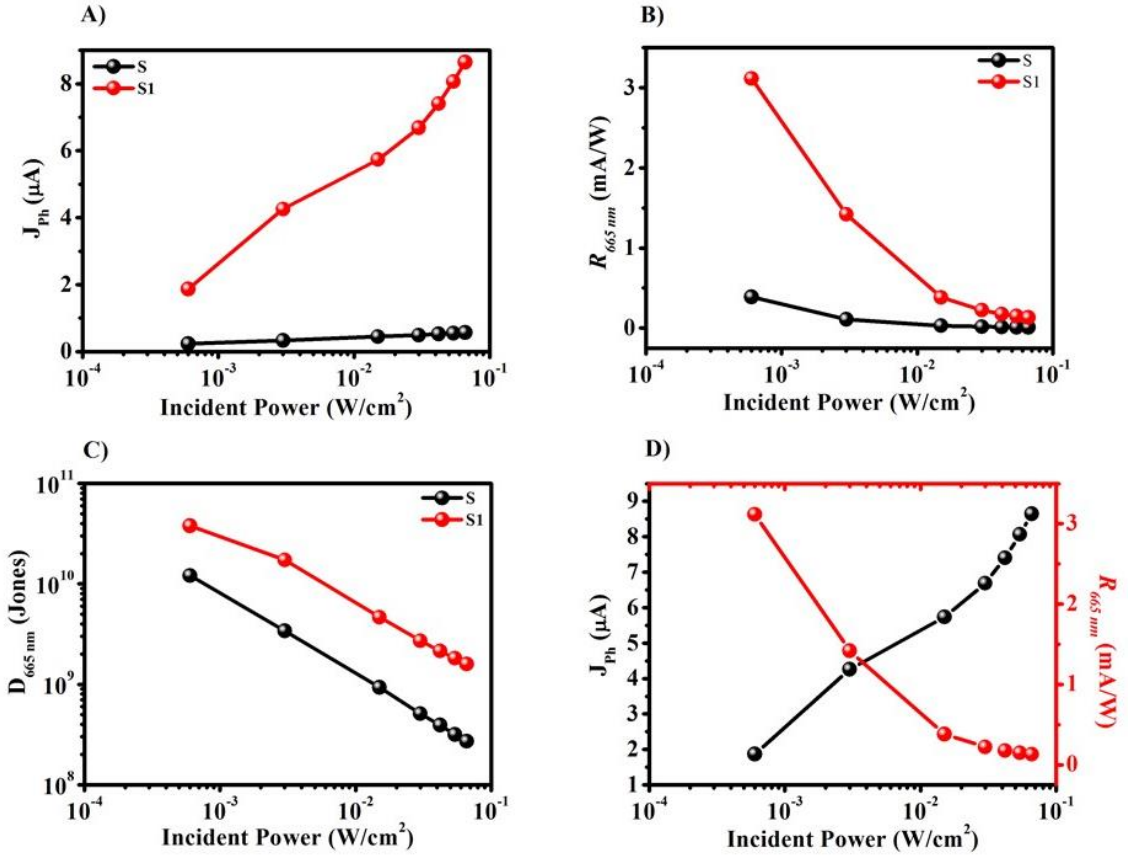

Figure 4.9. Incident power (λ~ 665 nm) dependent **(A)** Photocurrent (J_{Ph}). **(B)** Responsivity (R). **(C)** Detectivity (D) of the device S and S1. **(D)** Combined plot of Photocurrent and Responsivity of the device S1.

Same measurements are carried out for both the devices on excitation of other wavelengths i.e. 470 nm and 530 nm and plotted in the **Figure 4.10** and **4.11**.

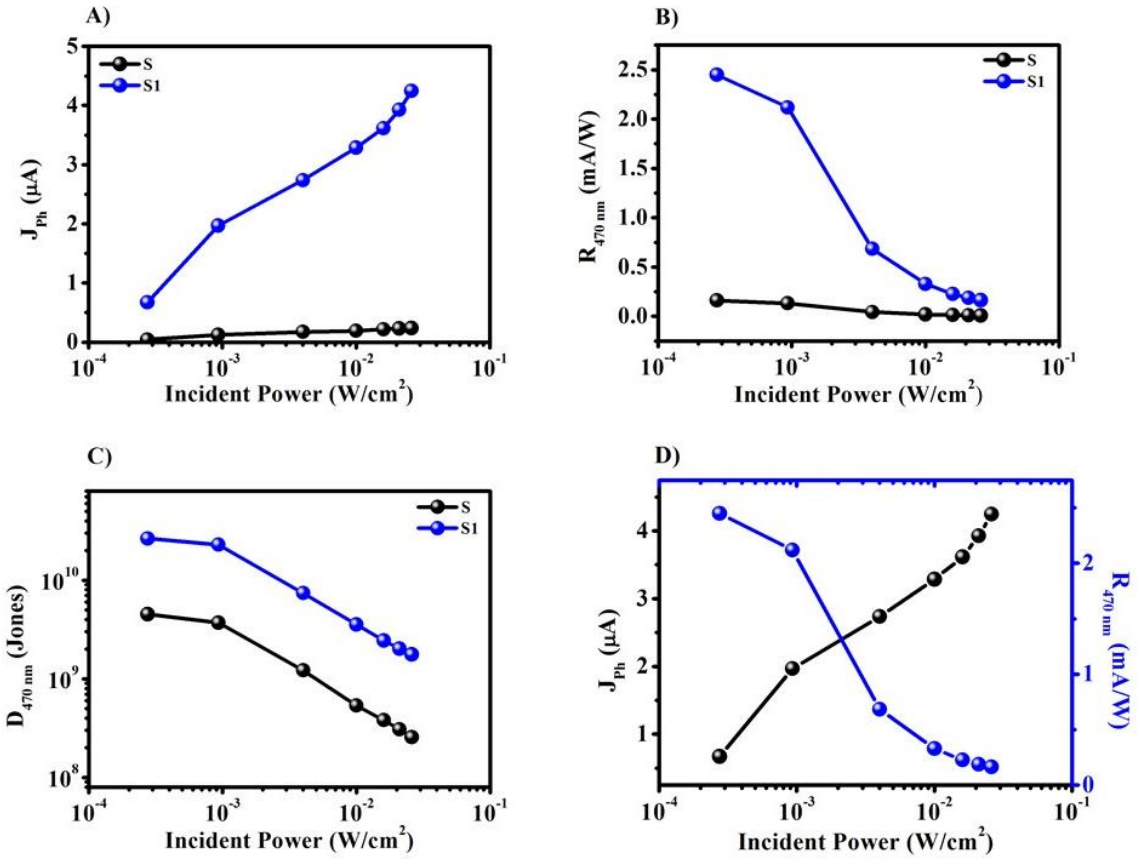

Figure 4.10. Incident power dependent **(A)** Photocurrent (J_{Ph}). **(B)** Responsivity (R). **(C)** Detectivity and with **(D)** combined plot of J_{Ph} and R on excitation wavelength ~ 470 nm respectively.

The heterojunction therefore shows increase in the optical absorption consequently more photoexcited electrons are generated. The inbuilt potential extracts more electrons resulting in large photocurrent. The mechanism of electron separation in the heterojunction can be understood from the band alignments.

The values of band gap (Eg) and electron affinity (χ_{Si}) for Si are 1.12 eV and 4.05 eV.[22] While the calculated band gap of CuS is 1.80 eV with its electron affinity of 1.91 eV.

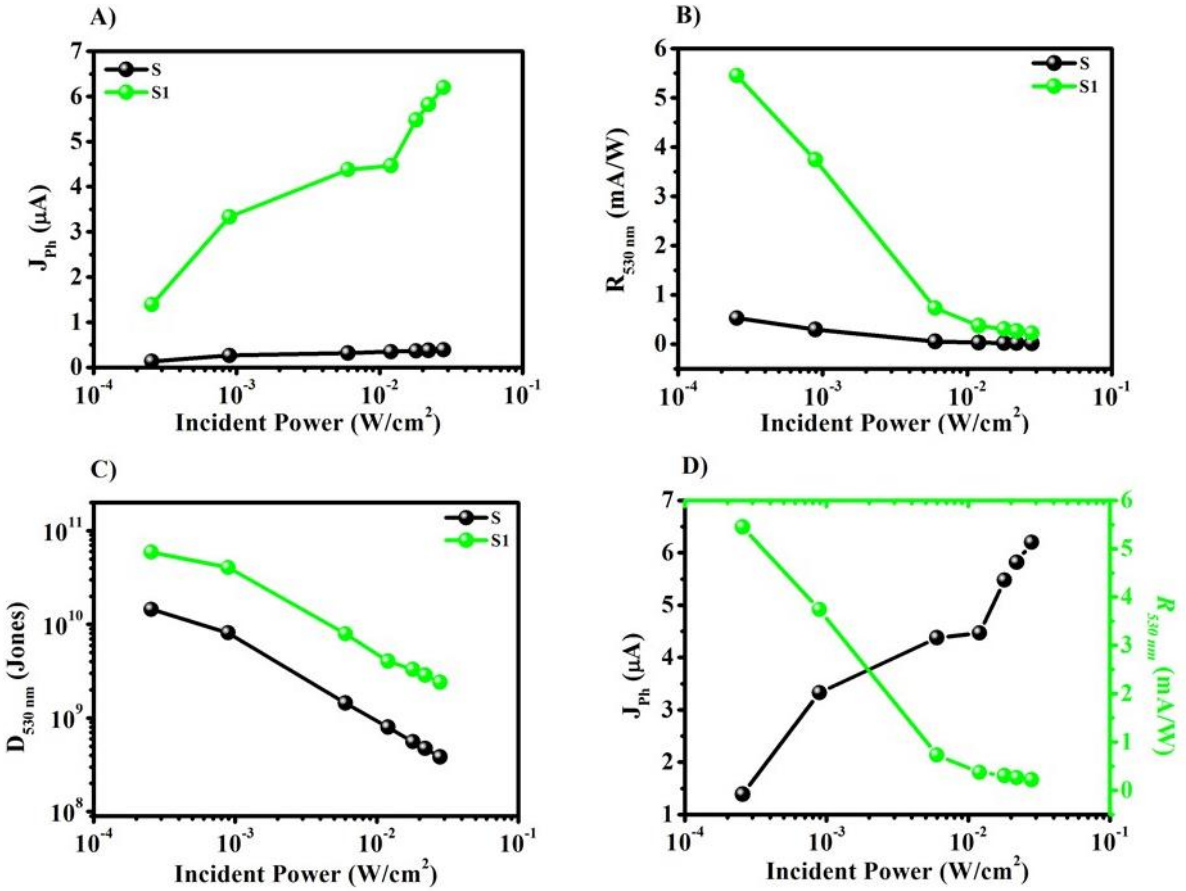

Figure 4.11. Incident power dependent **A)** Photocurrent (J_{Ph}). **(B)** Responsivity (R). **(C)** Detectivity and **(D)** combined plot of J_{Ph} and R on excitation wavelength ~ 530 nm respectively.

Band offsets between the Si and CuS based on Andersons approximation represented in the **Figure 4.12**.[23]The heterojunction clearly represents large conduction band offset (ΔEc) value of 2.14 eV and valence band offset value of (ΔEv) 1.46 eV for electron and hole transport. The photoelectrons from the CuS conduction band diffuses to the conduction band of the silicon due to the energy difference producing appreciable photocurrent.

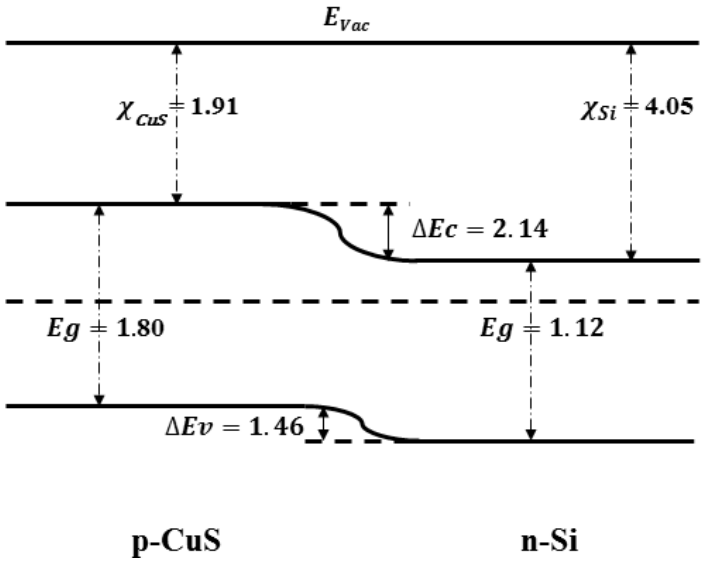

Figure 4.12. Band energy alignment in the SiNWs/CuS heterojunction (all values in eV.)

The plasmonic metal nanorods further increase the photogenerated exciton pairs in the CuS. This increases the total output photocurrent which is a result of absorption enhancement of the semiconductor heterojunction. Difference of work function between CuS and SiNWs may also influence the band alignment which causes Fermi level displacement and therefore reduces the effective barrier to current flow in light.

4.4 Conclusion:

The heterojunction diode between SiNWs and CuS is fabricated by resonant magnetron sputtering and displays stable, quick and good photoresponse. The responsivity of 0.027 mA/W of the SiNWs/CuS junction is increased ~13 times i.e. 0.36 mA/W for AuNRs deposited device at open circuit voltage. The result indicates that the optical antenna effect of AuNRs enhances the photocurrent, responsivity and detectivity of the photodiode. Both the devices are operating on the independent bias and able to differentiate specific wavelengths. The observed photodetector figures of merits are based on low temperature device fabrication.

We believe that they can be further improved by optimizing the CuS sputtering time and film thickness. The use of metal nanostructure can enhance the optical properties of the semiconductor devices which is enormously applicable for high speed photodetector.

4.5 References:

1) J M Pitarke, V M Silkin, E V Chulkov, and P M Echenique, *Rep. Prog. Phys.* **2007**, 70, 1.

2) P. Spinelli and A. Polman, *Optics Express*, **2012**, 20, A641.

3) Harry A. Atwater and Albert Polman, *Nature Mater.* **2010**, 9, 205.

4) G. Konstantatos and E. Sargent, *Nature Nanotech.* **2010**, 5, 391.

5) K. Kneipp, H. Kneipp Y. Wang, L. T. Perelman, I. Itzkan, R. R. Dasari, and M. S. Feld, *Phys. Rev. Lett.* **1997**, 78, 1667.

6) D. M. Schaadt, B. Feng, and E. T. Yu, *Appl. Phys. Lett.* **2005**, 86, 063106.

7) L. Huang, C. Tu, and L. Y. Lin, *Appl. Phys. Lett.* **2011,** 98, 113110.

8) Y. K. Lee, C. H. Jung, J. Park, H. Seo, G. A. Somorjai, and J. Y Park, *Nano Letters*, **2011,** 11, 4251.

9) B. Y. Zheng, Y. Wang, P. Nordlander, and N. J. Halas, *Adv. Mater.* **2014**, **26**, 6318.

10) M. W. Knight, H. Sobhani, P. Nordlander, and N. J. Halas, *Science*, **2011**, 332, 702.

11) S. S. Mousavi, A. Stöhr, and P. Berini, *Appl. Phys. Lett.* **2014**, 104, 143112.

12) W. Wu, A. Bonakdar, and H. Mohseni, *Appl. Phys. Lett.* **2010**, 96, 161107.

13) K. Rasool, M. A. Rafiq, M. Ahmad, Z. Imran, and M. M. Hasan, *Appl. Phys. Lett.* **2012**, 101, 253104.

14) Y. Cheng, G. Fang, C. Li, L. Yuan, L. Ai, B. Chen, X. Zhao, Z. Chen, W. Bai, and C. Zhan, *J. Appl. Phys.* **2007**, 102, 083516.

15) S. G. Yenchalwar, V. K. Azhagan, and M. V. Shelke, *Phys. Chem. Chem. Phys.* **2014**, 16, 17786.

16) H. Hiramatsu, M. Orita, M. Hirano, K. Ueda, and H. Hosono, *J. Appl. Phys.* **2002**, 91, 9177.

17) K. D. Yuan, J. J. Wu, M. L. Liu, L. L. Zhang, F. F. Xu, L. D. Chen, and F. Q. Huang, *Appl. Phys. Lett.* **2008**, 93, 132106.

18) B. Nikoobakht and M. A. El-Sayed, *Chem. Mater.* **2003**, 15, 1957.

19) H.S. Sanchez Rangel, A. Carrillo Castillo, J.F. Hernandez Paz, J.R. Farias Mancilla, H. Camacho Montes, P.E. Garcia Casilas, C.A. Martinez Perez, and C.A. Rodriguez Gonzalez, *Chalcogenide Letters*, **2015**, 15, 381.

20) A. G. Milekhin, N. A. Yeryukov, L. L. Sveshnikova, T. A. Duda, E. E. Rodyakina, V. A. Gridchin, E. S. Sheremet, and D. Zahn, *Beilstein J. Nanotechnol.* **2015**, 6, 749.

21) M. Nowak, B. Kauch, and P. Szperlich, *Review of Scientific Instruments*, **2009**, 80, 046107.

22) Z. Guo, D. Zhao, Y. Liu, D. Shen, J. Zhang, and B. Li, *Appl. Phys. Lett.* **2008**, 93, 163501.

23) R. L. Anderson, *Solid State Electronics,* **1962**, 5, 341.

Conclusion and Future Work

We have demonstrated the application of surface plasmon on the metal nanostructures in order to enhance the optical absorption and photodetection properties of the functionalized graphene, metal-semiconductor heterojunction between SiNWs/TiO_2, SiNWs/CuS in chapter 2, 3 and 4 respectively. Interesting coupling of surface plasmon is observed through optical absorption improvement and subsequently utilized for photocurrent enhancement. In this chapter, we will summarize the surface plasmon characteristics found in our studies and propose new research directions on surface plasmon application in optoelectronic devices.

5.1 Conclusions

Metal nanostructure possessing the surface plasmon resonance are the foundation on account of their high absorption/scattering cross section, ability to concentrate light in the nanoscale space. These plasmonic metal nanostructures nowadays are extensively being exploited for efficient optical trapping in solar spectrum due to their high scattering efficiency. Not only they enhances total absorbance by subwavelength localization of electromagnetic radiation but also boost photodetection performance of the device. By introducing such optical antennas in conjunction with other materials, the enhancements in the efficiency and performance of the solar cells and other optoelectronic devices have been demonstrated. The optical scattering by metal nanoparticles indirectly improves sensitivity of the photodetectors by the semiconductor band gap absorption. Photoelectron emission by non-radiative plasmon decay itself contributes in the optical response as in terahertz photodetectors.

The MNSs also have other enormous application in optoelectronic devices, optical/chemical sensing, photocatalysis etc.

In the first chapter, we have focussed on the charge transfer characteristics of organic molecules acting as linkers between acceptor and donor. Such molecular conducting junctions are necessary for controlled, efficient electron transfer and excitation energy transfer between two electrodes in which one acts as a donor and other one act as an acceptor. Saturated and non-saturated organic molecules in the form of self-assembled monolayers have been widely studied as a potential connecting bridge to facilitate electron transfer. Aromatic linkers suggested to be more efficient in such transfer by the involvement of a π-electrons in intramolecular as well as intermolecular processes.

In this particular study, rGO electrodes were fabricated on FTO by spray coating and then functionalized with linear chain (APTMS) molecule as well as with another organic molecule having aromatic triazole ring. Huisgen 1, 3-dipolar cycloaddition or “click chemistry” was performed to introduce aromatic triazole ring through the Cu-catalysed azide–alkyne cycloaddition reaction between terminal alkynes and azides. These linkers have bifunctional nature i.e. silane moiety anchored on rGO surface and amine groups at the free end for the electrostatic assembly of the AuNPs.

We explored the influence of AuNPs assembled on such organic linker functionalized rGO surface in photocurrent enhancement. Raman spectroscopic study reveals the significant enhancement of Raman intensity in the D and G band of the rGO. The highest enhancement is observed for the AuNPs assembled on the click modified rGO surface than the APTMS/rGO. Clicked rGO surface

has aromatic triazole ring which assists in the charge delocalization of the AuNPs and subsequent transfer to the graphene. The observed enhancement can be due to two separate mechanisms a) electromagnetic and b) chemical and it is highly debated in the literature. In this case it is the combined effect of these mechanisms. The scattering cross section of the AuNPs increases because of the higher electromagnetic field created by the localized surface plasmons on the nanoparticles as well as the delocalization or polarization by effective charge transfer from the AuNPs to the rGO through the aromatic linkers. The delocalization is ineffective or very small in the case of APTMS linkers due to lack of π-electrons and hence low Raman intensity.

The interfacial properties of the covalently modified rGO have considerably changed upon gold nanoparticle immobilisation. The electrochemical observation of rGO electrode reveals the highly conducting rGO surface where numerous defects on the edges as well as some functional groups can act as redox active centres while the aromatic backbone assists in the fast electron transport. Functionalized rGO electrodes on the other hand suggest purely blocking nature and compact monolayers of the organic molecules which have been used to functionalize the graphene. However, the redox properties of the ferrocyanide probe reappear after gold nanoparticles attachment on these linkers suggesting the formation of electron transport bridges between the AuNPs and graphene. AuNPs act as nanosized redox centres for the ferrocyanide probe as indicated by the cyclic voltametry and impedance measurement. The difference between the linkers can also be distinguished from the low resistance observed for the AuNPs attached on click modified rGO surface.

Enhanced photocurrent is observed for the rGO/AuNPs hybrid with different linker molecules. AuNPs assembled on the click-functionalised rGO shows higher photocurrent density than AuNPs assembled on the aliphatic linkers on the rGO. Here, AuNPs act as plasmonic antenna for light harvesting and triazole act as an effective electron-transferring linker. The wavelength dependent photocurrent reveals the plasmon intervened photocurrent. The nature of SAMs influences the electron-transport properties in the hybrid in which aromatic triazoles show the fast electrical conduction. Also, by comparison, the CV and electron impedance spectroscopy (EIS) data at the interface of the electrodes suggest the conjugated triazole ring to be an excellent bridge for the fast charge transport to the graphene surface. The inclusion of π- conjugation near metal nanoparticles allows an efficient pathway for the relaxation of hot electrons, thereby ensuring a large photocurrent from the hybrid.

Chapter 2 deals to understand the effect of the surface plasmon of gold nanoparticles on SiNWs/TiO_2 heterojunctions. Here, simple dip coating method has been carried out for the synthesis of heterojunctions and gold nanoparticles were embedded in the TiO_2 matrix by soaking it in gold salt solution along with annealing under normal atmosphere. The SiNWs already has low reflectance which is further lowered by the TiO_2 thin coating on the SiNWs. This is attributed to the antireflection properties of the TiO_2. However, large enhancement can be observed after deposition of gold nanoparticles which is due to the high absorption and scattering properties of the nanoparticles.

The absorption and scattering cross section are the result of the surface plasmon resonance of gold which can be altered by the environment around the nanoparticles. TiO_2 with highest refractive

index and dielectric constant affect the SPR frequency as well. This influences the optical and photocurrent properties of the nSiNWs/TiO_2 heterojunction. Such gold plasmon-sensitized SiNWs/TiO_2 exhibits broadband visible light absorbance and photoresponse at matching wavelengths between the SPR and interband transitions.

TiO_2 layers formed on the surface of SiNWs shows photoluminescence as a result of oxygen vacancies. A large enhancement in photoluminescence is also observed after gold nanoparticles deposition. The positions of energy of the vacancies lie just below the conduction band of the TiO_2 and they can be differentiated into a) band edge emission from TiO_2, b) single and c) double electron vacancies. It is found that the TiO_2 PL peaks originally appeared were shifted to higher energy levels after gold nanoparticles deposition. Furthermore the two electron oxygen vacancy related peaks were absent. The analogy behind the increased intensity can be due to the formation of more oxygen vacancies or enhanced rate of exciton formation. The disappearance of the shallow oxygen vacancies of TiO_2 at 505 nm suggest that this emission energy can be utilized for the excitation of SPR on the gold nanoparticles. Electric field in the vicinity of gold nanoparticles can be amplified which results in the creation of more excitons in the nearby TiO_2. The gold nanoparticles decorated heterojunction shows highest photocurrent than the standard sample. The maximum photocurrent was achieved near the plasmon resonance wavelength of the gold nanoparticle. The simultaneous plasmonic energy transfer to the semiconductor is attributed to the increased response towards the multiwavelength photoconductivity of the heterojunction. The deposition of noble metal nanoparticles on semiconductors or semiconductor heterojunctions can be effectively used in the preparation of highly efficient optoelectronic devices.

These hybrids show enhanced optical absorption, emission and photocurrent generation. Plasmonic sensitization enhances self-trapped exciton emission and oxygen vacancy radiative recombination emission properties of TiO_2.

The adsorption of metal nanostructures on the photodetection properties of the heterojunction based photodiode has been carried out and discussed in the chapter 3. A solid-state photodiode between p-CuS and Si nanowires is fabricated by Radio Frequency Magnetron Sputtering (RF) and studied for photodetection. The significant enhancement in the optical absorption and photocurrent is observed for the AuNRs dropcasted on the heterojunction surface. The AuNRs on the device surface serve as the light scattering antenna thereby increasing the optical absorption. Such plasmonic sensitization can be useful for enhanced sensitivity of visible as well as IR light photodetectors.

The heterojunction diode between SiNWs and CuS as fabricated displayed stable, quick and good photoresponse. Nearly thirteen times enhancement can be observed in the responsivity of the SiNWs/CuS junction after AuNRs deposition at open circuit voltage. While the detectivity reflect three times increment due to AuNRs. The result indicates that the optical antenna effect of AuNRs enhances the photocurrent, responsivity and detectivity of the photodiode. Both the devices are operating on independent bias and able to differentiate specific wavelengths. The observed photodetector figures of merits are based on low temperature device fabrication. We believe that they can be further improved by optimizing the CuS sputtering time and film thickness. The use of metal nanostructure can enhanced the optical properties of the semiconductor devices which is enormously applicable for high speed photodetector.

At last, the works mentioned in the thesis reveals the practicality of metal nanostructures in the optical absorption and device property enhancements. Simple covalent attachment, partial thermal treatment and deposition of plasmonic metal nanoparticles can be effectively controlled and alternatively improves the semiconductor electrochemical and physical characteristics. The optical loss occurring due to defects in the semiconductor or the inherent higher reflection can be minimized by using metal nanostructures.

5.2 Future Plans:

The works presented in the various chapters have opened up some interesting phenomena. They have to be fully understood for unravelling their importance in various applications.

1) Charge transfer rate on the electron transfer rate from metal nanoparticles to the electrode through the molecular linkers and surface enhanced Raman spectroscopy (SERS):

The plasmonic photocurrent observed for the rGO electrodes with different molecular linkers on different wavelength excitation presents a way to extract electrons from metal nanoparticles. The covalent bonding of aliphatic and aromatic molecules can be used for the efficient electron transfer. However, the rate of electron transfer is different with respect to the nature of the covalent linkers. As, discussed in the chapter 1, highest electron transfer rate is observed for the aromatic linkers. It is therefore necessary to study the electron transfer rate through such molecular linkers. We can efficiently use these bridges in the molecular switches, solar cells, and photodetectors by controlling the electron transfer rate.

The enhancement observed in the Raman bands of rGO implicates that these linkers can be useful in the detection of very low concentration of chemical compounds. By using different linkers in conjugation with the analyte we can efficiently detect the hazardous molecules.

2) Detailed understanding of the photoluminescence enhancement by metal nanoparticles:

The metal nanostructures possess high scattering and absorption cross section. The peculiar properties can be used in the light harvesting with the help of semiconductor materials. The light scattering by metal nanostructures in the semiconductor thin films alternatively increase their absorption in the interested region of solar spectrum or in the whole spectrum region. The enhanced absorption can be then effectively used for the efficiency enhancement in the solar cells, optical detection in the photodetectors, laser upconversion etc.

The second chapter in the thesis describes the effective increase in the photocurrent due to higher absorption and photoluminescence. The scattering by metal nanoparticles enhances these peculiar properties of the heterojunction. The photoluminescence due to oxygen defects present in the TiO_2 can be suppressed using the metal nanoparticles by absorption. This leads to the generation of intense electromagnetic field around the metal nanoparticles which can be used in the separation of excitons in the semiconductor. It also increases the excited electron density in the conduction band of the semiconductor. This process has to be studied more regressively.

3) Wide spectrum absorption enhancement:

This is of particular interest as the scattering by metal nanostructures are not only confined to the SPR. It is possible to enhance the hybrid absorption in the other region of the solar spectrum as

well. Therefore we can effectively use the whole solar spectrum for various applications. A comprehensive strategy of light trapping subsequent optical absorption enhancement in SiNWs/TiO_2 and SiNWs/ CuS through plasmonic metal nanostructures has been realized in ultra-broadband region. This enhancement can be translated to any wavelength from ultraviolet to terahertz ranges by simple modification of the geometric design of the plasmonic nanostructure and can be applied not only in two dimensional but also one dimensional materials and their heterojunction structures. It may significantly improve the efficiency of optical devices such as broadband photodetectors and solar cells based on silicon, graphene as well as other semiconductor materials.

Publications

1) **Sandeep G. Yenchalwar**, Vedi Kuyil Azhagan and Manjusha V. Shelke," Enhanced photoluminescence and photoactivity of plasmon sensitized nSiNWs/TiO2 heterostructures", *Physical Chemistry Chemical Physics*, 2014, 16 (33), 17786.

2) **Sandeep G. Yenchalwar**, Rami Reddy Devarapalli, Ashvini B. Deshmukh and Manjusha V. Shelke," Plasmon-Enhanced Photocurrent Generation from Click-Chemically Modified Graphene", *Chemistry-A European Journal*, 2014, 20 (24), 7402.

3) Rupali S. Mehare, Rami Reddy Devarapalli, **Sandeep G. Yenchalwar** and Manjusha V. Shelke, "Microfluidic spatial growth of vertically aligned ZnO nanostructures by soft lithography for antireflective patterning", *Microfluid Nanofluid*, 2013 15, 1.

4) Rami Reddy Devarapalli, Deodatta R. Shinde, Fatiha Barka-Bouaifel, **Sandeep G. Yenchalwar**, Rabah Boukherroub, Mahendra A. More and Manjusha V. Shelke, "Vertical arrays of SiNWs–ZnO nanostructures as high performance electron field emitters", *J. Mater. Chem.* 2012, 22, 22922.

5) **Sandeep G. Yenchalwar**, Sachin R. Rondiya, Pravin N. Shinde, Sandesh. R. Jadkar and Manjusha V. Shelke, "Optical antenna effect on SiNWs/CuS photodiode", *Manuscript Submitted*.